



Algorithm Theoretical Basis Document (ATBD)
for the
Conical-Scanning Microwave Imager/Sounder (CMIS)
Environmental Data Records (EDRs)

Volume 7: Cloud EDRs
Part 1: Cloud Ice Water Path EDR

Version 1.6 – 15 March 2001

Solicitation No. F04701-01-R-0500

Submitted by:
Atmospheric and Environmental Research, Inc.
131 Hartwell Avenue
Lexington, MA 02421-3126

With contributions by:
Jean-Luc Moncet, Sid Boukabara, Robert D'Entremont,
Ned Snell, Hélène Rieu-Isaacs, Alan Lipton,
Frank Evans (University of Colorado), David Mitchell (DRI).

Prepared for:
Boeing Satellite Systems
919 Imperial Avenue
El Segundo, CA 90245

AER Document P757-TR-I-ATBD-CIWP-20010315

This page intentionally left blank.

REVISION HISTORY

Version	Release Date	POC	Comments
1.0		J. L. Moncet, AER, Inc.	First Draft Version
1.5	22 February 01	J. L. Moncet, AER, Inc.	Post-PDR Version
1.6	15 March 01	S. Boukabara, AER, Inc.	Made this version consistent with what was presented at PDR

RELATED CMIS DOCUMENTATION

Government Documents

Title	Version	Authorship	Date
CMIS SRD for NPOESS Spacecraft and Sensors	3.0	Associate Directorate for Acquisition NPOESS IPO	2 March 2001

Boeing Satellite Systems Documents

Title		Covering
ATBD for the CMIS TDR/SDR Algorithms		
ATBD for the CMIS EDRs	Volume 1: Overview	Part 1: Integration Part 2: Spatial Data Processing <ul style="list-style-type: none"> • Footprint Matching and Interpolation • Gridding • Imagery EDR
	Volume 2: Core Physical Inversion Module	
	Volume 3: Water Vapor EDRs	Atmospheric Vertical Moisture Profile EDR Precipitable Water EDR
	Volume 4: Atmospheric Vertical Temperature Profile EDR	
	Volume 5: Precipitation Type and Rate EDR	
	Volume 6: Pressure Profile EDR	
	Volume 7: Cloud EDRs	Part 1: Cloud Ice Water Path EDR
		Part 2: Cloud Liquid Water EDR
		Part 3: Cloud Base Height EDR
	Volume 8: Total Water Content EDR	
	Volume 9: Soil Moisture EDR	
	Volume 10: Snow Cover/Depth EDR	
	Volume 11: Vegetation/Surface Type EDR	
	Volume 12: Ice EDRs	Sea Ice Age and Sea Ice Edge Motion EDR Fresh Water Ice EDR
	Volume 13: Surface Temperature EDRs	Land Surface Temperature EDR Ice Surface Temperature EDR
	Volume 14: Ocean EDR Algorithm Suite	Sea Surface Temperature EDR Sea Surface Wind Speed/Direction EDR Surface Wind Stress EDR
	Volume 15: Test and Validation	All EDRs

Bold = this document

TABLE OF CONTENTS FOR VOLUME 7, PART 1

REVISION HISTORY.....	3
RELATED CMIS DOCUMENTATION	4
TABLE OF CONTENTS FOR VOLUME 7, PART 1	5
LIST OF TABLES	8
LIST OF FIGURES	9
1. Introduction.....	13
1.1. Purpose of Retrieving Cirrus Cloud Ice	13
1.2. Scope	13
2. Overview and Background Information.....	14
2.1. Cloud Ice Water Path Definition and Requirements	14
2.1.1. Precipitating and Non-Precipitating Cases	14
2.2. Physics of the Problem.....	14
2.2.1. Cirrus Cloud Parameters Affecting the Radiometric Signal	15
2.2.2. Definitions	16
2.2.3. Sensitivity to Cirrus Particle Shape and Size	16
2.3. Cirrus Cloud Microphysics	18
2.3.1. Dependence of Ice-Cloud Radiative Properties on the Natural Variability of Ice-Particle Shape	18
2.3.2. Ice Crystal Size Distributions in Natural Cirrus.....	31
2.4. Channel Selection.....	34
2.4.1. Computation of Optical Properties.....	35
2.5. Instrument Characteristics.....	36
2.6. Requirements for Cross-Sensor Data (NPOESS or Other Sensors).....	36
3. Microwave Algorithm Description and Performance	37
3.1. Non-Precipitating Clouds.....	37
3.1.1. Historical and Background Perspective of the IWP Retrieval	38
3.1.2. Microwave Retrieval Approach for Non-Precipitating Clouds.....	39
3.1.3. Algorithm Processing Outline	40
3.1.4. Forward Model in the Presence of Scattering	40
3.1.5. Ice Water Path Algorithm Performance (Non-Precipitating Clouds).....	40
3.2. Precipitating Clouds	51
3.2.1. Microwave Retrieval Approach (Precipitating Clouds).....	51
3.2.2. Description of Test Data.....	51

TABLE OF CONTENTS

3.2.3. Forward Model in the Presence of Precipitation	52
3.2.4. Ice Water Path Algorithm Performance in the Presence of Precipitation	53
3.3. Microwave Algorithm Performance Summary	54
4. Infrared Algorithm Description and Performance.....	55
4.1. Cirrus Attributes.....	55
4.2. Infrared Algorithm Description.....	56
4.2.1. The Cloud Retrieval Problem.....	56
4.2.2. Ice Crystal Cloud Emissivity and Temperature	57
4.2.3. Ice Crystal Effective Diameter	58
4.2.4. Absorption of Infrared Radiation by Ice Clouds	60
4.2.5. Ice Water Path	62
4.2.6. Algorithm Description Summary	63
4.3. Numerical Attributes of the Infrared IWP Retrieval Algorithm	64
4.3.1. Algorithm Trade Space	64
4.3.2. Noise-free IWP Retrieval Sensitivities.....	65
4.3.3. IWP Retrieval Sensitivities to Sensor and Clear-Scene Noise.....	70
4.3.4. Accuracy and Precision Performance Indices for Rosettes.....	72
4.4. Summary of the Infrared Algorithm Description and Performance.....	78
5. Final Error Budget.....	79
6. Algorithm Calibration and Validation Requirements.....	80
6.1. Pre-launch.....	80
6.2. Post-launch.....	80
6.3. Special Considerations for Cal/Val.....	81
6.3.1. Measurement Hardware	81
6.3.2. Field Measurements or Sensors.....	81
6.3.3. Sources of Truth Data.....	81
7. Practical Considerations.....	82
7.1. Ice Water Path Algorithm Timing Constraints	82
7.2. Numerical Computation Considerations	82
7.3. Programming/Procedure Considerations.....	82
7.4. Computer Hardware or Software Requirements	82
7.5. Quality Control and Diagnostics.....	82
7.6. Exception and Error Handling.....	82
7.7. Special Database Considerations	82

TABLE OF CONTENTS

7.8. Special Operator Training Requirements.....	82
7.9. Archival Requirements.....	82
8. Appendix 1: Impact of Sub-Millimeter Channels on the IWP Retrieval.....	83
8.1. Introduction.....	83
8.2. Description of the Experiments.....	83
8.3. Impact of Adding Sub-Millimeter Channels.....	83
8.4. Results/Conclusion.....	84
REFERENCES.....	89
LIST OF ACRONYMS.....	92

LIST OF TABLES

Table 1: Ice Water Path Measurement Requirements.....	14
Table 2: Extinction coefficient, single scattering albedo, and asymmetry coefficients for different values of Dme and volume fraction.....	18
Table 3: Cirrus crystal habit percentages (from Heymsfield and Iaquinta, 2000)	20
Table 4: Frequency of occurrence of pristine ice particles in Arctic clouds (from Korolev et al., 1999).....	21
Table 5: The frequency of occurrence of ice particle habits over the four projects: BASE, CFDE I, CFDE III, and FIRE ACE for the three size ranges: $D > 125$, $D > 250$, and $D > 500 \mu\text{m}$ (from Korolev et al. 2000).....	22
Table 6: Constants used in the projected-area and mass-dimensional power laws (see Equations (1) and (2)) for hexagonal columns and plates, bullet rosettes, and planar polycrystals. All units are cgs.....	24
Table 7: Sphere-equivalent mass-median particle sizes for the ARM/FIRE mid-latitude and CEPEX tropical ice-crystal observations	33
Table 8: Small-mode normalized ice-water contents for the ARM/FIRE mid-latitude and CEPEX tropical ice-crystal observations. Large-mode portions are computed simply as $IWC_{\text{large}} = 1 - IWC_{\text{small}}$	34
Table 9: Sources of cross-sensor data required for CMIS.	36
Table 10: Components of the IWP error budget.	38
Table 11: Surface and cloud parameters used in verification of the IWP algorithm performance.	41
Table 12: Description of the sub millimeter channels tested in the “CMIS+325” configuration. The three channels are centered around the 325 water vapor absorption line and are all mono-sided.	42
Table 13: Error budget summary for known cloud top.....	79
Table 14: Error budget summary for unknown cloud top.....	79
Table 15: Description of the sub-millimeter channels tested along with the CMIS baseline configuration.	83
Table 17: IWP and Dme ranges for the different instrumental configurations, based on an accuracy threshold of 15% and a precision threshold of 20%.	84
Table 18: IWP and Dme ranges for the different instrumental configurations, based on an RMS error threshold of 25%.....	84

LIST OF FIGURES

Figure 1: Sensitivity Peaks for Different Particle Sizes.....	15
Figure 2: Effect of cirrus particle shape and size on the ratios of brightness temperature depression to IWP. Courtesy of Frank Evans [Evans, 2000].....	17
Figure 3: Projected area as a function of maximum particle size.	25
Figure 4: Ice crystal mass as a function of maximum particle size.....	25
Figure 5: Effective diameter of a size distribution for the 16 flights listed in Table 3. ...	28
Figure 6: Emissivity at 3.85 μm for the flights listed in Table 3 for a mode mean of 100 μm	29
Figure 7: Percent difference of the actual emissivity from the mean shown in Figure 6.	29
Figure 8: Emissivity at 3.85 μm for the flights listed in Table 3 for a mode mean of 300 μm	30
Figure 9: Percent difference of the actual emissivity from the mean shown in Figure 8..	30
Figure 10: Atmospheric transmission for a vertical path from 10 km to the top of the atmosphere.	35
Figure 11: Transmission from high altitude down to four different altitudes. Courtesy of Frank Evans [Evans, 2000].....	35
Figure 12 Flow diagram of the ice water retrieval module.....	37
Figure 13: Retrieval (a) accuracy and (b) precision for 300 mb cloud over ocean with CMIS+325 channel set and known cloud top pressure.....	43
Figure 14: Retrieval (a) accuracy and (b) precision for 300 mb cloud over ocean with CMIS channel set and known cloud top pressure.	43
Figure 15: Retrieval (a) accuracy and (b) precision for 300 mb cloud over ocean with CMIS+325 channel set and unknown cloud top pressure.	44
Figure 16: Retrieval (a) accuracy and (b) precision for 300 mb cloud over ocean with CMIS channel set and unknown cloud top pressure.	44
Figure 17: Retrieval (a) accuracy and (b) precision for CMIS channel configuration and known cloud top pressure.....	45
Figure 18: Retrieval (a) accuracy and (b) precision for 300 mb cloud over land with CMIS+325 channel set and known cloud top pressure.....	45
Figure 19: Retrieval (a) accuracy and (b) precision for 300 mb cloud over land with CMIS channel set and known cloud top pressure.	46

LIST OF FIGURES

Figure 20: IWP retrieval performances as a function of median diameter (D_{me}) (IWP 300 g/m ²). Cloud Top is assumed known (300 mb). Little retrieval skill for D_{me} below 400 mm ⁴⁷	
Figure 21: Precision (left) and Accuracy (right) of the Ice Water Path Retrieval for the CMIS configuration. The cirrus cloud top is 300 mb in this case and is supposed known from an external source. Only D_{mes} above 400 microns were considered for the computation of these statistics. For the error budget, the worst case in the IWP range was picked. Case over ocean.....	48
Figure 22: Bimodal Distribution and its impact on the scattering coefficient.	49
Figure 23: Distribution of the Ice water content for the two modes (small and large) for both tropics and mid-latitudes.	50
Figure 24: Schematic diagram showing vertical distribution of cloud constituents used for the generation of hydrometeor profiles (Kummerow and Giglio, 1994). The rain-rate (R) is selected randomly within a predetermined range using a random number (Ψ) between 0 and 1. For the case shown here, the RR falls in the range from 0-20.	52
Figure 25: Ocean retrieval (a) accuracy and (b) precision for threshold range of IWP...	53
Figure 26: Land retrieval (a) accuracy and (b) precision for threshold range of IWP.....	53
Figure 27: Ocean retrieval (a) accuracy and (b) precision for objective range of IWP...	54
Figure 28: Land retrieval (a) accuracy and (b) precision for objective range of IWP.....	54
Figure 29: Plot of all theoretically possible pairs of cirrus emissivity and effective temperature for a given set of observed MWIR and TIR brightness temperatures.....	64
Figure 30: Noise-free IWP-retrieval accuracies for simulations of planar polycrystals in a tropical atmosphere, and for varying cirrus thicknesses.	67
Figure 31: Noise-free IWP-retrieval precisions for simulations of planar polycrystals in a tropical atmosphere, and for varying cirrus thicknesses.	68
Figure 32: Summary of accuracy performance indices for planar polycrystals in a tropical atmosphere (noise free).	69
Figure 33: Summary of precision performance indices for planar polycrystals in a tropical atmosphere (noise free).	70
Figure 34: IWP-retrieval accuracy performance indices for simulations of planar polycrystals in a tropical atmosphere, and for varying cirrus thickness, with sensor and clear-scene noise models.	71
Figure 35: IWP-retrieval precision performance indices for simulations of planar polycrystals in a tropical atmosphere, and for varying cirrus thickness, with sensor and clear-scene noise models.	72

LIST OF FIGURES

Figure 36: IWP-retrieval accuracy performance indices for simulations of rosettes in a tropical atmosphere, and for varying cirrus thickness, with sensor and clear-scene noise models.	73
Figure 37: IWP-retrieval precision performance indices for simulations of rosettes in a tropical atmosphere, and for varying cirrus thickness, with sensor and clear-scene noise models.	74
Figure 38: IWP-retrieval accuracy performance indices for simulations of planar polycrystals in a mid-latitude atmosphere, and for varying cirrus thickness, with sensor and clear-scene noise models	75
Figure 39: IWP-retrieval precision performance indices for simulations of planar polycrystals in a mid-latitude atmosphere, and for varying cirrus thickness, with sensor and clear-scene noise models.	76
Figure 40: IWP-retrieval accuracy performance indices for simulations of rosettes in a mid-latitude atmosphere, and for varying cirrus thickness, with sensor and clear-scene noise models.	77
Figure 41: IWP-retrieval precision performance indices for simulations of rosettes in a mid-latitude atmosphere, and for varying cirrus thickness, with sensor and clear-scene noise models.	78
Figure 42: RMS error, accuracy and precision of the ice water path retrieval using the CMIS baseline configuration. The low errors at 200 g/m ² correspond to the background value taken for these retrievals (200 g/m ²) and not to a real skill.	85
Figure 43: RMS error, accuracy and precision of the ice water path retrieval using the CMIS configuration plus three channels around the 325 GHz WV absorption line.	86
Figure 44: RMS error, accuracy and precision of the ice water path retrieval using the CMIS configuration plus three channels at 325 GHz and an additional one at 642 GHz. ..	87
Figure 45: RMS error, accuracy and precision of the ice water path retrieval using the CMIS configuration plus three channels at 325 GHz and additional ones at 642, 680 and 820 GHz.	88

LIST OF FIGURES

1. Introduction

1.1. Purpose of Retrieving Cirrus Cloud Ice

Cirrus clouds cover 20% of the Earth (Wylie et al., 1994). The impact of ice clouds on the radiation budget is important as it can result in heating or cooling of the earth (Stephens and Webster, 1981; Stephens et al., 1990). Further, the release of latent heat in cloud formations provides an important fraction of the thermal energy required to drive atmospheric circulation (Chahine, 1992). On the other hand, general Circulation Models (GCM) are sensitive to the uncertainty in measuring cirrus (Del Genio, 1992). While there is a smaller ice water path (IWP) in thin cirrus than in convective systems, thin cirrus have a much larger global coverage. Ice clouds exist in the upper troposphere and they are globally distributed over land and ocean. Thus quantitative measurements of ice cloud properties could improve our ability to model and predict climate variability, and this requires a global and continuous system for measuring ice amounts in the atmosphere.

In summary, the importance of measuring ice clouds consists of (1) helping to quantify the role of cirrus clouds in global climate systems, (2) improving seasonal to interannual climate prediction and (3) helping modeling the hydrological cycle.

1.2. Scope

The Core Physical Inversion Module of the CMIS EDR algorithms performs a major portion of the retrieval processing for the IWP EDR. That module is described in ATBD Volume 2, and includes discussion of some aspects of the physics of the retrieval problem. This document discusses the physical aspects specific to the IWP retrieval, presents the portions of the algorithm not covered by the Core Module ATBD, and presents performance of the IWP EDR product.

2. Overview and Background Information

2.1. Cloud Ice Water Path Definition and Requirements

Cloud ice water path (CIWP, or IWP) is defined as the equivalent amount of water within cloud ice particles, including any particles that are precipitating even if they have fallen below cloud base, in a specified segment of a vertical column of the atmosphere. For this EDR, vertical cell size is the vertical height of the column segment and the vertical reporting interval specifies the locations of the column segment bottoms for which cloud ice water path must be reported.

The IWP measurement error is specified in terms of accuracy and precision. We interpret these, in accordance with the SRD glossary (Appendix A) as the bias and standard deviation of the measurement error, respectively. We believe that the numeric values that were applied to these two metrics should be exchanged in order to be consistent with the definitions of the metrics and the error characteristics of environmental remote sensing products.

Table 1: Ice Water Path Measurement Requirements.

Parameter	Thresholds	Objectives
a. Horizontal Cell Size	50 km	10 km
b. Horizontal Reporting Interval	50 km	10 km
c. Vertical Cell Size	N/A (Total Column)	0.3 km
d. Vertical Reporting Interval	N/A (Total Column)	0.3 km
e. Horizontal Coverage	Global	Global
f. Vertical Coverage	N/A (Total Column)	0 - 20 km
g. Measurement Range	0 - 2.6 kg/m ²	0 - 10 kg/m ²
h. Measurement Accuracy	5 %	2 %
i. Measurement Precision	10 % or 5 g/m ²	5 %
j. Long Term Stability	2 %	1 %
k. Mapping Uncertainty	4 km	1 km
l. Swath Width	1700 km	3000 km

2.1.1. Precipitating and Non-Precipitating Cases

Because of the measurement range extending from 0 to 2.6 kg/m², the meteorological situations covered by the requirements consist of both cirrus and precipitating convective clouds.

2.2. Physics of the Problem

Ice is very weakly absorbing in microwave and submillimeter spectral regions, and the signal from ice clouds is predominately from scattering by ice crystals. Figure 1 shows that the peak in extinction (peak sensitivity) for a single ice sphere shifts towards higher frequencies for smaller and smaller particles. At 200 GHz the measurements are affected by particles of ~200 μm or more in size. The small ice particles (~10 μm or less) can only be detected from infrared measurements. Thus to provide retrieval capability over required IWP measurement range the spectral coverage of measurements must extend from the microwave to the IR. This will provide

a full characterization of the size distribution for polydispersed particles and the detection of thin clouds (up to 100g/m^2) with small particles.

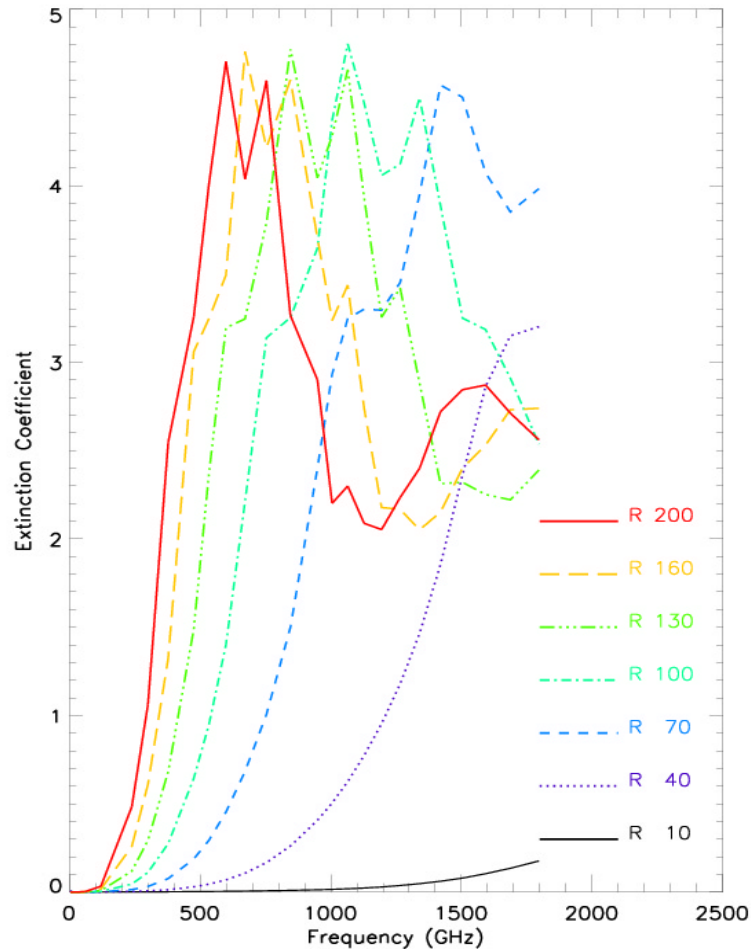


Figure 1: Sensitivity Peaks for Different Particle Sizes.

2.2.1. Cirrus Cloud Parameters Affecting the Radiometric Signal

The temperature of the cloudy layers is not critical because of a large amount of scattering and weak emission/absorption by ice in the millimeter and sub-millimeter spectral regions. The strong water vapor absorption in the sub-millimeter spectral region screens out the lower altitude clouds and the surface variability. The scattering is highly sensitive to the ice particle size distribution (Mugnai et al., 1990). The cirrus cloud parameters that have an effect on the measured radiances are:

- The ice water content in the atmospheric column.
- The ice particle size distribution.
- The ice particle shape.
- The signal is modulated by the water vapor load, therefore, the cloud top height is important.
- The vertical distribution of the ice water content, and the median diameter of the particle size distribution (Dme).

Evans and Stephens (1995b) studied the IWP sensitivity by estimating the brightness temperature depression for a change in IWP. From this they found that the sensitivity was linear except for high IWP where the sensitivity drops and the brightness temperature depressions become non-linear for a change in IWP. They also found that the upwelling radiance of a cirrus cloud is

independent of the cloud temperature for both high spectral frequencies and distributions with large particle sizes. However, the sensitivity increases strongly with frequency and median particle size. Further, the variance of the particle size distribution produces an ~7% variation in the IWP sensitivity. Evans and Stephens tried to gain additional information to retrieve particle size by using ratios of brightness temperature depressions for various channels. However, this approach requires very high frequency channels to avoid multiple solutions.

Evans and Stephens also studied the IWP sensitivity to particle shape. The ratios of brightness temperature depressions at different polarizations provide information about the particle shape. Polarimetric observations (four Stokes parameters) could also provide useful information on the crystal habit, which would improve the retrieval of IWP.

2.2.2. Definitions

The cloud ice water path (IWP) is defined as:

$$IWP = \int_{H_0}^{H_1} dz \int_0^{\infty} \frac{\pi}{6} \rho_{ice} D^3 N(D) dD \quad (1)$$

where $N(D)$ is the size distribution or concentration of particles of size D , and ρ_{ice} is the ice density. For a Gamma distribution, $N(D)$ is represented by :

$$N(D) = a_g D_e^\alpha \exp(-(\alpha + 3.67)D_e / D_{me})$$

where D_e is the diameter of the equivalent mass sphere (for a pure sphere, $D_e = D$), D_{me} is the median mass diameter of the distribution, α is related to the width of the distribution and a_g is found from the ice mass content. The relation between D_{me} and other measures of particle size depends on size and shape and the width of the distribution; for solid spheres with $\alpha=1$, $D_{me} = 2.3r_e$ where r_e is the effective radius. This definition is consistent with previous studies (Evans et al., 1997).

The effective diameter is defined as:

$$D_e = \frac{\int_0^{\infty} N(D) D^3 dD}{\int_0^{\infty} N(D) D^2 dD} \quad (2)$$

The ice density ρ_{ice} can vary greatly in precipitating clouds, which limits considerably the ability to retrieve IWP and D_{me} . It can be as low as 0.1 g/cm^3 (Hobbs et al., 1975) and as high as 0.5 g/cm^3 for mixed air and solid ice. For pure solid ice, $\rho_{ice} = 0.92 \text{ g/cm}^3$.

2.2.3. Sensitivity to Cirrus Particle Shape and Size

The brightness temperature sensitivity to IWP is shown in Figure 2 for different cirrus particle shapes and sizes. These results were obtained by computing the optical properties using the Discrete Dipole Approximation (DDA) (Evans and Stephens, 1995) and radiative transfer

calculations for 7 different particle shapes. The sensitivity is much larger at 630 GHz (21 cm^{-1}) than at 183 GHz.

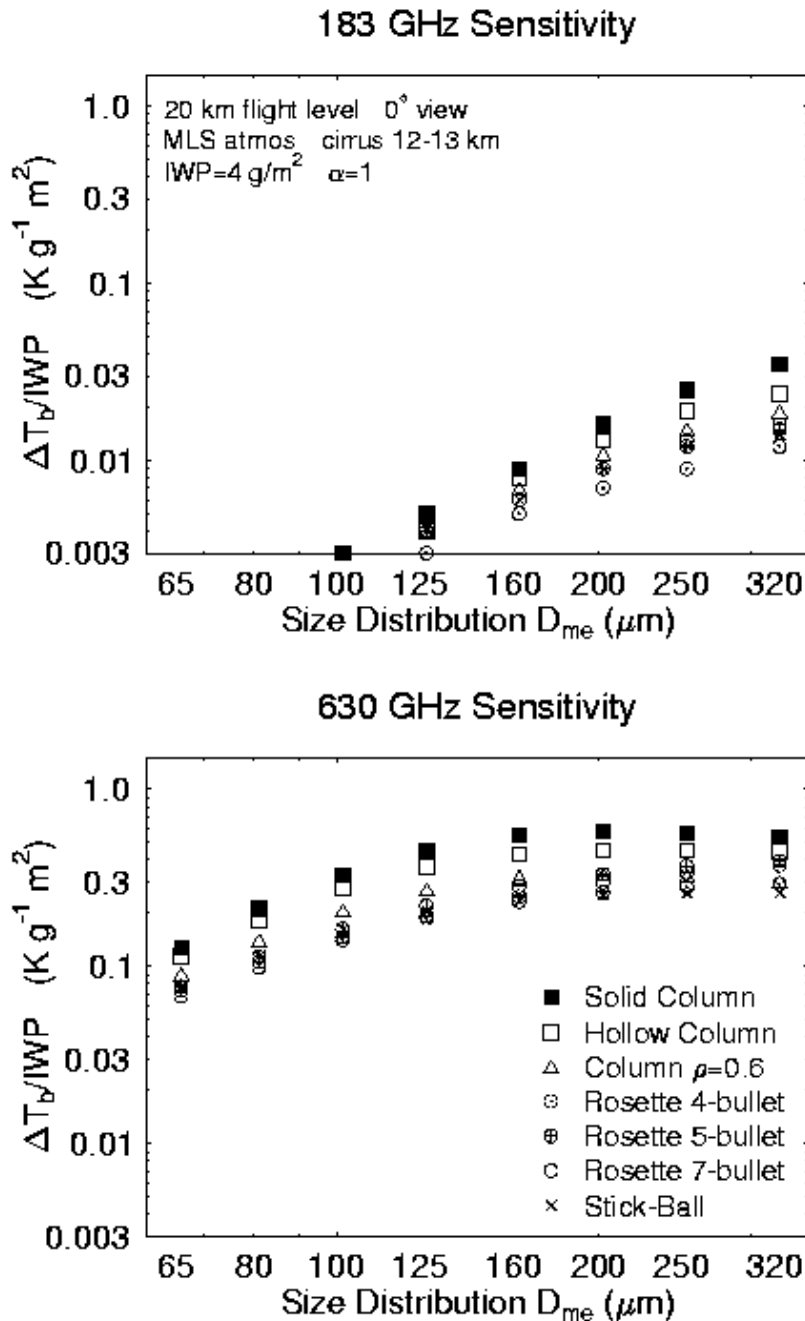


Figure 2: Effect of cirrus particle shape and size on the ratios of brightness temperature depression to IWP. Courtesy of Frank Evans [Evans, 2000].

Millimeter and sub-millimeter observations are sensitive to large ice particles (i.e., particles with a diameter greater than $50 \mu\text{m}$). In contrast, the IR is sensitive to small size ice particles and low IWP values. Depending on the characteristic size, the IR saturates quickly, at IWP values approaching 50 g/m^2 .

However, if the cloud is located above the region of high water vapor absorption, the IR radiances do not depend on the vertical distribution of ice within the cloud.

Bauer et al. (2000) studied the effect of melting particles for modeling stratiform rainfall on the microwave emission (10-100 GHz) and found that this could have an important effect, suggesting that hydrometeor retrieval could be affected if not accounted for melting. The distribution width (or variance) has been found to have a minimum effect.

The IWP retrieval performance depends highly on assumptions regarding ice crystal shape/density and the size distribution. Large variations in the IWP estimate (100% or more) may result from the use of different assumptions regarding the bulk density of ice particles (Weng and Grody, 2000). The impact of particle shape/density on the microwave optical properties is illustrated in Table 2. For a given Dme the extinction, single-scattering albedo, and asymmetry parameters can each have very different values depending on the volume fraction. Similarly, for a given volume fraction these parameters will have very different values depending on the Dme.

Table 2: Extinction coefficient, single scattering albedo, and asymmetry coefficients for different values of Dme and volume fraction.

Ice Spheres (IWC = 1.0 g/m ³), f=89 GHz				
D (μm)	Volume Fraction	Extinction (km ⁻¹)	Single-Scattering Albedo	Asymmetry Parameter
200	1.0	0.009	0.5006	0.0079
200	0.4	0.010	0.2679	0.0063
200	0.1	0.010	0.0802	0.0057
400	1.0	0.440	0.8833	0.3130
400	0.4	0.028	0.7366	0.2530
400	0.1	0.015	0.4008	0.0231
1000	1.0	0.645	0.9876	0.2
1000	0.4	0.296	0.9701	0.1591
1000	0.1	0.083	0.8875	0.1475
2000	1.0	2.670	0.9946	0.5126
2000	0.4	1.138	0.9901	0.6381
2000	0.1	0.281	0.9654	0.5748

2.3. Cirrus Cloud Microphysics

The microphysical attributes of cirrus clouds measured to date in such campaigns as CEPEX, ARM, and FIRE are discussed in this section, including the natural variability of ice-water content, crystal shape, and crystal size. The repeatability of these attributes are exploited in the CMIS UR retrieval paradigm in helping to assess algorithm performance metrics, to the extent that any or all of these observations are consistently similar in the contemporary literature.

2.3.1. Dependence of Ice-Cloud Radiative Properties on the Natural Variability of Ice-Particle Shape

2.3.1.1 Background

The radiative properties of ice clouds depend strongly on ice crystal shape due to the impact of shape on (1) the scattering phase function, (2) the projected area of the entirety of ice crystals in the size distribution, and (3) the effective photon path through an ice crystal. For emitted

terrestrial radiation, (1) may be negligible, since absorption and emission are the primary radiative processes. Hence, for the retrievals of ice water path described here, (2) and (3) are relevant. In the radiation scheme described in Mitchell (2000b), the factors determining (2) and (3) are the projected-area-dimensional and the mass-dimensional relationships, which are power laws formulated in terms of the ice-particle maximum dimension D and expressed as

$$P = \gamma D^\sigma \quad (1)$$

and

$$m = \alpha D^\beta, \quad (2)$$

where P = projected area (e.g., cm^2), m = mass (g), and γ , σ , α , and β are constants.

During development of our thermal-infrared (TIR) IWP retrieval algorithm, which is designed to augment baseline CMIS IWP retrievals when IWP is low and/or crystals are small, we found that cirrus-cloud extinction and absorption properties are not dependent on crystal shape per se but rather the mass- and projected-area vs. D relationships (i.e., Eqs. (1) and (2)) that correspond to a given crystal-shape type. Thus, two ice particles could appear different visually, but if their m - D and P - D relationships are the same then they have similar radiative properties. A second factor that strongly influences the cirrus bulk radiative properties is the functional form, or “shape,” of the size distribution $N(D)$. This will be discussed in upcoming sections, but first we will examine the literature for the state-of-knowledge of crystal shapes in natural cirrus clouds.

2.3.1.2 Ice-Particle Shape Probabilities

The objective of this analysis is to overview our current knowledge of ice particle shapes in cirrus clouds, and to evaluate the m - D and P - D relationships for the principal ice-particle shapes. Although much literature contains qualitative observational information on ice-particle shapes in natural ice clouds, very little exists that addresses the percentages of different ice-particle shapes. This analysis is restricted to studies that quantify the relative abundance of the various crystal shapes found in cirrus clouds. From this analysis, we can determine the sensitivity of ice-cloud radiative properties (e.g., emissivity) to natural variations in ice particle shape.

We begin by reviewing Table 3 from Heymsfield and Iaquinta (2000), which has been reconstructed below. The table contains estimates of the percentages of ice crystal shape for eight case studies sampled during the FIRE-1 field campaign, and for eight other case studies sampled during the FIRE-2 campaign. Ice particle shapes were determined from samples on oil-coated slides or replicator film, and from 2-D optical probe images. The flights listed in Table 3 were conducted in mid-latitude, synoptically generated cirrus, and no flights were carried out in convectively generated anvil cirrus.

The “rosettes/branched” category under FIRE 1 includes both bullet rosettes and aggregates containing bullet rosettes, bullets and/or side planes, while the “spatial” category under FIRE 1 is similar to the “spatial plate” category under FIRE 2. Spatial plates can be generally described as polycrystals having plate-like components, or planar polycrystals. Side planes are one type of planar polycrystal, and a number of crystal shapes in this category are yet to be given formal names. Rather than using the term spatial plates, these crystal types will be henceforth referred to as planar polycrystals. The miscellaneous category under FIRE 2 (“Misc.”) refers to irregular ice particle shapes (including aggregates) that could not be unambiguously classified under the

OVERVIEW AND BACKGROUND INFORMATION

other categories. The percentages in Table 1 shown in bold indicate the dominant ice crystal habit or shape. It is seen that cloud temperatures during FIRE 1 were considerably warmer than during FIRE 2. Bullet rosettes dominated in half of the cases during FIRE 1, and planar polycrystals dominating in seven of the eight cases during FIRE 2.

Table 3: Cirrus crystal habit percentages (from Heymsfield and Iaquinta, 2000)

FIRE-1 King Air						
Date	Temperature (°C)		Habit (%)			
	Top	Base	Columns	Plates	Rosettes/ Branched	Other
19 Oct 86	-41.5	-26.5	26	4	59	11
22 Oct 86	-37.0	-25.0	28	7	42	33
25 Oct 86	-35.8	-25.0	25	8	49	18
25 Oct 86 B	-32.0	-25.0	21	10	29	40
28 Oct 86	-37.2	-25.0	5	2	48	42
1 Nov 86	-43.2	-25.1	51	16	20	13
1 Nov 86 B	-44.0	-25.0	41	25	18	16
2 Nov 86	-43.5	-25.0	22	7	33	39
FIRE-2 University of North Dakota Citation						
Date	Temperature Range (°C)	Habit (%)				
		Columns	Plates	Rosettes	Spatial Plates	Misc.
11 Nov 91	-54 to -33	12	20	43	17	31
25 Nov 91	-55 to -39	8	20	35	43	5
26 Nov 91	-60 to -47	14	32	24	39	11
28 Nov 91	-59 to -48	4	10	19	48	16
30 Nov 91	-55 to -50	4	14	4	62	15
5 Dec 91	-64 to -38	5	8	17	65	6
5 Dec 91 B	-64 to -47	26	13	25	47	9
7 Dec 91	-45 to -35	6	6	26	51	9

While Table 3 indicates monocrystalline types (i.e. hexagonal columns and plates) generally constitute a minority of the total population of ice particles, other recent studies indicate these monocrystalline habits constitute a much smaller percentage than Table 3 indicates. Korolev et al. (1999) reported on ice particle habits in arctic clouds during the FIRE Arctic Cloud Experiment (FIRE ACE), where ice-particle morphology was measured using a Cloud Particle Imager (CPI). This newly developed probe has a pixel resolution of 2.3 μm , rendering very detailed images of particles having $D > 40 \mu\text{m}$. Another advantage of the CPI is its ability to process up to 1000 particles per second in real time, a vast improvement over oil-coated slides and labor intensive replicators. At the same time its image resolution is vastly superior to the 2DC laser imaging probe. For these reasons, the ice-crystal morphology quality and morphology statistics in the Korolev et al. study are considered superior to those of Table 3. For $D > 40 \mu\text{m}$, it was found that on average, monocrystalline or pristine habits comprised only 3.0% of the total particles sampled (95655). Pristine habits were defined as single columns or plates. Non-pristine habits were primarily faceted polycrystalline particles having planar or columnar components, or sublimated varieties of these crystals (producing rounded features). The

measurements were from 14 different flights (eight days) in cirrus and stratiform clouds associated with frontal systems, with temperatures ranging from 0 to -45 °C. The Korolev et al. results are summarized as a function of cloud temperature in Table 4 below.

Table 4: Frequency of occurrence of pristine ice particles in Arctic clouds (from Korolev et al., 1999)

Temperature (°C)	Total Cloud Length (km)	Total Number of Particles > 40 µm	Pristine ice > 40 µm (%)
-45 < T ≤ -40	820	8403	8.4
-40 < T ≤ -30	1101	26836	3.5
-30 < T ≤ -20	1182	20079	4.0
-20 < T ≤ -10	1191	28579	1.3
-10 < T ≤ 0	332	11758	0.7
TOTAL	4626	95655	3.0

Preliminary results from CPI measurements over the Great Lakes region of the U.S. indicate that pristine ice-crystal shapes occur in similar percentages there as in the arctic (Korolev et al., 1999).

The most recent investigation of the percentages of different particle shapes in ice clouds is also by Korolev et al. (2000), but it uses a different methodology and considers more flights, including flights over the North Atlantic near Newfoundland and over the Great Lakes. The data were collected in stratiform clouds usually associated with frontal systems. During two Arctic field programs, a number of flights sampled cirrus clouds. Temperatures ranged from 0 to -45 °C. This study only used particle images from the 2DC probe, and an ice-particle habit recognition algorithm was developed to classify crystals into the following shape categories: spheres, irregulars, needle/columns, or dendrites. By using only four basic categories, it was demonstrated that the algorithm could discriminate between categories and classify ice particles successfully. Bullet rosettes having three to five branches were included in the needle/column category. The dendrite category included dendrites, stellar crystals and aggregates of dendrites. Irregulars include particles having an irregular or random shape, such as polycrystalline particles comprised of planar and/or columnar components, heavily rimed particles, and other particles not classified in the other categories. Due to the 25-µm pixel resolution of the 2DC probe, the category of hexagonal plates was not included in this analysis. To allow sufficient pixels for shape characterization, only particles with $D > 125 \mu\text{m}$ were considered. Moreover, particles were classified as a function of size into one of three categories: $125 < D \leq 250 \mu\text{m}$, $250 < D \leq 500 \mu\text{m}$, and $D > 500 \mu\text{m}$. A total of 5,192,344 particle images were classified, obtained from 35,841 km of in-cloud sampling. The results of this study are given below in Table 5.

It is noteworthy that most of the size distribution projected area in cirrus clouds is associated with ice particles having $D < 250 \mu\text{m}$. This is even more true for number concentration. Hence, based on Table 4 and Table 5, irregular ice crystals in cirrus clouds should constitute ~90% of the concentration and projected area of cirrus particle size spectra.

Table 5: The frequency of occurrence of ice particle habits over the four projects: BASE, CFDE I, CFDE III, and FIRE ACE for the three size ranges: $D > 125$, $D > 250$, and $D > 500 \mu\text{m}$ (from Korolev et al. 2000).

Temperature Range ($^{\circ}\text{C}$)	% Spheres			% Irregulars		
	125 μm	250 μm	500 μm	125 μm	250 μm	500 μm
$0 > T > -5$	13	11	10	69	63	52
$-5 > T > -10$	14	10	9	69	65	58
$-10 > T > -15$	6	5	4	75	71	64
$-15 > T > -20$	8	9	10	84	83	80
$-20 > T > -25$	7	7	9	87	88	84
$-25 > T > -30$	6	3	6	90	94	88
$-30 > T > -35$	3	2	8	93	96	86
$-35 > T > -40$	1	0	3	95	97	85
$-40 > T > -45$	0	0	0	91	89	80
$0 > T > -45$	7	5	6	84	83	76
Temperature Range ($^{\circ}\text{C}$)	%Needles / Columns			% Dendrites		
	125 μm	250 μm	500 μm	125 μm	250 μm	500 μm
$0 > T > -5$	13	15	18	5	11	20
$-5 > T > -10$	10	9	8	8	16	24
$-10 > T > -15$	7	4	3	12	20	28
$-15 > T > -20$	6	3	3	3	4	6
$-20 > T > -25$	5	3	3	1	2	4
$-25 > T > -30$	4	2	4	0	1	2
$-30 > T > -35$	4	2	4	0	0	2
$-35 > T > -40$	4	2	10	0	0	2
$-40 > T > -45$	9	11	19	0	0	1
$0 > T > -45$	6	6	8	3	6	10

In summary, these studies indicate that irregular, polycrystalline ice dominates in cirrus and other ice clouds, and that the components of these polycrystals may be either columnar (i.e. bullet rosettes) or planar (i.e. planar polycrystals). The two Korolev et al. studies indicate that polycrystals are so dominant that to a good approximation, one could represent ice-cloud particle morphology through these two shapes: planar polycrystals and bullet rosettes. If so, the question then becomes: how are these two shapes apportioned in ice clouds, and what is the influence of each on upwelling radiance?

2.3.1.3 Projected-Area and Mass-Dimensional Relationships

The last section provided an inventory of ice crystal shapes commonly found in ice clouds, along with assessments of their relative abundance. This section will evaluate the impact of different shapes on cloud visible optical depth τ and TIR emissivity ε by investigating particle-shape-dependent P-D and m-D relationships (see Eqs. (1) and (2)). Even if they appear distinctly different visually, if two ice-particle shapes have the same P-D and m-D relationships then the τ and ε corresponding to homogeneous populations of each shape will be almost the same (Mitchell and Arnott 1994; Mitchell et al. 1996; Mitchell 2000a). This is because τ is twice the

size distribution (SD) total projected area, or $\tau = 2P_t$, and ε is a function of P_t and the effective photon path d_e of an ice particle. Effective photon path is formally defined as

$$d_e = V / P, \quad (3)$$

where $V = m/\rho_i$ is the volume of the ice crystal of density $\rho_i = 0.92 \text{ g cm}^{-3}$ (bulk ice density). In other words, V is the ice crystal volume at bulk density. Thus, ε depends on both m and P , and to a good approximation is defined by the m-D and P-D relationships and the size distribution (Mitchell et al. 1996; Mitchell 2000b).

Let us now examine the m-D and P-D power law relationships corresponding to the relevant crystal habits identified in the previous section: bullet rosettes, planar polycrystals, hexagonal plates, and columns. Thanks to the courtesy of Dr. Andy Heymsfield, the most current and accurate information on bullet rosettes is available to us. In Heymsfield et al. (2000), henceforth H00, relationships between ice-particle mass (or effective density) and area (or area ratio) were determined for a variety of ice particle shapes, using measurements from field studies and other sources. These relationships were tested for two case studies conducted in cirrus layers over the DOE ARM site in Oklahoma. The CPI probe quantified ice particle shape, and revealed that the ice particles were primarily bullet rosettes during each flight (on the flight of March 9th, ice particles were almost exclusively bullet rosettes). The clouds were sampled during vertical profiling by the Citation aircraft (i.e., Lagrangian or “step-down” descents). Accurate measurements were made of cloud ice water content (IWC) by a counter-flow virtual impactor, or CVI (Twohy et al. 1997). The IWCs determined from the effective density and area ratio relationships and the measured SD were compared with those measured by the CVI. These two determinations of IWC exhibited excellent agreement during both case studies, providing considerable confidence in the integrity of the mass and area relationships developed for bullet rosettes. H00 reported an m-D power law for rosettes (based on these case studies), and from the equations given in H00, a corresponding P-D power law was also determined analogous to Eqs. (1) and (2). These m-D and P-D expressions are listed in Table 6.

Also shown in Table 6 are the m-D and P-D expressions for planar polycrystals, and hexagonal plates and columns, taken from Mitchell et al. (1996). Random orientation is assumed for columns and plates. It is seen that the area expressions for bullet rosettes, planar polycrystals and hexagonal plates are similar, while those for hexagonal columns are considerably different. The mass expressions for plates and planar polycrystals are identical for $D > 100 \text{ }\mu\text{m}$, since the masses for side planes (a type of planar polycrystal) and plates were very similar. To extrapolate for $D < 300 \text{ }\mu\text{m}$, the smallest measured size for side planes, the plate relationship was used.

These expressions are plotted in Figure 3 for projected area and in Figure 4 for ice crystal mass. Now it is clear that the projected area and mass relationships are similar for all ice crystals excepting hexagonal columns. In Figure 3, the planar-polycrystal/bullet-rosette projected area ratio ranges from 0.82 to 0.86, while the hexagonal plate/bullet rosette projected area ratio is close to unity throughout the range of D ($5 \text{ }\mu\text{m}$ to $1000 \text{ }\mu\text{m}$). Only hexagonal columns exhibit significant deviation, but even this is modest in Figure 3. In Figure 4 however, the differences in mass between hexagonal columns and the other crystal types is considerable, indicating ice cloud radiative properties will be sensitive to a change in shape to hexagonal columns. Column masses are less than for other shapes when $D > 500 \text{ }\mu\text{m}$. However these sizes generally contribute a relatively small amount to SD mass in most cirrus (due to low concentrations), so that the total SD mass is generally greater for a given SD that contains columns versus some other shape(s).

OVERVIEW AND BACKGROUND INFORMATION

On the other hand, for a given D , the mass of bullet rosettes, planar polycrystals and hexagonal columns is extremely similar for $D < 400 \mu\text{m}$, a size regime that accounts for the bulk of the SD area and mass for most cirrus clouds.

In summary, Figure 3 and Figure 4 indicate that, based on current information, the projected area and mass relationships for bullet rosettes, planar polycrystals and hexagonal plates are very similar, and that significant changes in ice cloud radiative properties are not likely to result as the relative abundance of these crystal types vary in a cloud. A change in cloud microphysics promoting hexagonal columns, on the other hand, is likely to produce a significant change in cloud radiative properties (e.g., τ , ϵ , and single scattering albedo ω); however, hexagonal columns appear to represent a minor fraction of the ice particle population in most ice clouds.

Table 6: Constants used in the projected-area and mass-dimensional power laws (see Equations (1) and (2)) for hexagonal columns and plates, bullet rosettes, and planar polycrystals. All units are cgs

Ice-Particle Shape	Size Range	Projected Area (cm^2)		Mass (g)	
		γ	σ	α	β
Bullet Rosettes	$D \leq 100 \mu\text{m}$	0.2839	1.889	0.0260	2.750
	$D > 100 \mu\text{m}$	0.2839	1.889	0.0260	2.750
Planar Polycrystals	$D \leq 100 \mu\text{m}$	0.2285	1.880	0.05801	2.879
	$D > 100 \mu\text{m}$	0.2285	1.880	0.007389	2.449
Hexagonal Plates	$D \leq 100 \mu\text{m}$	0.2395	1.855	0.04953	2.852
	$D > 100 \mu\text{m}$	0.2395	1.855	0.007389	2.449
Hexagonal Columns	$D \leq 100 \mu\text{m}$	0.6837	2.00	0.2515	3.00
	$D > 100 \mu\text{m}$	0.0459	1.415	0.001658	1.91

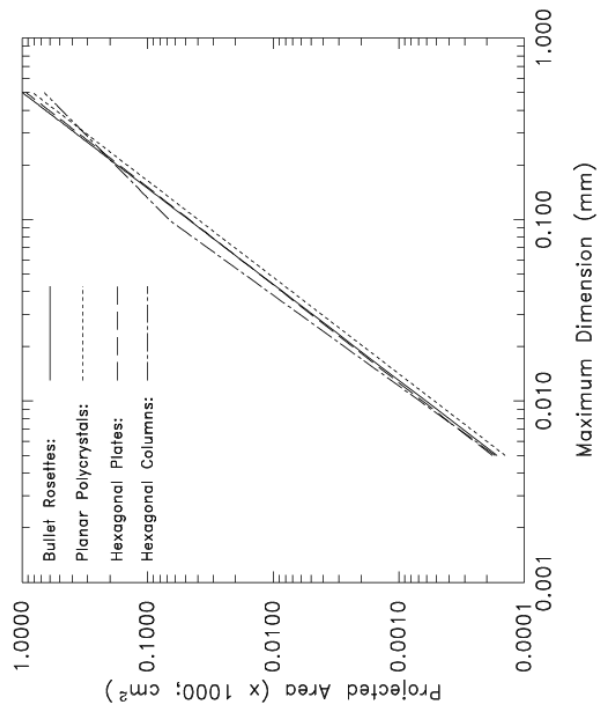


Figure 3: Projected area as a function of maximum particle size.

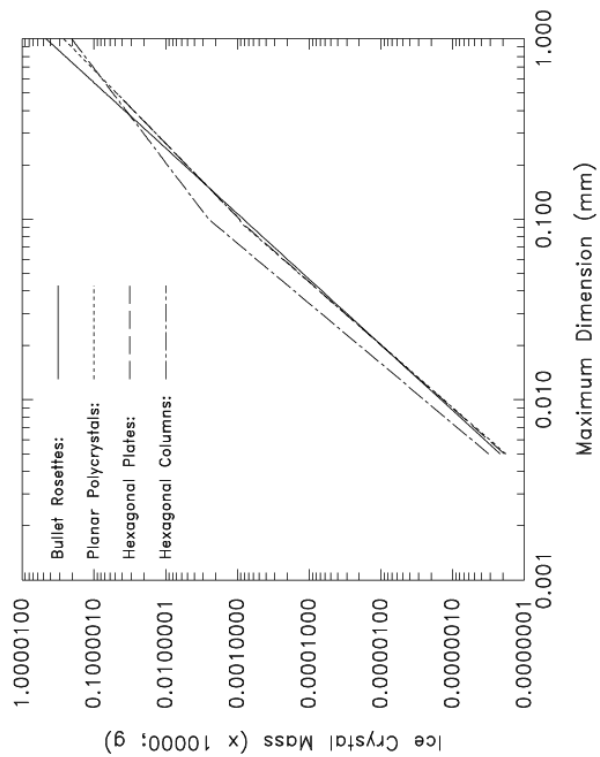


Figure 4: Ice crystal mass as a function of maximum particle size.

2.3.1.4 Sensitivity of Cloud Emissivity to Natural Variability in Ice Particle Shape

This section examines how cloud emissivity is affected by observed variations in ice particle shape. The two Korolev et al. studies in Section 2.3.1.2 indicate that for $T < -20^\circ\text{C}$, about 90% or more of the ice crystals are bullet rosettes and planar polycrystals. However, Table 3 indicates considerably higher percentages of columns and plates. To be conservative and provide a possibly high estimate of the emissivity uncertainty due to shape effects, the percentages in Table 3 will be used in this analysis. But first, a means of treating mixtures of ice particle shapes in our radiation code must be determined.

2.3.1.4.1 Calculating absorption and extinction for mixtures of ice particle shapes

The approach here is to determine m-D and P-D relationships for any given mixture of ice-particle shape. The constants corresponding to these power laws (see Eqs. (1) and (2)) are used in the absorption and extinction efficiency codes in a fundamental way, so it is best to determine single values of α , β , γ and σ for the entire non-homogeneous mixture of ice-crystal shapes. This simplifies the efficiency calculations considerably.

As shown in Table 6, the m-D and P-D relationships often change for a given crystal type at $D = 100\ \mu\text{m}$. Therefore a set of mass or area constants is determined for $D < 100\ \mu\text{m}$ and $D > 100\ \mu\text{m}$, which apply to a given mixture of ice particle shapes. Since it is a given that m and P are related to D via a power law, m and P can be determined at selected D values and used to define a line in log-log space. The D values used for a given shape, giving one or two line equations, are: $10\ \mu\text{m}$, $100\ \mu\text{m}$, $1000\ \mu\text{m}$. For a given D value and mixture of shapes, the crystal mass is given as

$$m_{\text{mix}} = m_{\text{ros}} (F_{\text{ros}}/F_t) + m_{\text{pp}} (F_{\text{pp}}/F_t) + m_p (F_p/F_t) + m_c (F_c/F_t), \quad (4)$$

where ros, pp, p and c refer to rosettes, planar polycrystals, plates, and columns, respectively; F_x refers to the fraction or percentage of a given shape listed in Table 1, and F_t is given as

$$F_t = F_{\text{ros}} + F_{\text{pp}} + F_p + F_c. \quad (5)$$

Note that the “miscellaneous” category in Table 3 (FIRE 2) was not included in this analysis. It is necessary to assume here that a given shape portion F_x applies equally over all particle sizes in a size distribution (SD). For a given crystal size and shape, m is determined from Table 6. In this way, m_{mix} is determined for the three D values noted above. If $D_1 = 10\ \mu\text{m}$ and $D_2 = 100\ \mu\text{m}$, then

$$\beta_{\text{mix}} = (\ln m_{\text{mix},2} - \ln m_{\text{mix},1}) / (\ln D_2 - \ln D_1), \quad (6)$$

and

$$\alpha_{\text{mix}} = \exp (\ln m_{\text{mix},2} - \beta_{\text{mix}} \ln D_2). \quad (7)$$

Equations analogous to (6) and (7) can be written for $D > 100\ \mu\text{m}$. The procedure for determining the projected-area power law constants γ_{mix} and σ_{mix} is analogous to this procedure.

Emissivities, or ε , were calculated in the radiation scheme (Mitchell 2000b) using the zero-scattering approximation, as this was found to yield emissivities within about 2% of ε determined when scattering effects were included:

$$\varepsilon = 1 - \exp(-\tau_{\text{abs}}). \quad (8)$$

The absorption optical depth τ_{abs} is the product of the cloud depth and the absorption coefficient of the model cloud, which depends on the given SD, wavelength, and ice-particle shape.

2.3.1.4.2 Results: Dependence of D_{eff} and emissivity on crystal shape

Modifying the radiation code to simulate a mixture, or “recipe” of crystal shapes using Eqs. (4)-(7) and the habit percentages listed in Table 3 yielded α , β , γ and σ for each shape mixture, from which emissivities were calculated for a given cloud ice water content (IWC) and size distribution. The size distribution parameterization of Ivanova et al. (2000) for mid-latitude cirrus was used, where the mean D of the large-particle mode, D_{large} , was 100 μm . A typical IWC of 0.010 g m^{-3} was assumed, and the cloud thickness was 1 km. The photon-tunneling factor was 0.5 for the small-particle mode of the size distribution (SD), and 0.0 for the large-particle mode.

The effective diameter of a SD is defined in this radiation scheme (Mitchell 2000b) as

$$D_{\text{eff}} = 3 \text{ IWC} / (2 \rho_i P_t), \quad (9)$$

where P_t is the total projected area of the SD. D_{eff} is plotted in Figure 5 for the 16 flights indicated in Table 3, in chronological order. Since the IWC and size distribution were fixed, all changes in D_{eff} are due to changes in ice-crystal shape. The largest D_{eff} values occur on flight numbers 6 and 7, the only flights where columns dominated. This is because, for a given D , columns contain more mass than the other shapes, giving lower number concentrations N and geometric cross sections P_t when IWC is fixed. Figure 3 and Figure 4 indicate that while P differences are modest, mass differences between columns and the other shapes are considerable (note different scales). It is these mass differences over this range of sizes that primarily account for differences in D_{eff} through their impact on N and P_t at fixed IWC. Also apparent in Figure 5 is that D_{eff} is generally greater for the FIRE 1 flights relative to the FIRE 2 flights. This is due to columns generally being more abundant during FIRE 1. An exception is the 5th flight, where a corresponding minimum in D_{eff} is observed. While columns were generally less abundant during FIRE 2, an exception was flight 15, and a corresponding increase in D_{eff} is found there. Hence the differences in D_{eff} are consistent with the P - D and m - D relations shown in Figure 3 and Figure 4, and the percentages shown in Table 3.

Emissivities ε at a wavelength λ of 3.85 μm for the flight numbers are shown in Figure 6. Absorption at this wavelength depends on D_{eff} in two ways: (1) the absorption efficiency Q_{abs} for the SD depends on D_{eff} , and (2) the SD projected area P_t also depends on D_{eff} . This strong D_{eff} dependence is shown in Figure 6, where the variation in ε is the inverse of the variation in D_{eff} in Figure 5. Hence, the behavior of ε in Figure 6 is entirely consistent with the percentages in Table 3. The uncertainty that natural variations in crystal shape impart to ε is more clearly appreciated in Figure 7, where percent differences from the mean ε are given by flight number. The cirrus conditions were chosen to yield $\varepsilon < 0.5$, since this provides for optimal sensitivity of ε to cloud microphysics. It is seen that changes in ε span a range of about 10%, with deviations from the mean within 6%.

This analysis was also carried out for a size distribution with a D_{large} of 300 μm , which is common for relatively broad size spectra found in cirrus. At larger sizes ($D > 250 \mu\text{m}$), Figure 4 shows mass for columns becoming comparable with other crystal shapes, while plate and planar polycrystal masses become increasingly less relative to bullet rosettes. For this reason the dependence of ε on ice crystal shape may be different when larger D characterize the SD. Figure

8 gives ε for the flights in Table 3, based on the same conditions as before, except D_{large} is 300 μm and the cloud depth is now 1.5 km. As anticipated, the ε pattern is different than before, due to the larger D_{large} . The first 8 flights from Table 3 (i.e., FIRE 1) generally exhibit higher D_{eff} (not shown) and lower ε than the FIRE-2 flights. Part of this is due to higher column percentages as before, but this alone cannot explain the relatively low ε of the first 3 flights. These lower emissivities are also due to the difference between rosette and planar polycrystal masses at these larger sizes. Since rosettes were dominating and columns were relatively abundant, ε was lower for these three flights (due to the relative mass differences between plates and polycrystals). Similar reasoning can be applied to explain the behavior of ε as a function of ice crystal shape for the other flights. Finally, Figure 9 illustrates the corresponding percent differences with respect to mean ε . Again, changes in ε were confined within a range of 10 percentage points, with deviations from the mean being $< 6\%$.

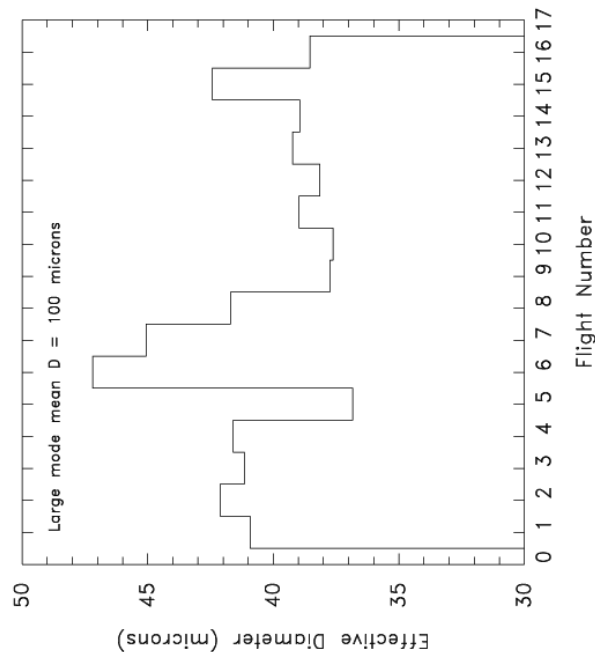


Figure 5: Effective diameter of a size distribution for the 16 flights listed in Table 3.

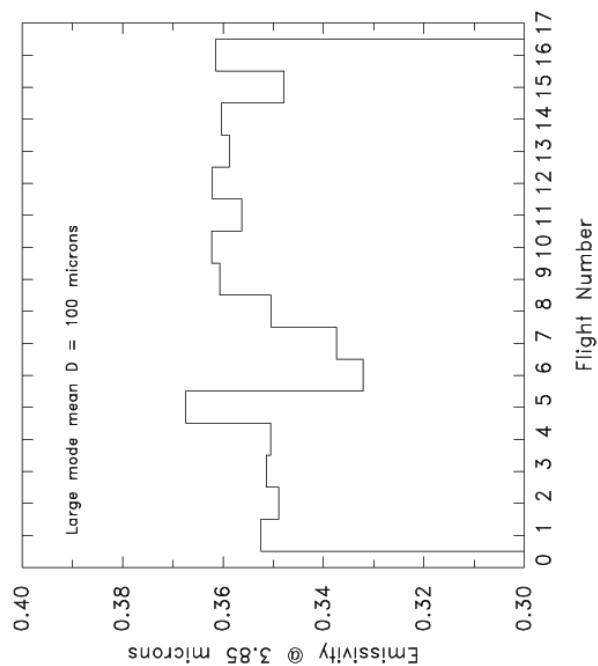


Figure 6: Emissivity at 3.85 μm for the flights listed in Table 3 for a mode mean of 100 μm .

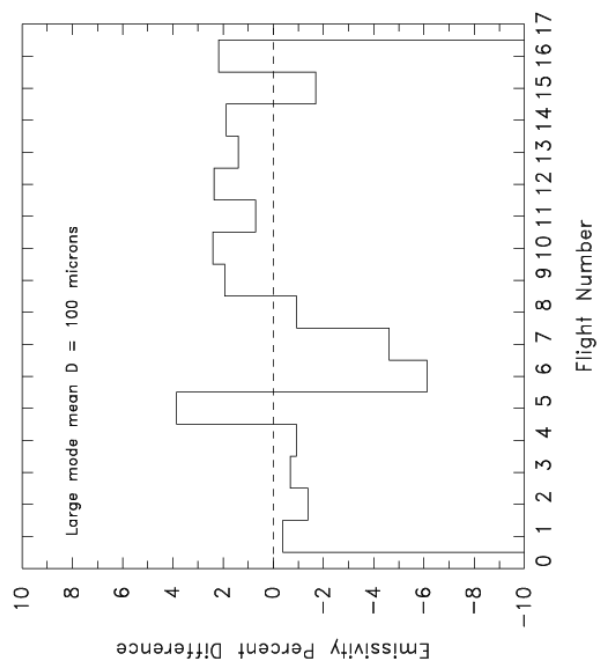


Figure 7: Percent difference of the actual emissivity from the mean shown in Figure 6.

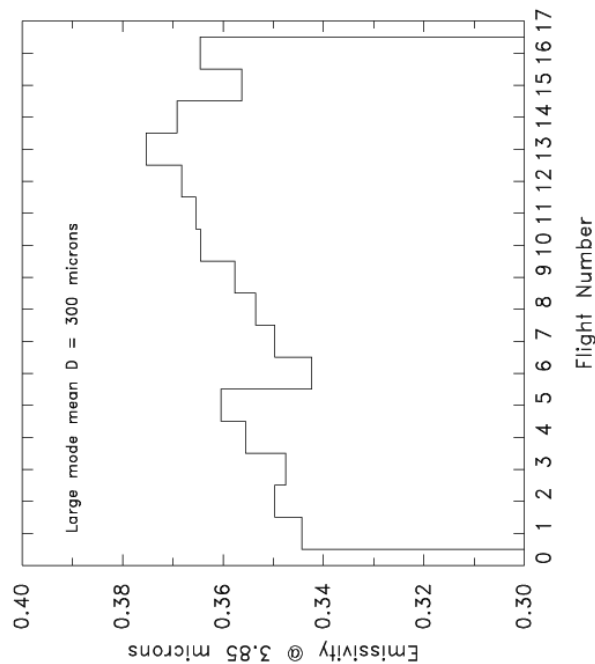


Figure 8: Emissivity at 3.85 μm for the flights listed in Table 3 for a mode mean of 300 μm .

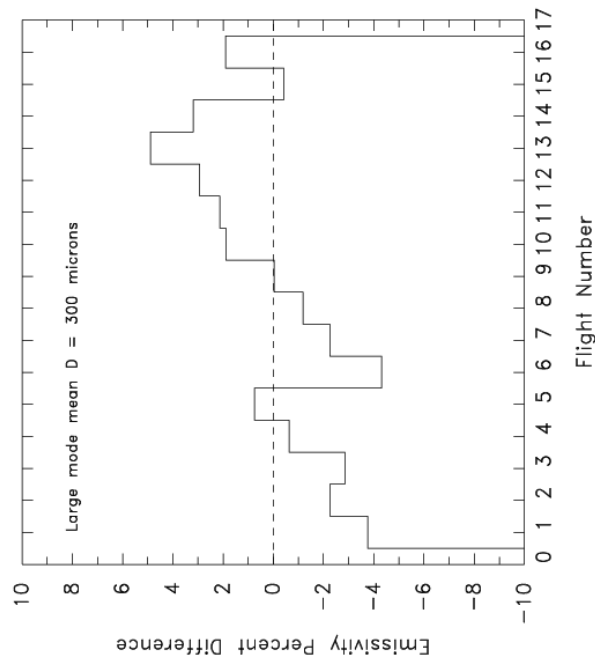


Figure 9: Percent difference of the actual emissivity from the mean shown in Figure 8.

2.3.1.5 Summary and Conclusions

Earlier work (e.g. Mitchell et al., 1996) indicated that ϵ was a strong function of ice particle shape. However, that was largely due to the mass and area expressions used for bullet rosettes, a crystal type difficult to characterize due to uncertainties in the aspect ratio of rosette branches and the number of branches. The recent work of Heymsfield et al. (2000) has provided better m-D and P-D expressions for bullet rosettes, validated against two cirrus case studies with CVI

measurements of IWC. As a result, it now appears there is little difference between cirrus ice-crystal shapes regarding mass and projected area, with the exception of hexagonal columns. Nonetheless, these findings are not conclusive, and only represent our best knowledge to date.

The above analysis indicates that for the observed variability in cirrus ice crystal habit, the cirrus emissivity should be within about $\pm 5\%$ of the mean ϵ . This low sensitivity to particle shape is largely due to the fact that hexagonal columns are generally a minor species in ice clouds. Two of the three studies examined in Section 2.3.1 attributed much smaller percentages to columns regarding their abundance in ice clouds than the first study (i.e., Table 3). Since this uncertainty analysis is based on the first study, the $\pm 5\%$ uncertainty estimate for ϵ is considered high.

These findings do not apply to solar retrievals where the scattering phase function of an ice particle also needs to be considered. However, it is likely that the dominance of irregularly shaped ice particles in ice clouds will produce a featureless phase function, as many observations have indicated, allowing the simplifications found here to be extended to solar wavelengths.

Finally, it is noted that some treatments of ice-cloud single scattering properties are based on hexagonal columns. In addition to being uncommon, the extinction and absorption properties of hexagonal columns appear dissimilar to the ice-particle types most common in ice clouds.

2.3.2. Ice Crystal Size Distributions in Natural Cirrus

In this section is discussed the observed attributes of cirrus particle size distributions, ice-crystal particle sizes, and ice-water-content observations in natural non-precipitating cirrus taken during CEPEX and ARM.

2.3.2.1 Bi-Modal Size Distributions

It has been well established in numerous journal articles that the size distribution of ice clouds in frontal systems tends to be exponential, at least for the mid-to-large particle sizes (e.g. Lo and Passarelli, 1982). More recently it has become apparent that ice particle size distributions are bimodal, in the sense of having a large and small-particle mode, with the large mode being exponential (e.g., $v \sim 0$; see Heymsfield and Platt, 1984; Ryan, 1996; Platt, 1997; McFarquhar and Heymsfield, 1997).

The gamma size distribution has form

$$N(D) = N_0 D^v e^{-\Lambda D}, \quad (10)$$

where N_0 is related to the ice-water content IWC and number concentration N , D is the ice-crystal maximum dimension, v is the dispersion parameter, and Λ is the slope parameter.

Figure 8 contains a size distribution sample in log-linear space, which has the form given by Eq. (1) and is typical of ice crystals measured in tropical anvil cirrus during CEPEX (McFarquhar and Heymsfield, 1996; 1997). Note that the slope of the line in log-linear space is steeper for crystals with $D < \sim 100 \mu\text{m}$ than it is for $D > \sim 100 \mu\text{m}$. This slope is the slope parameter Λ in Eq. (1), since for tropical cirrus it is observed that $v = 0$. When v is large the size distribution is narrow (i.e., a low dispersion), and when v is small the distribution is wide (a high dispersion).

Figures 9, 10, and 11 contain plots of observed size distributions from mid-latitude cirrus observations taken during the ARM campaign in the spring of 1994. Note that the distributions

are clearly bi-modal, as they are for the tropics, and that the dispersion and slope parameters v and Λ also vary with cirrus temperature. As is verified in these figures, it is generally accepted that boundary separating the “large” and “small-particle” modes of bi-modal ice-crystal size distributions lies at $D = 100 \mu\text{m}$.

Fortunately, a means of estimating particle sizes in tropical anvil and mid-latitude cirrus has been exploited by Ivanova et al. (2000). For the large-particle mode, the ice-crystal mean maximum dimensions $\underline{D}_{\text{large}}$ for tropical and mid-latitude cirrus are given by

$$\text{Tropics: } \underline{D}_{\text{large}} = 1031 e^{0.05522 (T-277)} \quad (11)$$

and

$$\text{Mid-latitudes: } \underline{D}_{\text{large}} = 440.2 e^{0.02290 (T-273)}, \quad (12)$$

where $\underline{D}_{\text{large}}$ has units μm and the cirrus temperature T is Kelvins. Equation (11) is based on 93 size distributions from three CEPEX tropical anvils (McFarquhar and Heymsfield, 1996), three tropical anvils reported in Knollenburg et al. (1993), and a tropical tropopause case (Heymsfield, 1986). The mid-latitude Eq. (12) is based similarly on over 1000 in-situ observations of cirrus taken during ARM and FIRE flights in the central U.S. The correlation coefficient r between T and $\underline{D}_{\text{large}}$ in (11) is $r = 0.959$, with $r^2 = 0.920$ (i.e., 92% of the variance explained).

The gamma distribution $N(D)$ given by Eq. (10) has mean $(v+1)/\Lambda$ and variance $(v+1)/\Lambda^2$. Thus the slope parameter Λ for the large-particle mode is given by

$$\Lambda_{\text{large}} = (v_{\text{large}} + 1) / \underline{D}_{\text{large}}, \quad (13)$$

with $v_{\text{large}} = 0$ for the tropics, and $v_{\text{large}} = 2.2 \pm 1.7$ (i.e., the dispersion-parameter distribution has a standard deviation of 1.7) for mid-latitudes. Similarly

$$\Lambda_{\text{small}} = (v_{\text{small}} + 1) / \underline{D}_{\text{small}}. \quad (14)$$

For the tropics $v_{\text{small}} = 0$, and for mid-latitudes $v_{\text{small}} = 3.72 \pm 1.01$. Data on polar cirrus clouds are sparse and are likely not statistically meaningful.

Interestingly it turns out that in the tropics the small-particle slope parameter is linearly proportional to that for the large-particles:

$$\text{Tropics: } \Lambda_{\text{small}} = 1.49 \Lambda_{\text{large}} + 583, \quad (15)$$

and

$$\text{Mid-latitudes: } \Lambda_{\text{small}} = 1589.23 \text{ cm}^{-1} \text{ (constant)}. \quad (16)$$

Equation (15) was obtained for tropical cirrus anvils using in-situ SD observations that were adjusted such that subsequent model predictions of TOA radiance using Λ_{small} and Λ_{large} matched observations. Equation (16) corresponds to $\underline{D}_{\text{small}} = \text{const} = 29.7 \mu\text{m} \pm 3.0 \mu\text{m}$ based on the 1000 $N(D)$ observations for mid-latitude cirrus only. The correlation coefficient r between Λ_{small} and Λ_{large} in (15) is $r = 0.86$, with $r^2 = 0.74$ (i.e., 74% of the variance explained).

2.3.2.2 Mass-Median Particle Sizes

Mass-median particle size is defined as the sphere-equivalent diameter that divides the mass of the ice-crystal size distribution in half. It is computed by numerically integrating the large and

small modes of the size distribution given by Eqs. (10)-(16), through which the slope parameter Λ is computed as a function of cirrus environmental temperature T and the dispersion parameter is a function of geographic region (i.e., tropics or mid-latitudes).

For the mid-latitude FIRE and ARM cirrus ice-crystal observations, D_{me} ranges between 127 and 487 μm for cirrus temperatures between 210 and 258 K. For the tropical CEPEX observations, D_{me} ranges between 27 and 1126 μm . Table 5 lists the mass-median particle sizes for the range of observed cirrus temperatures 210-258 K.

Table 7: Sphere-equivalent mass-median particle sizes for the ARM/FIRE mid-latitude and CEPEX tropical ice-crystal observations

Cirrus Temperature (K)	D_{me} (μm) Tropics	D_{me} (μm) Mid-latitudes
200	27	127
210	42	164
220	79	207
230	189	259
240	428	324
250	755	406
258	1126	487

2.3.2.3 Ice-Water Content

The concept of effective particle sizes for the large and small modes of the size distribution $N(D)$ can be extended to describe the portion of the total cirrus ice mass that is contributed by the small and large modes. Using the 1000 mid-latitude and 96 tropical in-situ observations of cirrus ice-crystal size distributions, the normalized ice-water content of the tropical cirrus small mode is partitioned as

$$\text{Tropics: } IWC_{\text{small}} = 0.025 + 0.975 \exp \left[- (\underline{D}_{\text{large}} / 80)^2 \right], \quad (17)$$

and for mid-latitudes by

$$\text{Mid-latitudes: } IWC_{\text{small}} = 0.11 + 0.89 \exp \left[- (\underline{D}_{\text{large}} / 50)^2 \right], \quad (18)$$

where $\underline{D}_{\text{large}}$ is given by Eq. (11) (for (17)) and by Eq. (12) (for (18)), and has units of μm . The normalized large-mode portion is simply

$$IWC_{\text{large}} = 1 - IWC_{\text{small}}. \quad (19)$$

Note that, in the asymptotic limit where $\underline{D}_{\text{large}}$ approaches ∞ , $IWC_{\text{small}} \approx 0.025$ (0.11) for tropical (mid-latitude) cirrus. In other words, when the large-mode crystals are “very big” (most likely in lower levels of a cirrus cloud), the small-mode crystals contribute only 2.5% (11%) of the total tropical (mid-latitude) cirrus ice mass. This information can be added quantitatively to the error budget and error covariance matrices of the UR IWP retrievals.

The normalized IWCs given by Eqs. (17) - (19) can be related directly to cirrus temperature via Eqs. (11) and (12). Table 6 lists the small-mode IWC portions for tropics and mid-latitudes as a function of cirrus temperature.

Table 8: Small-mode normalized ice-water contents for the ARM/FIRE mid-latitude and CEPEX tropical ice-crystal observations. Large-mode portions are computed simply as $IWC_{large} = 1 - IWC_{small}$

Cirrus Temperature (K)	IWC_{small} Tropics	IWC_{small} Mid-latitudes
200	0.97	0.17
210	0.91	0.12
220	0.74	0.11
230	0.41	0.11
240	0.08	0.11
250	0.03	0.11
258	0.03	0.11

In the case of the tropics, the finding that only 2.5% of the total cirrus ice mass is contributed by the small-mode crystals is defensible in that the large ice crystals of a precipitation-bearing thunderstorm cloud are growing via aggregation at the expense (i.e., depletion) of smaller crystals.

In the case of mid-latitude cirrus, note that 11% of the total cirrus ice mass is taken up by the small modes at nearly all but the very lowest cirrus temperatures.

2.3.2.4 Precipitating Cirrus

As for precipitating cirrus, using high-end IWC values per 1-km layer beginning at 273 K and ending at the mid-latitude tropopause, the total cirrus IWP is computed to be only $\sim 860 \text{ g m}^{-2}$. Thus for the vast majority of situations likely to be encountered in nature, frontal snowstorms are already included in the CMIS IWP algorithm retrieval range. In the lower levels of frontal-system clouds, "equilibrium" snow size spectra develop that have a constant actual mean size of about 1 mm, or a median mass dimension, D_{me} , of about 3 mm. This yields a D_{me} of about 1 mm after converting the non-spherical snowflake to its sphere-equivalent mass-median size. Thus the range of D_{me} used in the CMIS UR simulations is also likely to be inclusive.

As for crystal shapes in frontal snowstorms, Korolev et al. (2000) show that pure shapes such as dendrites or columns may become dominant only within the narrow convective cells that produce the bands of heavy precipitation, but irregular crystals dominate elsewhere in the cloud. Thus, if one is concerned about radiation issues (i.e., ensuring that crystal shape distributions are spatially representative at all levels within the cloud) and not precipitation, then it is best to assume irregular habits at all levels, even in the warmer regions of the cloud. While such regions typically have about 70% irregulars as opposed to 90% for cirrus, the irregular-shape assumption is still not too bad.

2.4. Channel Selection

Figure 10 illustrates that the opacity of the atmosphere increases with frequency due to H_2O absorption and thus limits the usefulness of far IR frequencies beyond $\sim 1000 \text{ GHz}$. Also, absorption by ice particles increases toward the center of the H_2O rotational band.

Figure 11 shows the transmission from the top of the atmosphere down to four different altitudes for the sub-millimeter region, which is defined as the domain where the wavelength is less than one millimeter and more than 0.1 mm (i.e., corresponding to 10 to 100 cm^{-1} , or 300 to 3000 GHz). It is clear that a series of H_2O and O_2 absorption lines the drastically reduce the transmission. The 60 GHz oxygen line is used by MSU to determine the temperature profile and

the 183 GHz H₂O line is used to measure the water vapor profile. The baseline CMIS instrument design includes frequencies up to 183 GHz, but there is an option to include higher frequencies in the sub-millimeter spectral region.

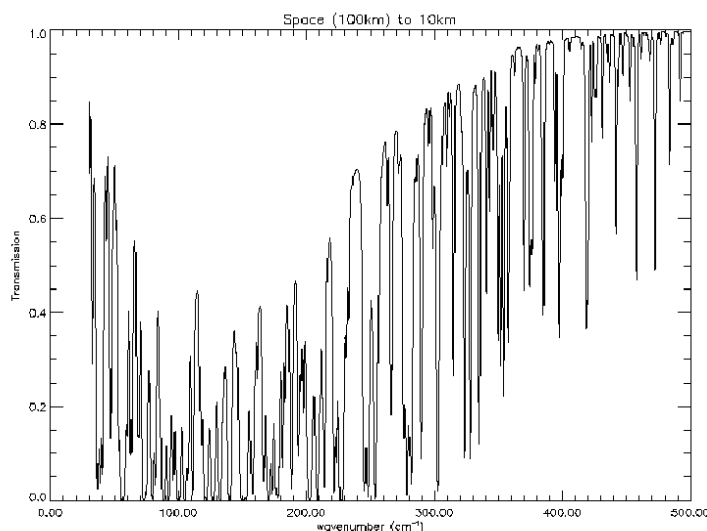


Figure 10: Atmospheric transmission for a vertical path from 10 km to the top of the atmosphere.

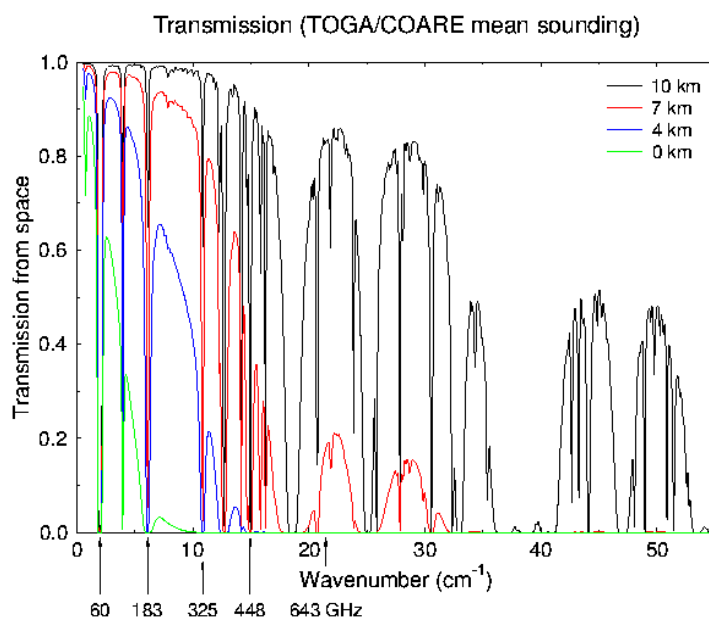


Figure 11: Transmission from high altitude down to four different altitudes. Courtesy of Frank Evans [Evans, 2000].

2.4.1. Computation of Optical Properties

The electromagnetic scattering properties of ice particles are generally computed using the Lorentz-Mie theory where the ice particles are assumed to be spherical (or approximated by

equivalent spheres). This is not necessarily a good approximation and the polarization signal can not be modeled with these assumptions.

Evans and Stephens (1995) studied the single scattering properties of different ice particle shapes and size distributions. Their results indicate that crystal shape has a significant effect on the scattering: For the same effective ice particle size and ice content, the extinction can be a factor of three different for different crystal shapes. Further, the shape is the dominant effect in the polarization signal, where thinner shapes have a larger polarization signal. The characteristic particle size has a strong impact on the extinction and single scattering albedo.

2.5. Instrument Characteristics

2.6. Requirements for Cross-Sensor Data (NPOESS or Other Sensors)

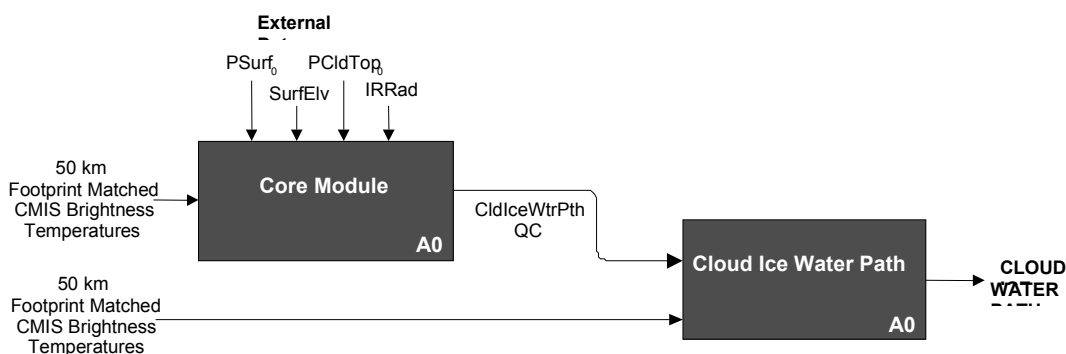
Cross-sensor data required for the CMIS retrievals is given in Table 9. Cloud top pressure information from CrIS or VIIRS is required to (1) detect ice and (2) improve the IWP retrieval. Because CMIS channels are not sensitive to small particles, the VIIRS IR radiances are also required to perform the retrieval of small values of IWP. Unless we perform a unified retrieval combining microwave-IR radiances, there will be errors introduced in the size distribution assumption.

Table 9: Sources of cross-sensor data required for CMIS.

Required Parameter	Data Source	Expected Uncertainty
Cloud Top Pressure	VIIRS/CrIS	50 mb
IR Radiances	VIIRS (as a minimum: at the 3.9 μ m and 10-12 μ m bands)	See Section 4.4

3. Microwave Algorithm Description and Performance

This section describes the microwave retrieval algorithm in non-precipitating cirrus clouds as well as in precipitating clouds. The ice water path in non-precipitating clouds is retrieved using a physical approach while in the precipitating cases, a neural network algorithm is adopted to retrieve the integrated ice water path. In both cases, the retrieval approach is described and the summary of the obtained performances is presented. The test dataset is also described in detail. Figure 12 shows the overview of the ice water retrieval. The core module runs first using the 50 kilometers footprint matched brightness temperatures and some external data. If the quality control (QC) detects no scattering due to ice or rain then the profile is assumed clear sky and an ice water path amount of zero is reported. If the QC detects scattering by cirrus ice, then we use the multiple scattering retrieval code to perform the retrieval of the non precipitating ice water path. If the QC detects precipitating conditions then we use a neural network algorithm to compute IWP. The integration of the IWP retrieval algorithm, in particular the switch between precipitating and non-precipitating clouds, is described in the “Overview: Integration ATBD (Volume I, Part I)”.



KEY		
<i>Products from CMIS Data</i>		
Input	Description	Source
CldIceWtrPth	Cloud Ice Water Path	Core Module
<i>Flags from CMIS Algorithm Output</i>		
Input	Description	Source
QC	Output Production Mode	Core Module
<i>Data from Sources External to CMIS</i>		
Input	Description	Example Source
PSurf ₀	Surface Pressure	NCEP or FNMOC NOGAPS
SurfElv	Surface Elevation	DTED
IRRad	IR Radiances	VIIRS
CldCvr	Cloud Cover Fraction	VIIRS Cloud Cover EDR
PCldTop ₀	Cloud Top Pressure	VIIRS Cloud Top Pressure EDR

Figure 12 Flow diagram of the ice water retrieval module.

3.1. Non-Precipitating Clouds

In non-precipitating clouds, the ice water path is retrieved as part of the geophysical state vector output by the core module (see the Core Module ATBD, vol. 2). The state vector is extended to include the ice water path, the particle size distribution median diameter, as well as the cloud top and cloud thickness. Currently, the derivatives are computed using the finite differences

technique. The performances of the IWP retrieval depend on several parameters summarized in Table 10. The sensor noise and the environmental conditions are included in the simulations and are part of the obtained performances. The impacts of the other sources of error (unknown concentration of small particles, particle shape/density, 3D effects and cell mismatch) were studied separately.

Table 10: Components of the IWP error budget.

Error Component	Description
Sensor Noise	<ul style="list-style-type: none"> Baseline 50 km spatial resolution HF channel noise = 0.3 K
Environmental conditions	<ul style="list-style-type: none"> Variable cloud thickness Vertical distribution of ice particles Width of ice particle distribution
Other Sources of Error	<ul style="list-style-type: none"> Unknown concentration of small particles Particle shape/density Cloud 3-dimensional geometry (convective type) Cell mismatch

3.1.1. Historical and Background Perspective of the IWP Retrieval

Visible sensors have been used to retrieve cloud ice water path in optically thin clouds (Rossow and Shiffer, 1991) while microwave instruments have been used for convective precipitating clouds (Virekanandan et al., 1991; Weng and Grody, 1994).

For the microwave, Weng and Grody (2000) used a simplified two-stream scheme model to retrieve IWP and the median diameter of the particle size distribution (D_{me}) assuming a certain bulk density (ρ). Their results were applied to two frequencies, 89 and 150 GHz (MIR on NASA ER-2), and they developed an analytical expression to approximate the radiance using approximations for IWP, D_{me} and ρ typical of the microwave region. However, uncertainties in ρ induce a large uncertainty in the IWP/ D_{me} retrieval because ρ varies from snowflakes, graupels, pristine crystals (for precipitating clouds).

Several guidelines have been proposed for an IWP retrieval algorithm (Evans and Stephens, 1995): (1) Clear sky radiances must be known, either by using nearby pixels or lower frequencies to simulate clear sky radiances. From this the characteristic size may be determined using ratios of ΔTB at different frequencies. (2) One can make a physical assumption about the characteristic particle size given the cloud temperature or adjacent successful retrievals. From this the particle shape can be determined based on ratios of ΔTB for different polarizations. Using these guidelines, Evans et al. (2001) developed and analyzed a method to retrieve IWP and characteristic particle size. The modeling of cirrus cloud was performed using seven parameters (IWP, D_{me} , Z_{top} , δZ , α , γ , β), where γ and β are the lapse rate of the vertical variation of D_{me} and the exponent relating the ice water content in each layer to the layer's D_{me} . Their results show that if the cloud top and height are known, the *rms* IWP average is about 30% for $25 \leq IWP \leq 800$ and $100 \leq D_{me} \leq 400$ (at nadir). For lower IWP or lower D_{me} , the error is much worse. If the geometry is unknown, then the error is significantly worse for clouds down 6 km.

3.1.2. Microwave Retrieval Approach for Non-Precipitating Clouds

The relationship between the measured brightness temperatures and the ice cloud properties depends not only on the ice parameters, but also on other environmental conditions (e.g., water vapor and cloud liquid water). The approach adopted by previous studies has been to account for these environmental conditions by including external data from NWP forecasts or radiosondes (Deeter and Evans, Liu and Curry, 2000). These environmental conditions may also be retrieved from radiometric data using low frequency channels, assuming that these channels are not affected by scattering by ice crystals (Weng and Grody, 2000).

Our baseline CMIS algorithm uses a physical approach that accounts for the simultaneous impact on the radiances from the cirrus cloud parameters and the environmental conditions. For non-scattering cases the inversion is performed as part of the core module using the maximum likelihood approach described in the core module ATBD. In scattering media, the state vector is augmented by the ice water path (IWP), mean mass diameter (Dme) of the size distribution, and the ice cloud top height and thickness. The ice cloud parameters are then retrieved simultaneously with the non-scattering parameters. The use of lower frequency channels in the inversion (i.e., the temperature sounding and window channels) provides information about both the atmospheric temperature and the cloud liquid water in the presence of ice (mixed phase or multi-layer cloud). This explicit treatment of multiple scattering makes it possible to model the ice effects in the high frequency channels (89 GHz and above) and produce the water vapor profile. The retrieved water vapor information along with the atmospheric temperature, cloud liquid water and surface properties, is taken into account in the IWP retrieval.

Several cloud parameters must be included in the forward simulation of the radiances to accurately simulate the measured radiances. In the retrieval however, only some of the parameters need to be considered. Thus although the ice water path is the only required EDR, the Dme and the cloud top must also be retrieved to avoid large errors due to incorrect assumptions concerning the values of these parameters. The values of other parameters such as the particle size distribution width (or variance) may be fixed to reasonable values, with little impact on the retrieval results.

3.1.2.1 Particle Size Distribution (Dme) as a Secondary Retrieval Product

The extinction of radiation due to cloud particles is largest for those clouds with a wide particle size distribution, because of the sheer number of large particles. However, Evans and Stephens (1995) found that increasing the mean particle size of the distribution has a similar impact on the radiance as the overall width of the distribution. Thus a wider distribution behaves as if it were a narrow distribution with a slightly larger mean particle size. This suggests that from a radiative transfer point of view it is difficult to distinguish between the signal coming from the characteristic size and the signal coming from the width of the distribution. In either case the impact on the measured radiances is too large to be ignored without impacting the overall retrieval performance. Therefore we have chosen to retrieve the median diameter of the particle size distribution (Dme) as part of our physical retrieval. Because coincident measurements of Dme and IWP are a useful quantity for various cloud modeling applications, the value of the retrieved Dme will be reported even though it is not one of the EDR requirements. For example, an important component of the parameterization of cloud microphysics in general circulation models is the ice particle size, since this determines the cloud radiative properties (Evans, 2000).

3.1.2.2 On the Retrieval of the Cirrus Cloud Top and Thickness

The main physical mechanism is absorption by the water vapor column above the cloud. For thin and moderately thick cirrus clouds the cloud top and cloud thickness may be adjusted in the retrieval to produce radiometrically equivalent results. That is, by varying the altitude of the cloud top while fixing the cloud thickness to an arbitrary value it is always possible to find an effective cloud top which produces the same radiances as the true combination of cloud top and cloud thickness. However, for thick clouds (i.e., greater than about 200 mb) the algorithm will not converge properly as it will be unable to find an appropriate cloud top.

Operationally the algorithm performs the retrieval of both the cloud top and the cloud thickness. If the cloud top is known from an external source (e.g., CrIS or VIIRS) then the retrieval of cloud thickness is possible even for medium and thin cirrus cloud types.

3.1.2.3 Physical Constraints

Currently, the algorithm uses no statistical relationship between IWP and Dme. The plan is to derive such relationships from climatological information or based on environmental conditions obtained from special experiments such as CEPEX and FIRE.

3.1.3. Algorithm Processing Outline

The core inversion algorithm is described in the Core Physical Inversion Module ATBD. The state vector is extended to include the ice water path, median diameter of the particle size distribution, and cirrus cloud top and thickness.

3.1.4. Forward Model in the Presence of Scattering

The forward model in scattering media is described in Conical-scanning Microwave Imager Sounder Environmental Data Records ATBD Volume 2, Core Physical Inversion Module. It uses delta Eddington 2nd approximation radiative transfer (Evans, 1997). The frequencies strictly below 89 GHz are currently assumed to be unaffected by the presence of ice in order to meet the processing time constraints in operational mode. However, the frequencies below 89 GHz should be minimally affected by scattering under the cirrus cloud conditions in non-precipitating cases. Alternate approaches have been developed and evaluated for IWP retrieval under precipitating clouds.

3.1.5. Ice Water Path Algorithm Performance (Non-Precipitating Clouds)

We present in this section the performances of the IWP physical retrieval algorithm. First we describe the test dataset that was used. The brightness temperatures are then computed and footprint matched before to perform the retrieval. The noise affecting the brightness temperatures corresponds to a spatial horizontal resolution of 50 kilometers.

3.1.5.1 Description of Test Data

The set of environmental conditions used to simulate the IWP algorithm performance has been designed to account for the variation of each of the parameters impacting the retrieval. The core of this data consists of 200 atmospheric temperature and water vapor profiles and surface temperatures randomly selected from the global NOAA-88 data set. The range of other cloud and surface parameters is given in Table 11. The ocean emissivity is calculated using the Wilheit model (1979) with variable wind speed, while the land surface emissivity is obtained (randomly) from the Prigent database (Prigent et al., 1997; Prigent, Personal Communication, 2000). To account for the vertical inhomogeneity of the cirrus cloud parameters, it is first assumed that the Dme and IWP decrease linearly with height beginning with a random value at

the cloud base. The slope of the Dme decrease is determined by a random number between 0.5 and 1.0, where 1.0 represents a homogeneous cloud. The IWP is related to the Dme by an exponential function. The exponent is random between 0 (IWP homogeneous) and 4. The particle sizes are given by a gamma distribution (Evans et al., 1998). All the simulations assume a spherical shape for the hydrometeors.

Table 11: Surface and cloud parameters used in verification of the IWP algorithm performance.

Parameter	Range
Ocean Wind Speed	0 – 20 m/s
Land Emissivity	Prigent Database
Cirrus Cloud Top	300 mb, 500 mb
Cloud Thickness	30 – 170 mb
Ice Water Path	0 – 1000 g/m ²
Dme	50 – 800 μm
Gamma Distribution Factor	$\alpha = 1 - 7$

Additional assumptions used during the performance assessment include (1) both simulation and retrieval use optical properties for spheres and (2) there is no cloud liquid water present. Impact of shape is described in a later section. Using all of the combinations of profiles, cloud, and surface parameters gives a total test set of 20,000 points.

3.1.5.2 Evaluation and Analysis of Results

This section describes the performance of the physical retrieval of cloud ice water path (IWP). These simulations were done using single scattering coefficients of spheres, computed using Mie theory. In addition to IWP and Dme, the cloud top pressure and the cloud thickness were also retrieved. However, the retrieval simulations presented below did not account for different types of vertical inhomogeneity or different particle size distribution widths (alpha in Table 11). Further the instrumental error covariance matrix was relaxed to avoid issues related to an attempt by the algorithm to over-fit the retrieval, especially for high cloud tops and at high frequencies where the sensitivity is larger.

The retrieval results discussed below (Figure 13 - Figure 16) represent the accuracy and precision of the retrieval in a 3-dimensional space for a range of IWP between 0 and 1000 g/m² and a range of Dme between 50 and 900 μm. Several algorithm and sensor configurations have been tested. These represent different approaches to understanding the optimal method and sensor channel set for performing the IWP retrieval. The results are shown for ocean scenes. However, the retrieval performance over land is consistent with the ocean cases and is discussed at the end of this section.

In addition to the CMIS baseline configuration (which contains channels with frequencies up to 183 GHz), retrieval simulations were performed to consider the addition of sub-millimeter sounding channels. Several different channel configurations were tested, including 220, 325 and 340 GHz, to determine which would provide the most useful information to the IWP retrieval. The best results were obtained for channels located around the water vapor absorption line at 325 GHz, which will be referred to as the “CMIS+325” channel configuration (see Table 12 for the exact channels frequencies).

Table 12: Description of the sub millimeter channels tested in the “CMIS+325” configuration. The three channels are centered around the 325 water vapor absorption line and are all mono-sided.

Central Frequency	Side 1	Side2	Half-bandwidth
325.15000	1.5000	0.0000	500
325.15000	3.1800	0.0000	500
325.15000	5.9400	0.0000	500

Overall the retrieval results are consistent with the published simulation results (e.g., Deeter and Evans, 1999; Liu and Curry, 2000). For Dme below 200 μm the performances are generally degraded, even considering higher frequency channels around the 325 GHz water vapor absorption line. This degradation is due to the lack of sensitivity for the range of particle sizes in the spectrum considered. Low Dme values will not be considered in the calculation of the performances for the error budget.

Prior knowledge of the cloud top pressure (e.g., from a VIIRS measurement) provides additional information to the IWP retrieval. By constraining the cloud top to the true value, the algorithm is able to distinguish between the radiometric signature of the cloud top, the Dme and the IWP. But, as discussed in Section 3.1.2.2, the cloud top and cloud thickness can be varied to produce different clouds which are radiometrically equivalent. Consequently, the retrieval will be stabilized if only one of the two parameters is retrieved. If the cloud top pressure is unknown from external data, the cloud thickness can be fixed to a constant value for the retrieval of cloud top pressure. Similarly, if cloud top information is available, then the cloud thickness may be retrieved. Simulation studies have shown that even if the cloud top information is available, it is best to let it vary slightly in order to compensate for the vertical inhomogeneities of the cloud parameters. The simulations have been performed for both known and unknown cloud top. Unless otherwise noted, the cloud is located at 300 mb for all of the simulations presented here.

Figure 13 and Figure 14 show the impact to the retrieval of the addition of the 325 GHz channels when the cloud top pressure is known, while Figure 15 and Figure 16 correspond to an unknown cloud top. These figures show that the addition of sounding channels at 325 GHz provides sufficient information for improvement in the IWP retrieval. These comparisons also show a slight improvement in both accuracy and precision for the case where the cloud top pressure is known.

Figure 17 illustrates how clouds located at different altitudes will change the previous retrieval results. This figure was generated by considering the largest errors for the range of IWP and Dme for each of the different cloud top pressures. The retrievals shown in Figure 17 were performed for the CMIS baseline channel set with the addition of the 325 GHz channels. Note that these performances considered only Dme values greater than 200 μm . Other simulations (not shown) illustrate that the addition of *a priori* knowledge about the cloud top pressure results in little change in the retrieval performance.

The IWP retrieval performance over land (Figure 18 –18) is generally worse than the performance over ocean backgrounds (see Figure 13 – Figure 16). The same conclusions drawn previously concerning the addition of the 325 GHz channels and the *a priori* knowledge of the cloud top hold true for IWP retrieval over land for high altitude cirrus clouds. For low clouds, where the surface background does not offer much contrast with the atmosphere, the IWP performances are degraded compared to high.

Another point to consider is that in the current implementation of the algorithm, the IWP variation is not constrained to the Dme or the atmospheric temperature. It is expected that these types of constraints will further improve the retrieval of the IWP by separating the radiometric signatures of the IWP and the Dme. The values of these constraints could be obtained from a robust set of measurements, such as those obtained during the CEPEX campaign (McFarquhar and Heymsfield 1997). Because this information is not a part of the current algorithm, the performance estimates shown here represent accuracy and precision values that are a somewhat larger than might be achieved if this information were available.

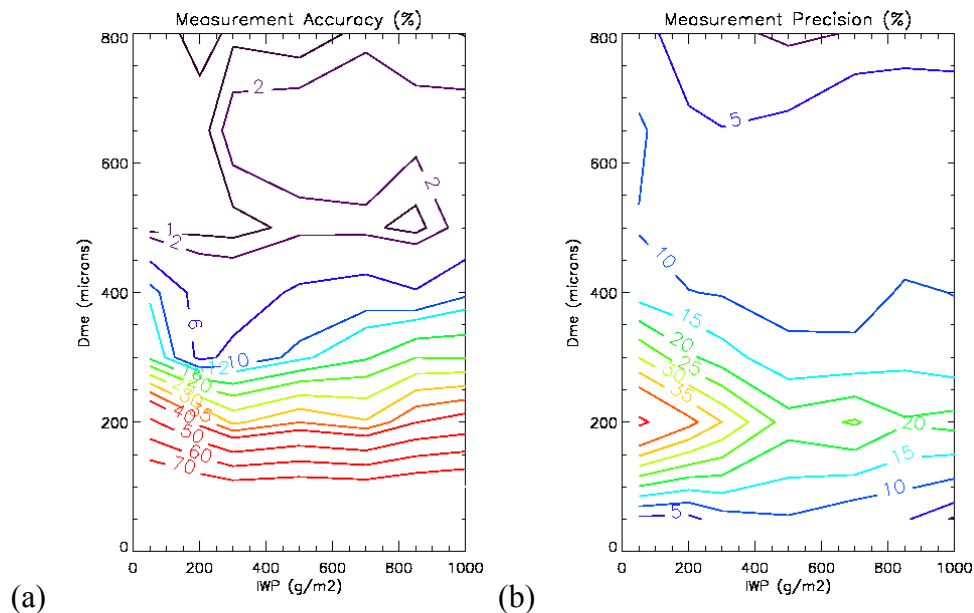


Figure 13: Retrieval (a) accuracy and (b) precision for 300 mb cloud over ocean with CMIS+325 channel set and known cloud top pressure.

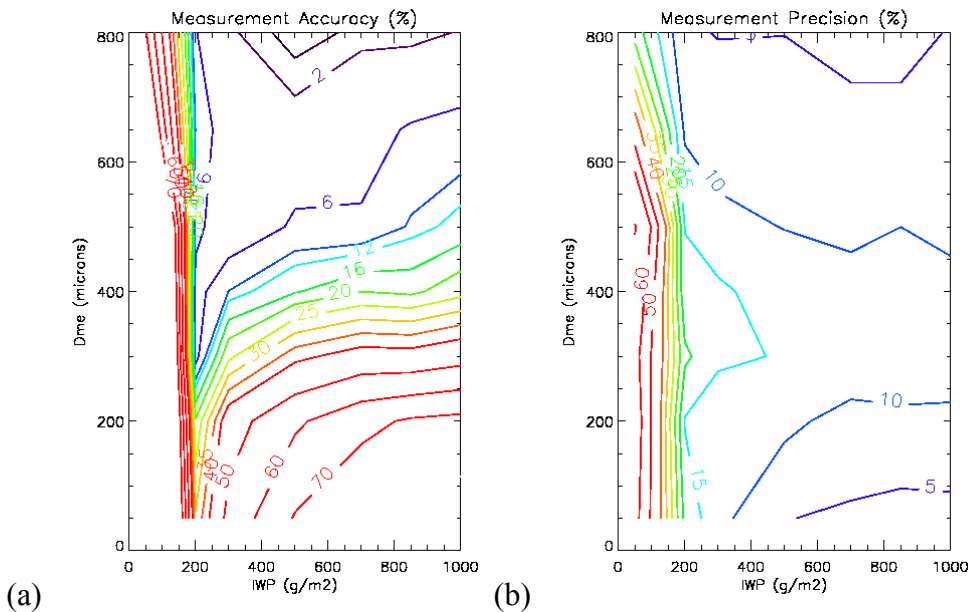


Figure 14: Retrieval (a) accuracy and (b) precision for 300 mb cloud over ocean with CMIS channel set and known cloud top pressure.

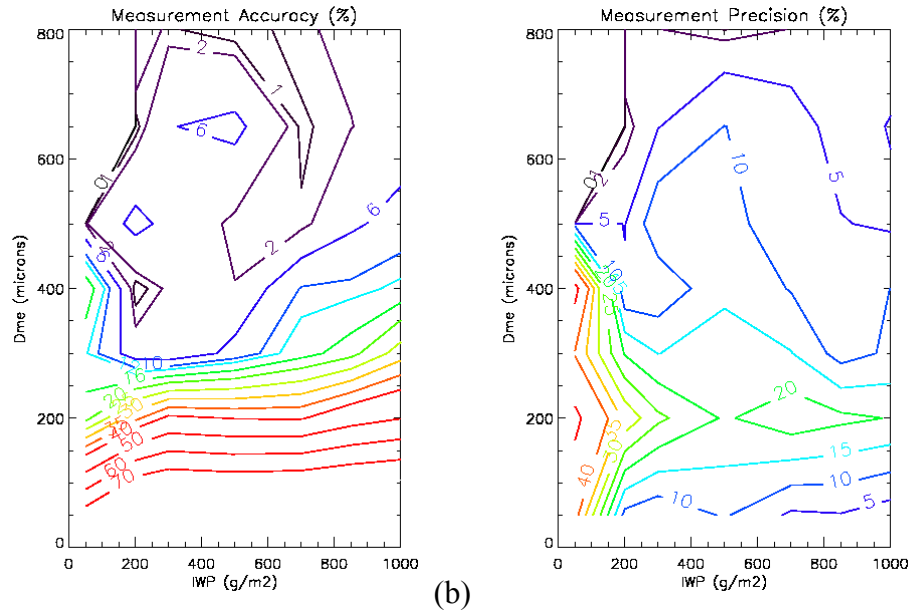


Figure 15: Retrieval (a) accuracy and (b) precision for 300 mb cloud over ocean with CMIS+325 channel set and unknown cloud top pressure.

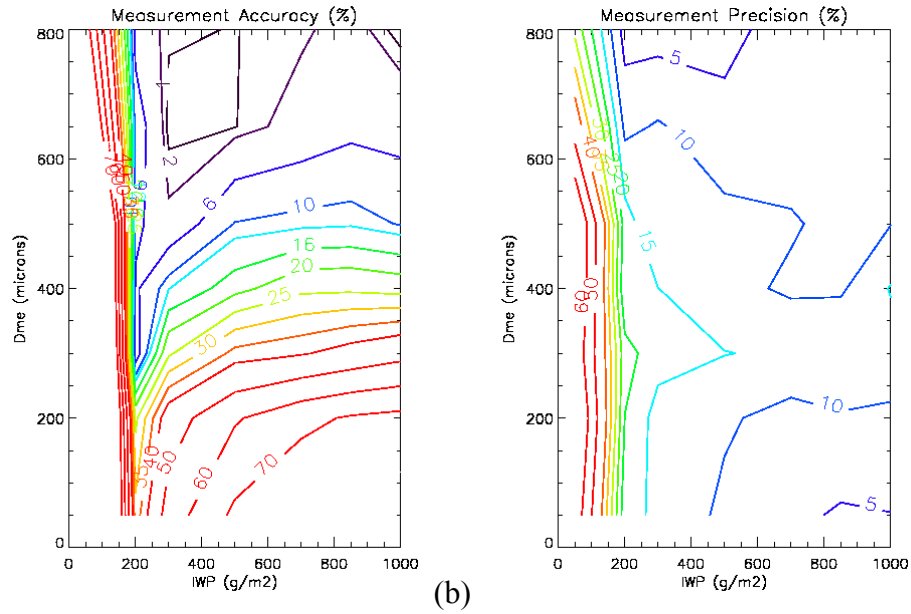


Figure 16: Retrieval (a) accuracy and (b) precision for 300 mb cloud over ocean with CMIS channel set and unknown cloud top pressure.

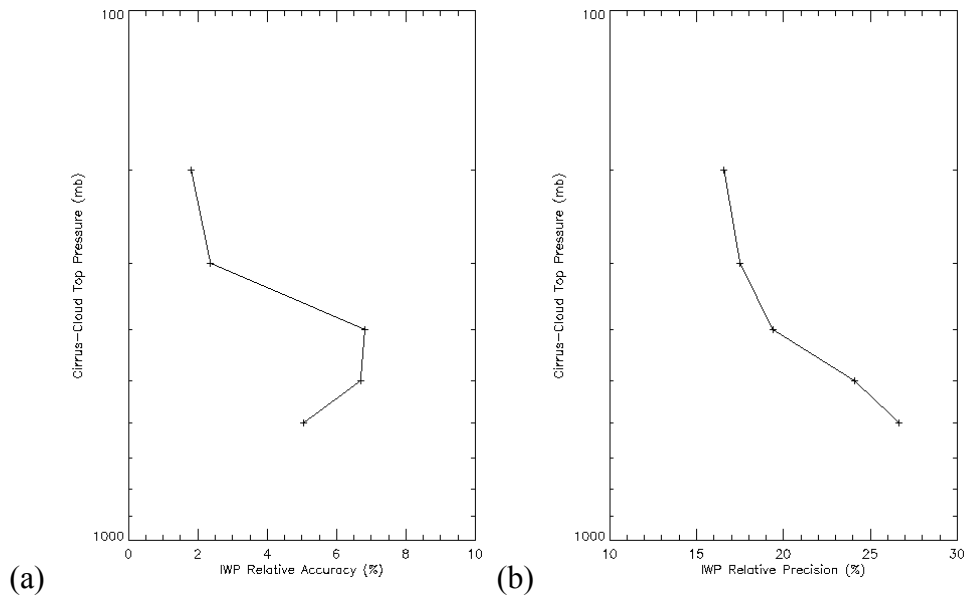


Figure 17: Retrieval (a) accuracy and (b) precision for CMIS channel configuration and known cloud top pressure.

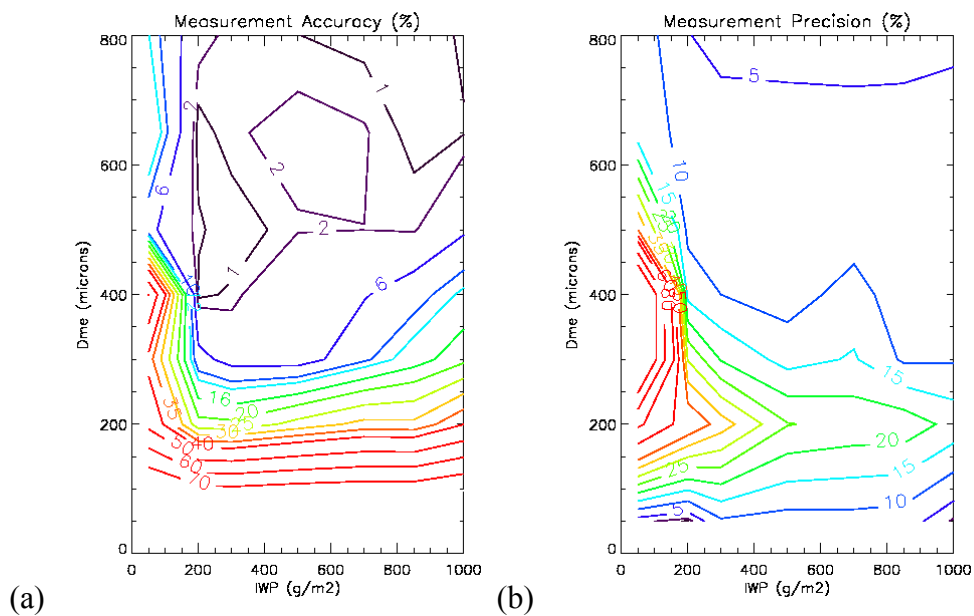


Figure 18: Retrieval (a) accuracy and (b) precision for 300 mb cloud over land with CMIS+325 channel set and known cloud top pressure.

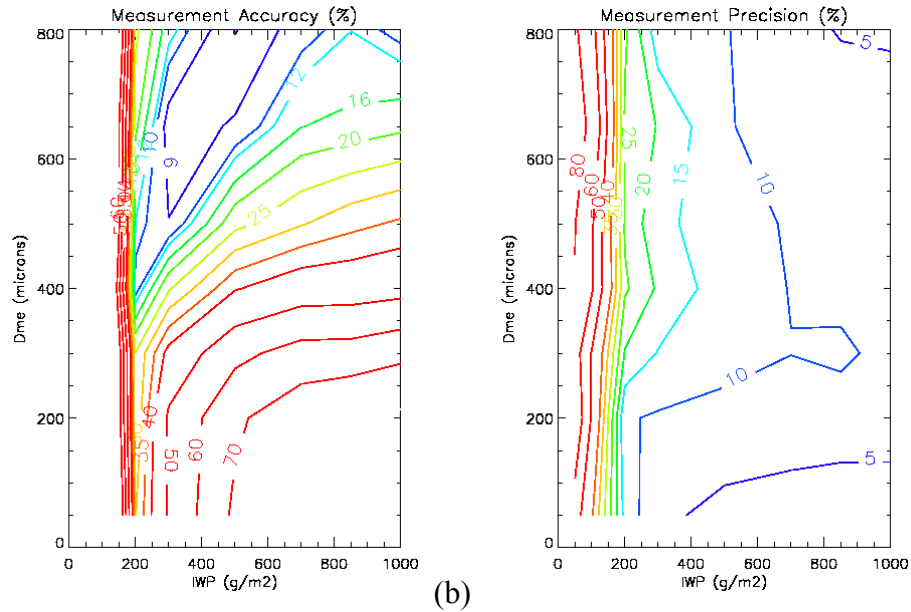


Figure 19: Retrieval (a) accuracy and (b) precision for 300 mb cloud over land with CMIS channel set and known cloud top pressure.

3.1.5.3 Discussion about the Dme measurement range :

The requirements regarding the ice water path are specified regardless of the range of the median diameter Dme. However, the CMIS frequencies are not radiometrically sensitive to the low end of the Dme range: below 400 microns. This cutoff is pushed to 200 microns if we use the submillimeter radiances (see previous contour plots and Figure 20). When computing the performances, we can include the whole Dme range, in which case the diameters to which we are not sensitive will negatively impact the overall performance. The other option adopted here is to exclude the Dmes to which we have no retrieval skills (radiometrically speaking) and report performances only for the range of Dme where we have reasonable skills. Figure 20 shows the retrieval performance for one case where the true ice water path was 300 g/m². We have little skills for the low diameters (below 400 microns). If we add higher frequencies (325 GHz for instance), it allows us to report performances for a broader range of Dme (above 200 microns). The use of the IR radiances would allow us to further extend the Dme range in the report of the performances below 200 microns, see section 4 on the IR algorithm performances.

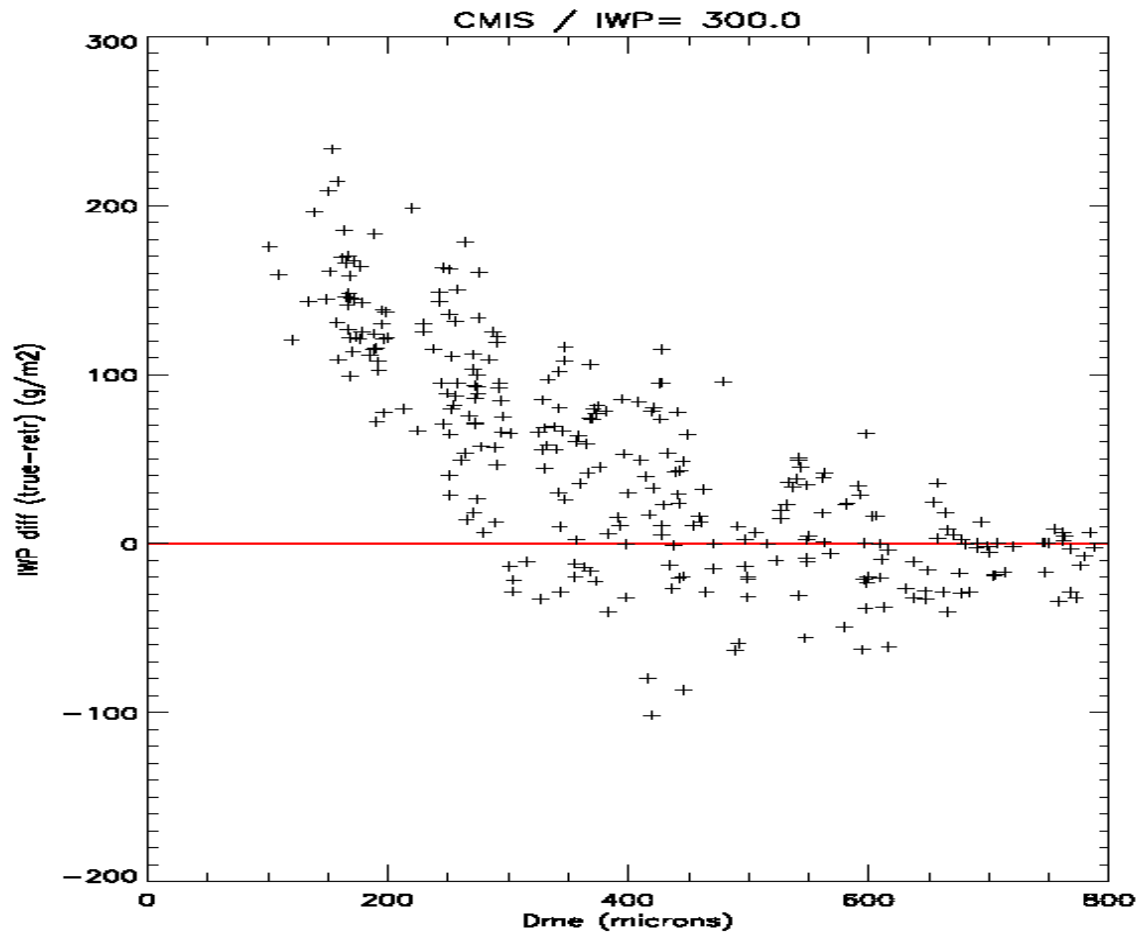


Figure 20: IWP retrieval performances as a function of median diameter (D_{me}) (IWP 300 g/m^2). Cloud Top is assumed known (300 mb). Little retrieval skill for D_{me} below 400 μm

3.1.5.4 Overall IWP Retrieval Error Budget for non-precipitating IWP

The elements of the IWP error budget are summarized in Table 10. The error budget due to the sensor noise and to the environmental conditions was generated by simulation.

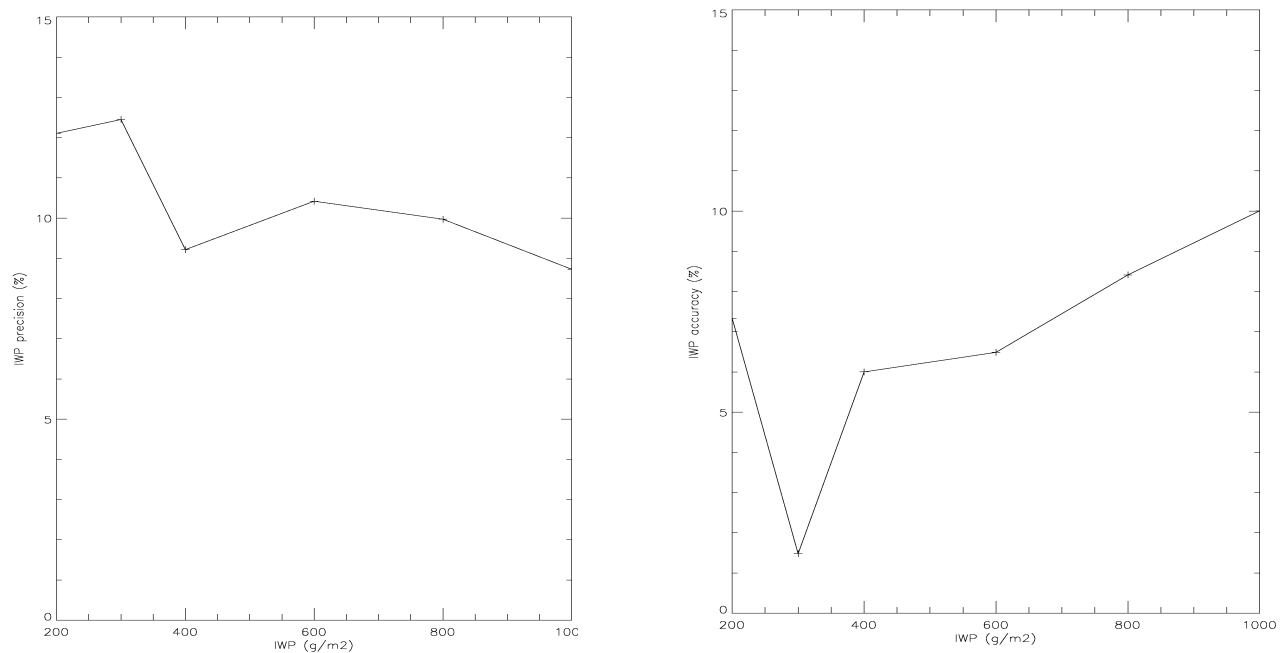


Figure 21: Precision (left) and Accuracy (right) of the Ice Water Path Retrieval for the CMIS configuration. The cirrus cloud top is 300 mb in this case and is supposed known from an external source. Only Dmes above 400 microns were considered for the computation of these statistics. For the error budget, the worst case in the IWP range was picked. Case over ocean.

Only Dme values with sensitivity were considered. This corresponds to 400 μm for the CMIS baseline (with channels up to 183 GHz). The error budget was determined for different cloud top pressures for land and ocean scenes. These calculations were done for cloud top pressures of 300 mb and 500 mb. The precision is the square-root of the weighted sum of the squares of the individual precision values. From this an overall land/ocean error budget was derived. The global error budget is the simple weighted mean determined from the land and ocean cases weighted relative to their frequency of occurrence. The error due to cell mismatch was deduced by comparing the sensor response function for a square field-of-view (FOV) with a Gaussian FOV. This comparison was done for highly convective scenes. However, the error for cirrus cloud types is about 50% of that of the convective scenes. The precision and accuracy of the cell mismatch were estimated to be around 6%.

Impact of Bimodal Distribution:

Ice mass in the cirrus cloud has contributions from both the small and large modes (Mitchell, 2000): $IWP = IWP_{sm} + IWP_l$.

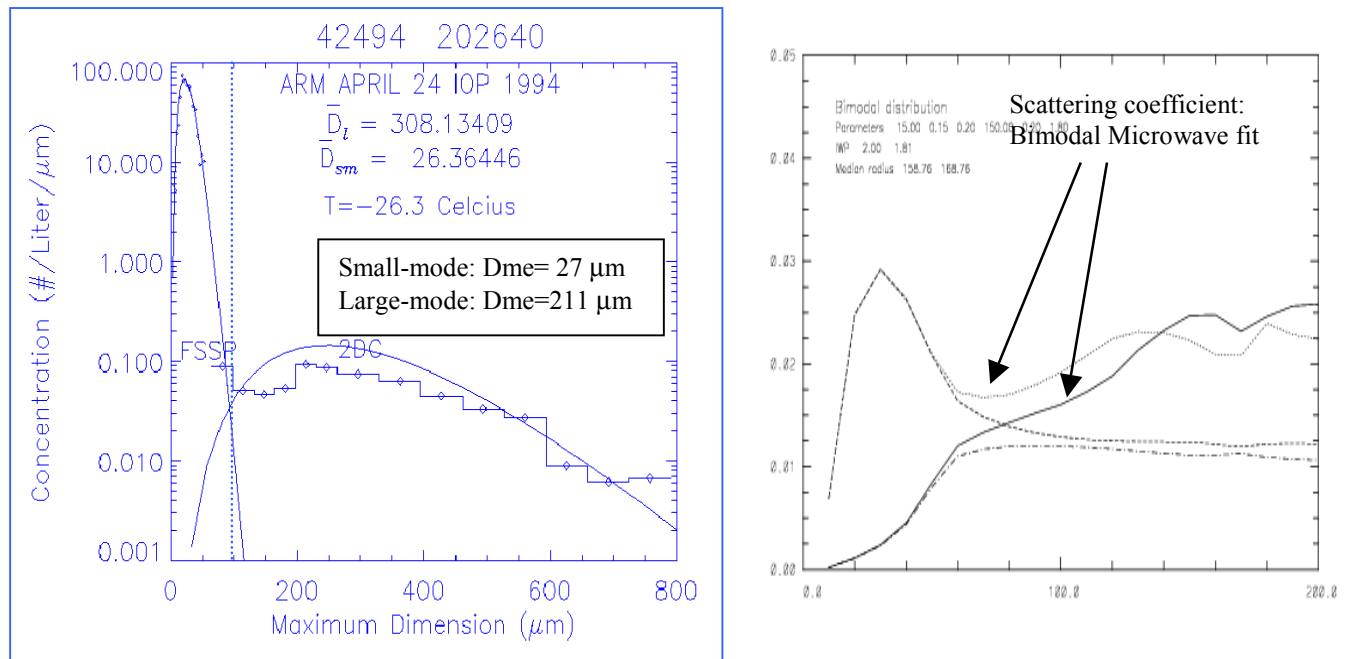


Figure 22: Bimodal Distribution and its impact on the scattering coefficient.

The retrieval only fits the contribution of the large mode in the microwave and sub-millimeter regions: $IWP_{retr} \approx IWP_l$.

Therefore, information about IWP_{sm} must be derived from an external source (e.g. environmental conditions). Analysis of ARM IOP data indicates that IWP_{sm} / IWP is relatively invariant with temperature in midlatitude cirrus. Fixed bias correction could reduce error to about 5 % in the midlatitudes. In the tropics, it is found that there is a strong temperature dependence for diameters below 200 microns (see Figure 23). See section 2.3.2.1 on the discussion about the bimodal distribution.

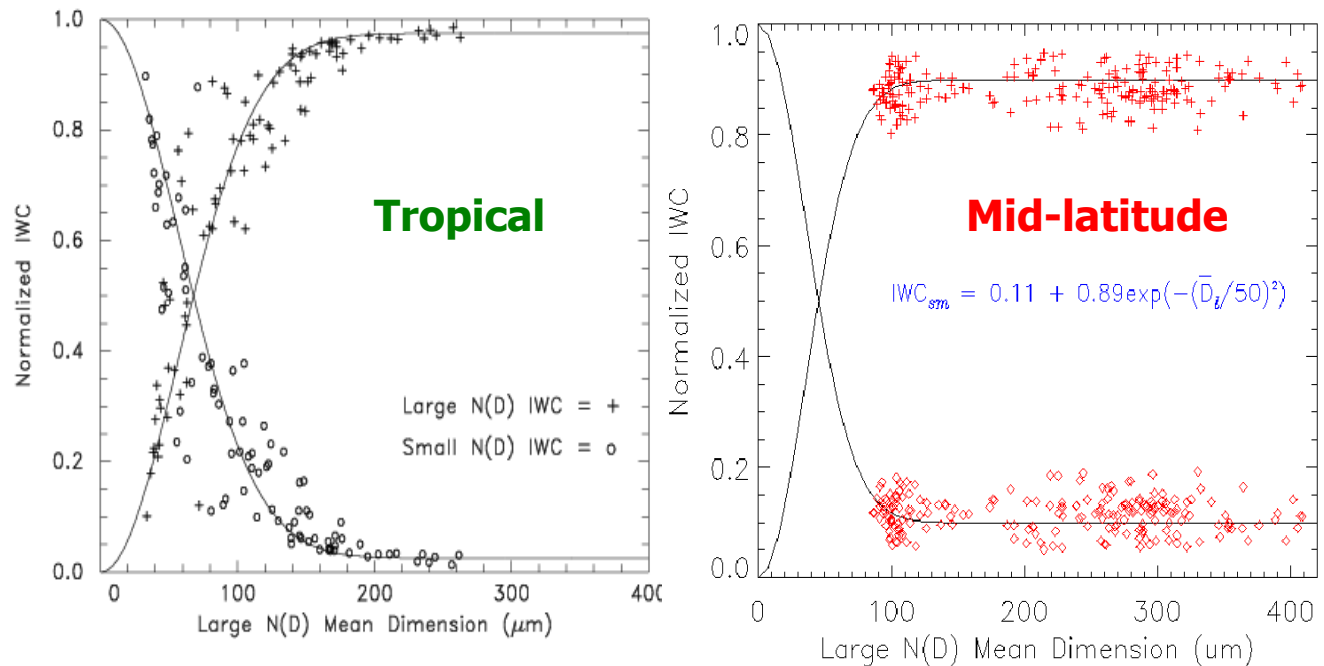


Figure 23: Distribution of the Ice water content for the two modes (small and large) for both tropics and mid-latitudes.

Impact of crystal shape:

Crystal shape error was determined from a study by Evans (Evans et al., 2001). This uncertainty was quantified by simulating observations from clouds containing four different randomly oriented particle shapes: hexagonal column, 4 bullet-rosette, 7 bullet-rosette and a stick-ball irregular shape. Observations were simulated for two cases: 1) each cirrus cloud made of a single, randomly chosen particle shape, and 2) all clouds made of an equal mixture of the four shapes. The retrievals are performed with a database made for the equal mixture of shapes. Thus, the retrieval accuracy for the first case contains the particle shape effect, while that for the second case does not. The authors found that the errors become noticeable for IWP greater than 30 g/m^2 but it remains small. It was found that the error due to crystal shape increased with IWP because large IWP is associated with larger particle sizes which have greater particle shape difference. The maximum rms error due to particle shape was found to be around 10% for the IWP range between 200 and 800 g/m^2 . The previous experiment may have underestimated the particle shape effect as pointed out by the authors because the retrieval is made with the mean mixture of the particle shapes which could be biased with respect to realistic particle shapes mixtures. On the other hand, the wide range of morphologies modeled is closer to the real cirrus mixtures than is the single shape assumed in this experiment.

Future experiments aimed at the cirrus cloud parameters measurement will give us a better knowledge of the global statistics. We will then be able to assess more accurately the mixture of particle shape that occurs in nature and thus minimize the error accuracy (bias).

3.2. Precipitating Clouds

The switch between non-precipitating and precipitating clouds is described in the “Overview: Integration ATBD (Volume I, Part I)”. The retrieval is part of the precipitating module.

3.2.1. Microwave Retrieval Approach (Precipitating Clouds)

For the precipitating cloud algorithm (for both land and ocean scenes), a statistical algorithm is trained on radiative transfer simulations for a variety of rain cloud properties and surface types. Because of the many degrees of variability in rain cloud scenes, as well as the potential non-linearity associated with the use of surface-blind sounding channels, a neural network approach is adopted:

$$R = f(\Delta\vec{T}_B)$$

where $f(\)$ represents the trained network and $\Delta\vec{T}_B$ is a vector of multi-channel brightness temperature anomalies relative to the precipitation-free background emission, as estimated by the CMIS Core module.

3.2.2. Description of Test Data

The particle size distribution (PSD) is driven by the Sekhon-Srivastava function, which depends only on the rate of precipitation. The simulation and training set comprises a randomly generated hydrometeor profile set (Kummerow, 1994). Simulations include instrumental noise, surface and atmospheric variability. The cloud ice water path is allowed to vary in a range from 1 – 12 kg/m², with the rain rate between 0 and 15 mm/hour. The vertical distribution of the hydrometeor data is shown in Figure 24.

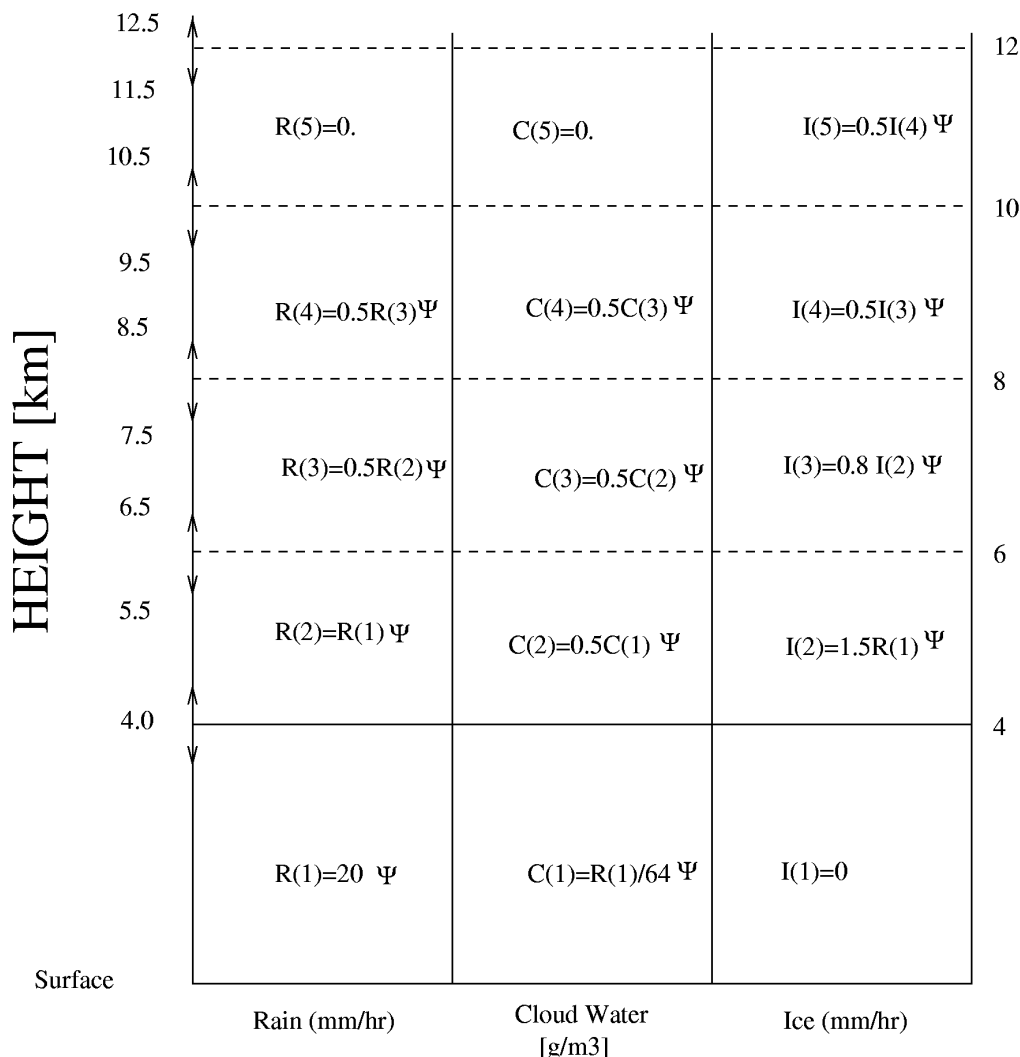


Figure 24: Schematic diagram showing vertical distribution of cloud constituents used for the generation of hydrometeor profiles (Kummerow and Giglio, 1994). The rain-rate (R) is selected randomly within a predetermined range using a random number (Ψ) between 0 and 1. For the case shown here, the RR falls in the range from 0-20.

3.2.3. Forward Model in the Presence of Precipitation

The general radiative transfer approach, and the OSS implementation, are described in detail in the Core Module ATBD. The tests described here use a specialized version of OSS, called OSSCAT. Since this is a non-polarized radiative transfer code, no explicit distinction is made between the horizontal and the vertical polarizations. OSSCAT is a combination of OSS and an extension of the CHARTS model (Code for High-resolution Accelerated Radiative Transfer with Scattering) to the microwave and sub-millimeter region (Moncet and Clough 1997). CHARTS is based on the adding-doubling method, with a specified number of discrete angles for the radiance computation. The individual electromagnetic efficiencies are computed off-line, using the Mie code, and the integration over the particle size distribution can be done outside or inside the forward model. The particle size distribution of the liquid rain follows Marshall and Palmer (1948). The frozen rain particle size distribution follows Sekhon and Srivastava (1970). The non-precipitating cloud liquid water particle size distribution is assumed to follow a gamma function.

3.2.4. Ice Water Path Algorithm Performance in the Presence of Precipitation

Determination of the IWP performance in the presence of precipitation was conducted using a data set similar to that described in Section 3.1.5.1. Figure 25 – Figure 28 illustrate the expected performance for ocean and land scenes. Performances have been calculated for two ranges of IWP: 1 – 2.6 kg/m² and 1 – 10 kg/m². These are denoted as the “threshold” and “objective” algorithm performances (see Table 1: Ice Water Path Measurement Requirements.). Note that IWP values less than 1 kg/m² will be retrieved using the physical algorithm described in Section 3.1.2. All of these simulations used the CMIS baseline channel set (see Section 3.1.5.2).

Differences between the threshold and objective performances, for either land or ocean conditions, are due to the training method of the neural-net retrieval algorithm. For the case of threshold performance, the neural-net was trained using only IWP values in the threshold range of retrieval, while for the objective case the training occurred with profiles spanning the entire range of IWP values.

The performance for ocean scenes over both the threshold and objective range of IWP values meets the objective accuracy requirements for most conditions. The precision values meet the threshold precision requirements. For both ranges of IWP the performance is degraded at low IWP values. The performance results for land scenes are consistent with those over ocean.

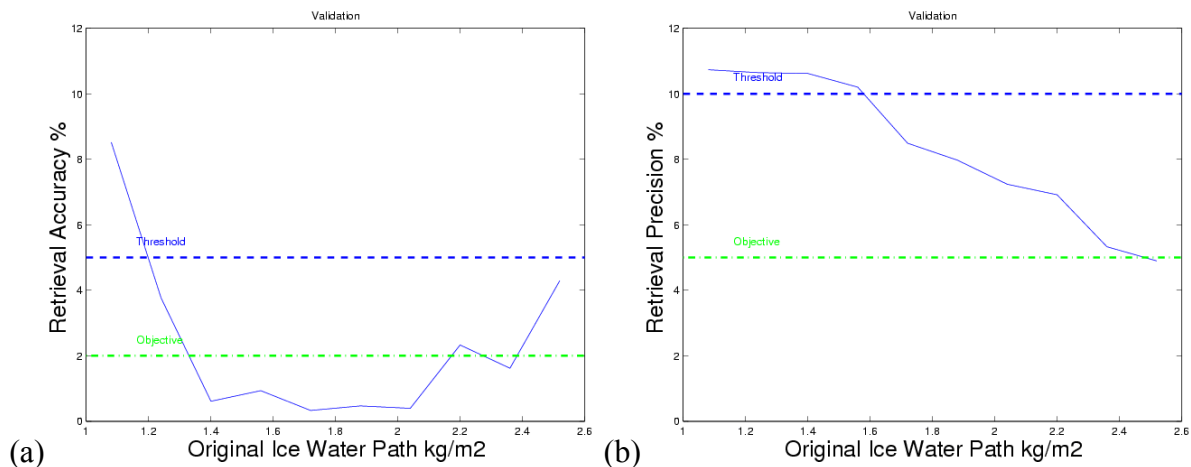


Figure 25: Ocean retrieval (a) accuracy and (b) precision for threshold range of IWP.

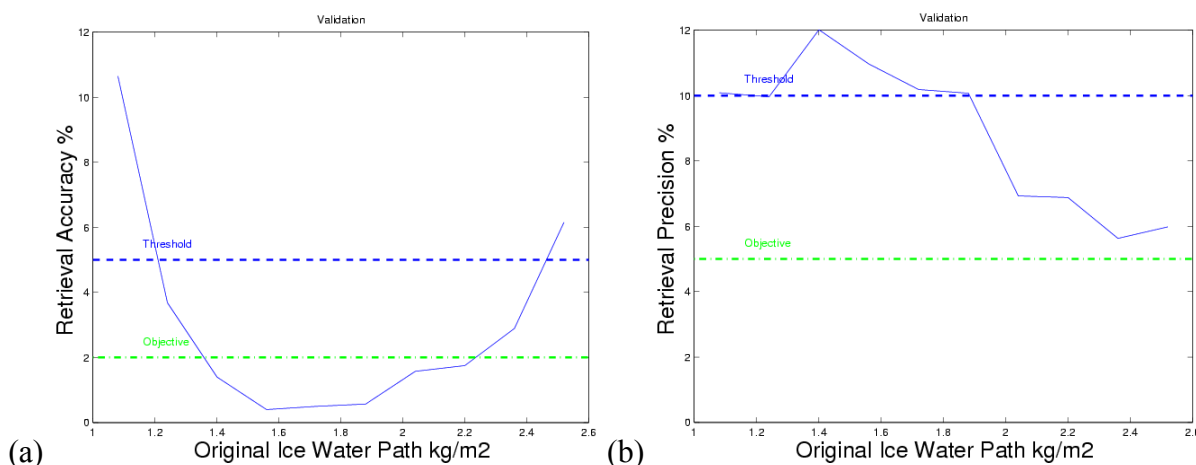


Figure 26: Land retrieval (a) accuracy and (b) precision for threshold range of IWP.

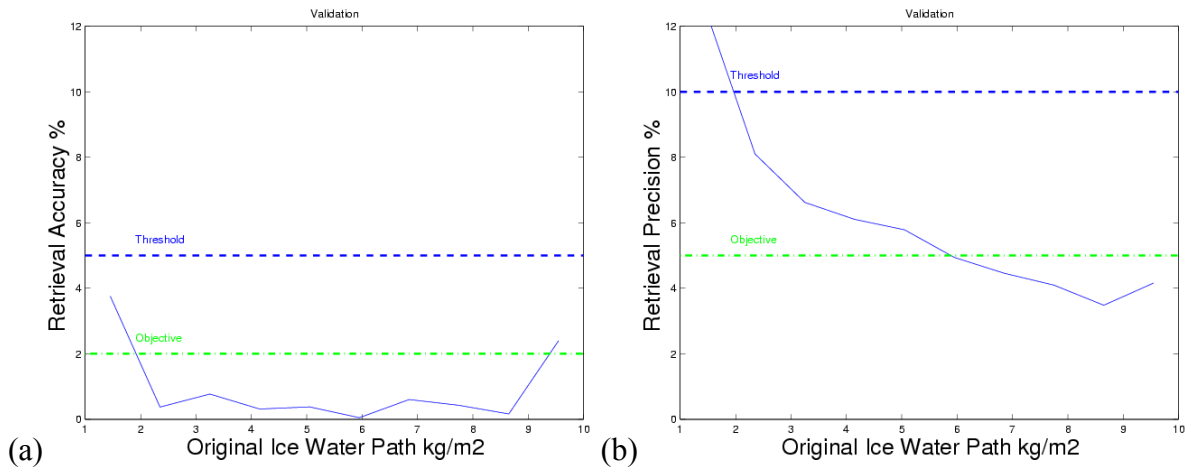


Figure 27: Ocean retrieval (a) accuracy and (b) precision for objective range of IWP.

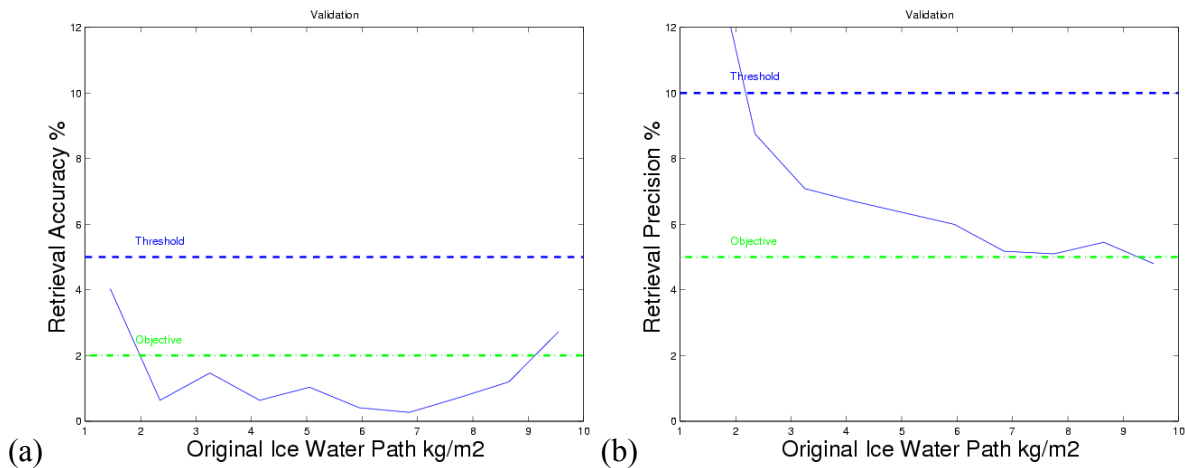


Figure 28: Land retrieval (a) accuracy and (b) precision for objective range of IWP.

3.3. Microwave Algorithm Performance Summary

Simulations of IWP retrievals considered instrumental noise, atmospheric variability, vertical inhomogeneities in ice concentration and particle size, and variability in the size distribution. With the baseline sensor configuration the algorithm is limited to $D_{me} > 400 \mu\text{m}$. For IWP in the range of $0.3 - 2.6 \text{ kg/m}^2$, the error is less than 20%. These values of IWP encompass frontal clouds, altostratus, and precipitating clouds. Large uncertainties exist in both the microphysics and radiative properties of the precipitating clouds. Final performance estimates include margin for uncertainties in cloud microphysics (characteristic crystal shape/density and size distribution) and 3-dimensional effects (which are significant for precipitating clouds). The final performance estimates include a bias reduction from improved microphysics characterization due to on-going and future *in situ* measurement campaigns.

4. Infrared Algorithm Description and Performance

An IR-based IWP algorithm was developed to sense the low size ice particles. This would be useful in combination with the sub-millimeter frequencies. The set of CMIS channels + the submillimeter channels + the IR radiances can have the capability of sensing all the ice particle sizes and will therefore cover all the range of ice water path.

Using the IR radiances, cirrus ice-water path (IWP) is estimated using a coupled algorithm that simultaneously retrieves IWP, ice-crystal particle size, emissivity, and cirrus temperature using radiances collected in the GOES mid-wave infrared (MWIR) and thermal infrared (TIR) wavelengths, nominally at 3.9 and 10.8 μm . From a radiative transfer point of view cirrus IWP, emissivity, effective particle size, and effective temperature (defined here as the temperature of the radiative “center of mass” of the cirrus cloud) are interdependent. For this reason all these cloud attributes are being estimated simultaneously using a first-principles algorithm that numerically solves a set of simultaneous radiance equations.

The cirrus retrieval algorithm uses a simultaneous-solution approach to ensure physical consistency between satellite radiance measurements and theoretical radiative transfer calculations. The fundamental non-uniqueness of the relationship between measured radiance and cloud IWP, emissivity, particle size, and temperature at a single wavelength is resolved by forcing the retrieved parameters to be simultaneously consistent with theory and satellite observations at multiple infrared wavelengths.

4.1. Cirrus Attributes

This section summarizes all the cirrus attributes that are retrieved using our IWP algorithm. For emissivity, particle size, and cirrus effective temperature our approach is to retrieve these parameters simultaneously, since from a radiative point of view they are not independent of one another. Our radiative-transfer theory also requires as a by-product the specification of other cirrus microphysical and radiative attributes such as ice-water path and optical thickness.

Cirrus effective particle size D_{eff} (usually expressed in μm) is defined as the ratio of the third moment of the ice-crystal size distribution to the second moment, averaged over a layer of air within a cloud. A second particle-size metric, the sphere-equivalent mass-median diameter D_{me} (μm), is defined as the crystal dimension that divides the cirrus ice-crystal size distribution into two equal-mass portions. In other words, the mass of the entirety of ice crystals whose diameter is greater than the mass-median diameter is equal to the mass of all crystals whose size is less than the median diameter. Cirrus optical thickness is the extinction (scattering plus absorption) vertical optical thickness of the cloud. Optical thickness τ is related to the transmittance t by the relation

$$t = e^{-\tau}.$$

Effective cloud-top temperature T_{cld} (K) (height z_{cld} (m), pressure p_{cld} (mb)) is valid for the radiative center of mass of the cirrus cloud, “effectively” placing it as an infinitesimally thin slab of ice crystals of size D_{eff} at a single atmospheric level z_{cld} . Thus the retrieved temperature (height, pressure) is that which, in combination with the retrieved emissivity, yields the same upwelling radiance for a cirrus cloud that is homogeneous in D_{eff} as does the actual cirrus cloud that is heterogeneous in D_{eff} .

Cirrus ice-water path is defined as the vertical summation of the mass of all ice crystals in the cirrus cloud per unit area, and typically has units of g/m^2 .

4.2. Infrared Algorithm Description

This section describes the scientific basis of the cirrus IWP retrieval algorithm. Our approach is to retrieve the parameters IWP, particle size, emissivity, and cirrus effective temperature simultaneously, since from a radiative point of view they are co-dependent on one another. Cloud effective temperature can be thought of as the temperature at the cloud's radiative "center of mass," and does not usually correspond to the physical top of the cirrus cloud unless it is optically very thick. However the retrieved cloud effective temperature is a marked improvement over temperatures that are computed using a blackbody assumption, especially for transmissive cirrus.

4.2.1. The Cloud Retrieval Problem

Clouds exist globally throughout the troposphere. Their effects on remotely sensed top-of-atmosphere (TOA) radiances emitted at thermal infrared wavelengths are highly variable both temporally and spatially.

Scattering of light by spherical water droplets is largely a solved problem. Given a spherical particle of radius r and complex refractive index $n = n_{\text{re}} + in_{\text{im}}$, Mie theory provides the means for computing the extinction efficiency factor Q_{ext} , the scattering efficiency Q_{sca} , and the phase function $P(\Theta)$ for a given scattering angle Θ . Other relevant properties, such as the single-scattering albedo ω and asymmetry parameter g , can be derived from the above quantities. All parameters derived from Mie calculations are wavelength-dependent.

Scattering by non-spherical ice crystals is substantively more problematic due to the non-uniform shape of the scatterer. While much progress has been made in this area, significant uncertainties remain, such as the phase function and its dependence on environmental conditions (e.g., crystal shape and its dependence on temperature and supersaturation).

The net radiative effects of an atmospheric cloud layer depend on its size distribution $n(r)$, which is the number of particles per unit volume per particle-size radius increment: common units for $n(r)$ are $\text{cm}^{-3} \mu\text{m}^{-1}$. Bulk radiative attributes of the entire cloud layer are computed as a frequency-of-occurrence weighted sum of the Mie-computed variables for a population of cloud particle radii. For example, the extinction coefficient β_{ext} for cloud layer is given by

$$\beta_{\text{ext}} = \int_0^{\infty} \pi r^2 Q_{\text{ext}}(r, \lambda, m) n(r) dr \quad (1)$$

The radiative effects of a cloud layer depend strongly on its particle size distribution. Many size-distribution shapes are used in radiative transfer models for cloudy atmospheres, but the most common are a modified gamma distribution for spherical water droplets (e.g., Miles et al., 2000) and a uni- or bimodal gamma distribution for non-spherical ice crystals (e.g., Mitchell et al., 1996). Gamma distributions are reasonably consistent with in-situ observations of cloud particles, although variations on these shapes occur that are functions of cloud formation processes (e.g., convective or stratiform). The vertical distribution of ice-cloud particle sizes also tends to vary with temperature.

Knowledge of the cloud droplet (crystal) size distribution, refractive index, total liquid (ice) water path, and vertical distribution of mass within the cloud is required to properly parameterize radiative transfer models. Calculation of top-of-atmosphere radiances requires consideration of cloud scattering and absorption, multiple-scattering interactions between cloud particles and atmospheric gases, and absorption by atmospheric water vapor.

4.2.2. Ice Crystal Cloud Emissivity and Temperature

Analytic approximations to full geometric-scattering theory for non-spherical ice crystals have been developed for use in simulating mid-wave (MWIR) and thermal infrared (TIR) bands. This section describes the theory and summarizes its application in our retrieval paradigm.

The infrared upwelling radiance $I_{\lambda, \text{TOA}}$ at wavelength λ in a non-scattering atmosphere and for a cirrus-filled pixel is well approximated by

$$I_{\lambda, \text{TOA}} = (1 - \epsilon_{\lambda}) I_{\lambda, \text{clr}} + \epsilon_{\lambda} B_{\lambda}(T_{\text{cld}}), \quad (2)$$

where ϵ_{λ} is the cirrus emissivity at wavelength λ ; $I_{\lambda, \text{clr}}$ is the TOA radiance that would be observed in an otherwise cloud-free pixel; and $B_{\lambda}(T_{\text{cld}})$ is the cirrus Planck blackbody radiance, a function of the cirrus effective emitting temperature T_{cld} .

As an aside, the overall retrieval paradigm is to write Eq. (2) for two wavelengths and solve them simultaneously using an iterative numerical approach. At first glance, Eq. (2) has two unknowns in emissivity ϵ and cirrus temperature T_{cld} , making such a solution possible in a strictly mathematical sense. In practice, the improper choice of the two wavelengths can make the solution unstable and poorly defined. These issues are all discussed in later sections, but the overall approach is mentioned here to keep in mind as the theoretical discussion of our radiation transfer models continues.

Effective temperature is understood in its proper context via Eq. (2): T_{cld} is not the cloud-top temperature, but rather the temperature of the radiative “center of mass” of the cirrus cloud. This is evidenced by the fact that the second term on the right side of Eq. (2) represents the integration of layer radiances over the entire depth of the cirrus. Mathematically, ϵ_{λ} and T_{cld} are the values that make the expression

$$\epsilon_{\lambda} B_{\lambda}(T_{\text{cld}}) = \int_{t_{\text{base}}}^{t_{\text{top}}} B_{\lambda}[T_{\text{cld}}(t)] dt \quad (3)$$

true. In Eq. (3), “ t ” denotes the transmittance profile of the cirrus cloud, due only to the ice crystals. Atmospheric attenuation within and above the cirrus cloud is formally neglected in the formulation of Eq. (2), but in practice represents a source of error in T_{cld} . However, since water vapor is the primary and relatively weak atmospheric absorbing constituent in the MWIR and TIR window bands, its influence at and above cirrus levels on TOA radiances is minimal.

In general, cirrus effective temperature is not representative of the cirrus cloud top temperature. However, it helps diagnose the wavelength dependence of cirrus emissivity.

Equation (2) forms the basis for the radiative-transfer model in our cloud implementation. Neglecting cirrus reflectivity, absorption optical thickness τ_{abs} is related to cirrus emissivity ϵ via the expression

$$1 - \varepsilon = e^{-\tau}.$$

Thus Eq. (2) can be written

$$I_{\lambda, \text{TOA}} = \exp(-\tau_{\lambda, \text{abs}}) I_{\lambda, \text{clr}} + [1 - \exp(-\tau_{\lambda, \text{abs}})] B_{\lambda}(T_{\text{cld}}), \quad (4)$$

where $\tau_{\lambda, \text{abs}}$ is the cirrus bulk absorption optical thickness at wavelength λ . All that is needed to use Eq. (4) within our simultaneous-equation retrieval framework is a physically consistent model that relates cirrus optical thickness at multiple wavelengths to effective particle size and temperature. This need motivates the development of a scattering theory for non-spherical ice crystals that is outlined next.

4.2.3. Ice Crystal Effective Diameter

Cirrus ice-crystal effective diameter (D_{eff}) is an important cloud attribute in our retrieval approach, and is directly related to ice water content (IWC). First the definition of effective diameter with respect to irregularly shaped ice crystals is addressed.

The concept of an effective distance or photon path, d_e , as being a particle volume-to-area ratio was first suggested by Bryant and Latimer (1969) and further developed in Mitchell and Arnott (1994) and Mitchell et al. (1996) to treat absorption and extinction by ice particles. The last two citations define d_e for ice particles as the volume V (cm^3) defined at bulk ice density divided by the particle's projected area at random orientation, P (cm^2):

$$d_e = m / (\rho_i P), \quad (5)$$

where m is the particle's mass (g), and bulk ice density $\rho_i = 0.92 \text{ g cm}^{-3}$. This value of ρ_i must be used since ice refractive indices are referenced to bulk ice density. This concept of d_e is borne out of the anomalous diffraction approximation (ADA), a simplification of Mie theory (van de Hulst 1981). ADA approximates the absorption efficiency as

$$Q_{\text{abs,ADA}} = 1 - \exp(-4\pi n_i d_e / \lambda), \quad (6)$$

where n_i is the imaginary part of the refractive index and λ is the wavelength. As defined in Eq. (5), d_e is the representative distance a photon travels through a particle without internal reflections or refraction occurring. In Mitchell (2000), henceforth M00, it is shown that relevant processes not included in ADA can be parameterized in terms of ADA such that this modified ADA yields absorption efficiencies with errors $\sim 10\%$ or less relative to Mie theory. Absorption processes represented in this modified ADA are based on the principle of effective photon path, indicating that d_e is the relevant dimension for single particle-radiation interactions. We can take this a step further, and relate the diameter of a sphere, D , to its effective distance, d_e . Using ice spheres as an example in Eq. (5), mass $m = \rho_i(\pi D^3/6)$ and projected area $P = \pi D^2/4$, giving

$$d_e = 2/3 D. \quad (7)$$

If there is an effective photon path for a single particle, it can be asked if there is also an effective photon path D_{eff} for the entire size distribution, $N(D)$. Substituting Eq. (7) for $D_{\text{eff}} = 3d_e/2$ into Eq. (6) yields

$$Q_{\text{abs,ADA}} = 1 - \exp(-8\pi n_i D_{\text{eff}} / 3\lambda) , \quad (8)$$

where $Q_{\text{abs,ADA}}$ is the absorption efficiency representing the entire size distribution based on ADA and the concept of effective photon path. Equation (8) represents absorption due only to a particle's geometric cross section. It has been expanded by Mitchell (2000) to include the processes of internal reflection/refraction and photon "tunneling," which collectively are well approximated by

$$Q_{\text{abs}} = (1 + C_1 + C_2) Q_{\text{abs,ADA}} . \quad (9)$$

The leading term (the "1") on the right side of Eq. (9) represents absorption via the particle's cross section; the term C_1 accounts for absorption due to internal reflection/refraction; and C_2 is the photon tunneling term. Tunneling here is a process by which photons beyond the particle's geometric cross-section are absorbed. Expressions for the constants C_1 and C_2 are given in Mitchell (2000) and are not repeated here, except to note that they depend on ice-crystal particle size, shape, wavelength, and index of refraction.

In summary, Eq. (9) is the absorption efficiency that represents the entire size distribution based on ADA and the concept of effective photon path. Based on the formalism in Eq. (5), such a photon path should be defined for ice size spectra as

$$D_e = \text{IWC} / (\rho_i P_t) , \quad (10)$$

where IWC is the cirrus cloud ice water content (g cm^{-3}), and P_t is the total projected area of all ice crystals in the size distribution (with units of area per unit volume; e.g., $\text{cm}^2 \text{ cm}^{-3} = \text{cm}^{-1}$). Projected area P_t is the geometric cross-sectional area per unit volume of a distribution of ice crystals with random orientations. Based on Eq. (7), the effective diameter of the size distribution should then be $3/2 d_e$ or

$$D_{\text{eff}} = 3 \text{ IWC} / (2 \rho_i P_t) . \quad (11)$$

The same formalism applies to water clouds. That is, the standard definition of effective radius used for water clouds, r_{eff} , is equivalent to Eq. (11). Defining r_{eff} as $1/2 D_{\text{eff}}$, then

$$r_{\text{eff}} = 3 \text{ LWC} / (4 \rho_w P_t) , \quad (12)$$

where LWC is the liquid water content (g cm^{-3}), and ρ_w is the density of liquid water (1 g cm^{-3}). The LWC and P_t are defined as

$$\text{LWC} = \int \rho_w (4/3) \pi r^3 N(r) dr , \quad (13)$$

and

$$P_t = \int \pi r^2 N(r) dr , \quad (14)$$

where $N(r) dr$ is the size distribution with respect to radius. Substituting Eqs. (13) and (14) into Eq. (12) yields the traditional definition of effective radius, as defined in Slingo (1989):

$$r_{\text{eff}} = \frac{\int r^3 N(r) dr}{\int r^2 N(r) dr} \quad (15)$$

This illustrates how there is simply one general definition for effective radius or diameter for all clouds, regardless of phase, and that this definition can be understood physically as the representative photon path for all particles in the size distribution.

4.2.4. Absorption of Infrared Radiation by Ice Clouds

The coefficient for absorption is defined as follows:

$$\beta_{\text{abs}} = \int_0^{\infty} Q_{\text{abs}}(D, \lambda) P(D) N(D) dD, \quad (16)$$

where Q_{abs} is the absorption efficiency at wavelength λ for ice crystals of maximum dimension D ; $P(D)$ is the projected area for a crystal of maximum dimension D , and $N(D)$ is the ice-crystal particle size distribution. D has dimensions of length, P of area, and $N(D)$ of “per unit volume per unit length;” Q_{abs} is dimensionless. It follows that the absorption coefficient β_{abs} has units of inverse length.

If D_{eff} is the appropriate dimension for describing particle-radiation interactions for a size distribution, then it is natural to ask what the consequences might be if the absorption efficiency Q_{abs} were to be taken outside the integral of Eq. (16), and solved for in terms of D_{eff} . This results in the following simple equation

$$\beta_{\text{abs}} = \underline{Q}_{\text{abs}} P_t, \quad (17)$$

where $\underline{Q}_{\text{abs}}$ is the absorption efficiency representing the entire size distribution; and where

$$P_t = \int_0^{\infty} P(D) N(D) dD \quad (18)$$

is the geometric cross-sectional area of the entirety of ice crystals in the size distribution $N(D)$, with units of area per unit volume (e.g., $\text{cm}^2 \text{cm}^{-3} = \text{cm}^{-1}$). For irregularly shaped crystals it is easy to comprehend that $P(D)$ is a function of crystal shape and size. The mass- and projected-area dimensional power law expressions for m and P of an individual ice crystal are

$$m = \alpha D^{\beta} \quad (19)$$

and

$$P = \sigma D^{\delta}, \quad (20)$$

where D is the maximum dimension of the ice crystal (cm), $[P] = \text{cm}^2$, and $[m] = \text{g}$. It is seen that the constants σ , δ , α , and β relate the cross-sectional area P and mass m of a single ice crystal to that crystal's maximum dimension D . These constants are determined empirically for different ice-crystal shapes using cirrus microphysics probe observations, and are tabulated by Mitchell (1996).

Solving Eq. (17) for absorption efficiency finally yields

$$\underline{Q}_{\text{abs}} = \beta_{\text{abs}} / P_t. \quad (21)$$

Both the absorption coefficient β_{abs} and the cross-sectional area P_t of the entire size distribution $N(D)$ are dependent on the amount and shape of the ice crystals that comprise the cirrus cloud. However, the absorption efficiency Q_{abs} is a normalized metric of absorption that depends only on crystal size, shape, wavelength, and refractive index. Thus if it is possible to compute β_{abs} and P_t for a “representative” unit volume of the actual ice-crystal size distribution, their ratio will yield that distribution’s absorption efficiency. This forms the basis for computing cirrus TIR emissivity values in our retrieval paradigm, and is outlined next.

The gamma size distribution has the form

$$N(D) = N_0 D^v e^{-\Lambda D}, \quad (22)$$

where N_0 is related to the IWC and number concentration N . The gamma distribution $N(D)$ has mean $(v+1)/\Lambda$ and variance $(v+1)/\Lambda^2$. Again, as a reminder, D is the maximum dimension of an ice crystal in a cirrus cloud that has a size distribution of the form given by Eq. (22).

Inserting Eqs. (9), (20), and (22) into Eq. (16) yields

$$\begin{aligned} \beta_{\text{abs}} = & \sigma N_0 \Gamma(\delta+v+1) / \Lambda^{\delta+v+1} - \sigma N_0 \Gamma(\delta+v+1) / (\Lambda+g)^{\delta+v+1} \\ & + a_1 \sigma N_0 \Gamma(\delta+v+1) / (\Lambda+g)^{\delta+v+1} - a_1 \sigma N_0 \Gamma(\delta+v+1) / (\Lambda+2g)^{\delta+v+1} \\ & + a_2 \sigma N_0 \Gamma(\delta+v+m+1) / (\Lambda+\varepsilon)^{\delta+v+m+1} - a_2 \sigma N_0 \Gamma(\delta+v+m+1) / (\Lambda+g+\varepsilon)^{\delta+v+m+1} \end{aligned} \quad (23)$$

where Γ denotes the gamma function, and where all other variables are as described by Mitchell (2000). In summary the first line represents absorption processes due (a) purely to the geometric cross-section of an ice crystal, (b) the second line denotes internal reflection/refraction, and (c) the third line quantifies photon “tunneling,” which includes large-angle diffraction and wave resonance phenomena (Mitchell, 2000). Tunneling is a process by which photons beyond the particle’s physical cross section are absorbed.

A detailed analysis of Eq. (23) (see Mitchell, 2000) is not repeated here except to note with importance that the absorption coefficient β_{abs} is dependent on the shape of the size distribution $N(D)$ as prescribed by the parameters v and Λ , and on ice-crystal shape as well via the coefficients σ and δ .

It is also possible to compute the geometric cross-sectional area of all the crystals in the size distribution by substituting Eqs. (20) and (22) for $P(D)$ and $N(D)$, respectively, in Eq. (18) to obtain

$$P_t = \int_0^{\infty} \sigma N_0 D^{\delta+v} e^{-\Lambda D} dD.$$

This in turn can be integrated analytically to yield

$$P_t = \sigma N_o \Gamma(\delta+v+1) / \Lambda^{\delta+v+1} . \quad (24)$$

Now Eq. (21) can be used with Eqs. (23) and (24) to compute the absorption efficiency Q_{abs} of the entire size distribution. Such computations have been compared with numerical Mie theory integrations over size distributions of water droplets, and against observations of absorption efficiencies for non-spherical ice crystals. Errors relative to $Q_{abs,Mie}$ are low (generally within 10%), and for small ice crystals grown in a cloud chamber the errors between observation and the modified ADA theory are within 3% at MWIR and TIR wavelengths (Mitchell, 2001).

One of the major output components of our retrieval approach (as defined by simultaneous solution of Eq. (2) at two wavelengths) is the estimated emissivity ε at the 10.8- μm TIR channel, corresponding to temperature T_{cld} at the cloud's radiative center of mass. Based on this, the algorithm determines ε at any other infrared wavelengths, based on the radiation transfer theory described by Eq. (21). The theoretical development for emitted terrestrial radiation is described in its most fundamental form by these equations, and is applied below for the purpose of retrieving IWP. Assuming no scattering at thermal wavelengths,

$$\varepsilon = 1 - \exp(-\tau_{abs} / \cos\theta_{\text{sat}}) , \quad (25)$$

where θ_{sat} is the satellite zenith angle and τ_{abs} is the absorption optical depth. Dividing optical depth by the factor $\cos\theta_{\text{sat}}$ accounts for increased path length through the cirrus due to non-nadir views. For a cirrus cloud where the size distribution (SD) is invariant with in-cloud position, the absorption optical depth is given by

$$\tau_{abs} = \beta_{abs} \Delta z , \quad (26)$$

where Δz is the cloud physical depth (from top to base) and β_{abs} is the absorption coefficient, defined by Eq. (23).

4.2.5. Ice Water Path

Equation (26) can now be combined to solve for the ice water path IWP (g cm^{-2}), which is the melted-equivalent water mass per unit area of a vertical column through the entire extent of the cirrus cloud. By definition, and assuming that IWC is the vertically averaged value,

$$\text{IWP} = \text{IWC} \Delta z$$

and Eq. (11) becomes

$$D_{\text{eff}} = 3 \text{ IWP} / (2 \rho_i P_t \Delta z) , \quad (27)$$

giving

$$\text{IWP} = 2 \rho_i D_{\text{eff}} \tau_{abs} / (3 Q_{abs}) \quad (28)$$

with the help of Eq. (17) solved for P_t . Substituting for τ_{abs} in (25) using (28), (25) can be rewritten as

$$\varepsilon = 1 - \exp(-3 \text{ IWP} Q_{abs} / 2 \rho_i D_{\text{eff}} \cos\theta_{\text{sat}}) . \quad (29)$$

Solving Eq. (29) for IWP yields

$$\text{IWP} = -2 \rho_i D_{\text{eff}} \cos\theta_{\text{sat}} \ln(1 - \epsilon) / (3 Q_{\text{abs}}) . \quad (30)$$

Note that D_{eff} appears both in the numerator and in the denominator, since Q_{abs} is dependent on particle size via Eq. (8).

Fortunately, we have exploited a means of estimating D_{eff} in tropical anvil and mid-latitude cirrus as a function of cirrus environmental temperature (Ivanova et al., 2000). The tropical scheme is based on 93 size distributions from three tropical anvils reported in McFarquhar and Heymsfield (1996) for the CEPEX field campaign, three tropical anvils reported in Knollenburg et al. (1993), and a tropical tropopause cirrus case (Heymsfield 1986). The mid-latitude scheme is based on over 1000 in-situ measurements of cirrus taken during ARM and FIRE campaigns in the central U.S. (Ivanova et al., 2000).

4.2.6. Algorithm Description Summary

With a methodology to compute IWP, emissivity as a function of wavelength, and effective particle size as a function of cirrus environmental temperature, it is now possible to both simulate and solve a simultaneous set of equations as defined by Eq. (2) for two infrared bands using an iterative numerical approach. In application the clear-scene radiance estimate $I_{\lambda, \text{clr}}$ in Eq. (2) is made by averaging the radiances of nearby cirrus-free pixels (as determined by a pre-computed cloud mask) on a land-water background basis. Figure 29 illustrates graphically the process of retrieving cirrus emissivity and temperature. Effective particle size is tied to temperature, and also varies throughout the iteration process.

In Figure 29 are plots of mathematically possible pairs of cirrus temperature and emissivity for a given set of satellite radiance observations. The radiance observations correspond to an MWIR brightness temperature of 273 K, and a TIR temperature of 265 K. Note that for a single wavelength the number of theoretically possible pairs (ϵ, T) is infinite. This ambiguity is resolved, however, by choosing the retrieved pair as that which satisfies satellite radiance observations at two infrared wavelengths simultaneously. This forms the fundamental basis of our retrieval paradigm.

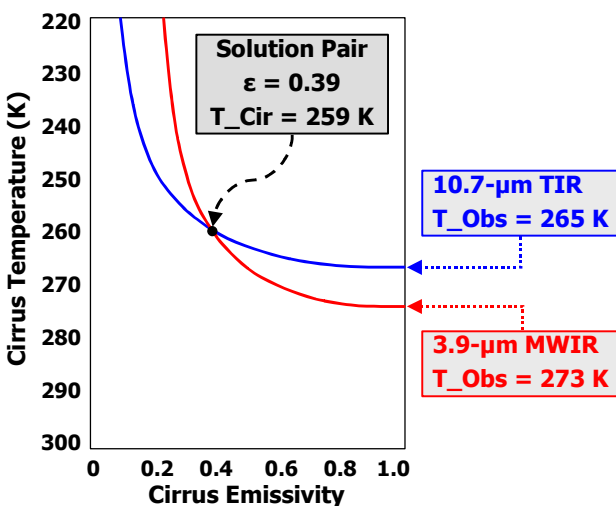


Figure 29: Plot of all theoretically possible pairs of cirrus emissivity and effective temperature for a given set of observed MWIR and TIR brightness temperatures

4.3. Numerical Attributes of the Infrared IWP Retrieval Algorithm

4.3.1. Algorithm Trade Space

Numerical sensitivity calculations were made to help determine the performance characteristics of the IWP infrared retrieval algorithm. Simulations of top-of-atmosphere (TOA) upwelling radiances in the 3.9-μm MWIR and 10.8-μm TIR bands of the GOES Imager were made in the following trade space. Two atmospheric temperature and moisture profiles were used to simulate fundamentally different atmospheres encountered in the tropics and mid-latitudes: tropical (warm and moist, 8-km pressure scale height, 300-K surface temperature, 17-km tropopause), and the 1976 U.S. Standard (temperate and moderately dry, 7.7-km pressure scale height, 288-K surface temperature, 12-km tropopause).

Two diverse ice-crystal shapes were simulated: planar polycrystals and rosettes. Relations between mass, projected area, and ice-crystal effective diameter were derived using CEPEX and ARM in-situ observations of tropical and mid-latitude cirrus, according to Eqs. (19) and (20), and as given in Mitchell et al. (1996).

Cirrus physical thickness, i.e., the linear distance between cirrus base and cirrus top, was allowed to vary between 1 and 5 km. No cirrus-layer temperature was allowed to exceed 258 K, and cirrus tops were not allowed to be higher than the tropopause. Vertical inhomogeneity in ice-crystal particle size and IWC was also modeled. Particle size and size-distribution shape within the cirrus were prescribed by environmental temperature, crystal shape, and atmosphere (tropical or mid-latitude) as prescribed by Ivanova et al. (2000). Total cirrus IWP (from base to top) was scaled into a monotonic IWP vertical profile according to the Clausius-Clapeyron relation. This effectively assumes a steady-state, non-precipitating cirrus cloud for purposes of simulation.

A sensor noise model was simulated as a normal distribution of random noise with an MWIR NE Δ T of 0.07 K and a TIR NE Δ T of 0.05 K, each at 300 K.

In review, the overall IWP retrieval paradigm is to write Eq. (2) for two wavelengths and solve them simultaneously for the unknowns ϵ and T_{cld} using an iterative numerical approach. $I_{\lambda,\text{clr}}$ is the TOA radiance that would be observed in an otherwise cirrus-free pixel, and is dominated in the MWIR and TIR windows by the underlying land- or ocean-surface thermal emission component. The term “cirrus-free” is chosen intentionally here to denote that the underlying object may be an opaque water-droplet cloud. In theory this component provides a uniform source of energy that is attenuated differentially, according to wavelength, by the cirrus cloud. This differential signal is in turn what allows for retrieval of cirrus properties.

In practice, $I_{\lambda,\text{clr}}$ is estimated using cirrus-free radiances “nearby” the cirrus cloud itself. If the cirrus-free pixels are “very close” to the cirrus pixel, errors in $I_{\lambda,\text{clr}}$ are likely to be low. Conversely, errors in $I_{\lambda,\text{clr}}$ may grow higher as the clear pixels lie increasingly “farther” from the cirrus pixels. Thus the $I_{\lambda,\text{clr}}$ estimation process represents a source of error in the cirrus retrievals.

Consequently, a clear-column noise model was simulated using a normal distribution of random noise with a mean of 0 K, and standard deviation of 1 K. Thus it is assumed that 67% of the MWIR-TIR $I_{\lambda,\text{clr}}$ estimates in our IWP retrieval-sensitivity simulations are accurate within ± 1 K, 96% within ± 2 K, and 99% within ± 3 K.

In the following two sections are described the results of our numerical sensitivity studies. Section 4.3.2 discusses IWP retrieval performance metrics using simulations with no sensor and $I_{\lambda,\text{clr}}$ noise, and Section 4.3.3 contains results obtained with the sensor and surface-emission noise models.

4.3.2. Noise-free IWP Retrieval Sensitivities

Sensitivities in retrieved ice-water path were computed, assuming zero error in sensor noise and surface skin temperature estimates, in order to learn about the numerical characteristics of the IWP retrieval algorithm. Accuracy and precision were computed for polycrystals and rosettes, and the results were plotted for each cirrus thickness (1-5 km) as well as the average for all thicknesses together. The all-thickness performance metrics were weighted to simulate global conditions using the statistics of Sassen and Barnett (2000), who report from seven years of ground-based lidar data that non-precipitating cirrus of 1, 2, 3, 4, and 5-km thickness occurs approximately with 0.21, 0.35, 0.28, 0.13, and 0.03 frequency of occurrence, respectively (Sassen and Barnett, 2000).

Describing the results of the entire simulation trade study requires the descriptions of 324 plots, and so will not be presented here in their entirety. Sample plots will be discussed, and summaries of the complete sensitivity will be presented in their place.

Figure 30 contains a plot of expected accuracy for the following simulation: crystal shape is planar polycrystal; atmosphere is tropical; IWP ranges between 0 and 420 g/m²; and cirrus thicknesses range between 1 and 5 km. A total of 1837 simulated retrievals were performed and plotted on D_{me} -IWP axes as a function of cirrus thickness. The CMIS IWP accuracy requirement is 10% or 5 g/m², whichever is larger. Colors denote accuracy (g/m²), and black denotes regions of D_{me} -IWP space where the simulated retrievals do not converge. Non-convergence primarily occurs when the cirrus cloud signature is “saturated” out in one or both of the thermal infrared

bands. In other words, once the cloud becomes optically thick, the addition of more ice will not change the MWIR and/or TIR radiances. This results in an inability to resolve with certainty the non-uniqueness of the radiative-transfer theory since many combinations of IWP and D_{me} will yield, according to theory, the same upwelling TOA radiance.

From Figure 30 two main retrieval attributes are evident. First, except for the combination of physically thin cirrus and relatively large ice crystals, IWP in general is underestimated and the magnitude of the underestimation increases with increasing cirrus thickness. As cirrus thickness and/or IWP increases, the larger crystals near cloud base are increasingly more obscured by smaller crystals near the cloud top. Our cirrus model has this behavior since it prescribes that crystal size decreases with in-cloud temperature. For a fixed ice water content (g/m^3), smaller crystals have a larger cross section absorbing area than larger crystals. Being more efficient absorbers of upwelling energy, small crystals above tend therefore to “hide” or “subdue” the influence of the larger crystals below. Subsequently the upwelling MWIR and TIR radiances are not maximally sensitive to the presence of the larger crystals, in turn causing IWP to be underestimated. The effect increases in severity as more and more small crystals in the upper layers of the cirrus mask out the larger crystals in the lower layers.

From Figure 30 the second dominant retrieval attribute is that IWP algorithm retrieval space decreases with increasing cirrus thickness. This occurs for the same reasons just described in the previous paragraph. Essentially, as cirrus thickness increases, more and more smaller crystals are present in the cloud. In turn these crystals mask out the influence of the larger crystals below, which results in a weighting toward the smaller crystals as prescribed by the IWP retrieval physics.

The consistent underestimate of IWP is not all bad because the error is systematic. The plots in Figure 30 indicate that the underestimation is very repeatable, suggesting that thermal-IR retrievals of IWP can be adjusted according to these results.

Figure 31 contains a plot of expected precision for the conditions simulated in Figure 30. The CMIS IWP precision requirement is 5%. Colors denote percent precision, defined as the standard deviation of the retrieval errors normalized by the truth IWP. Black denotes regions of D_{me} -IWP space where the simulated retrievals do not converge. In general, percent precision is large for small values of IWP and small for large values of IWP. In absolute precision space, the majority of the simulated-retrieval precisions fall below $5 g/m^2$, indicative of a consistently stable and repeatable retrieval formulation.

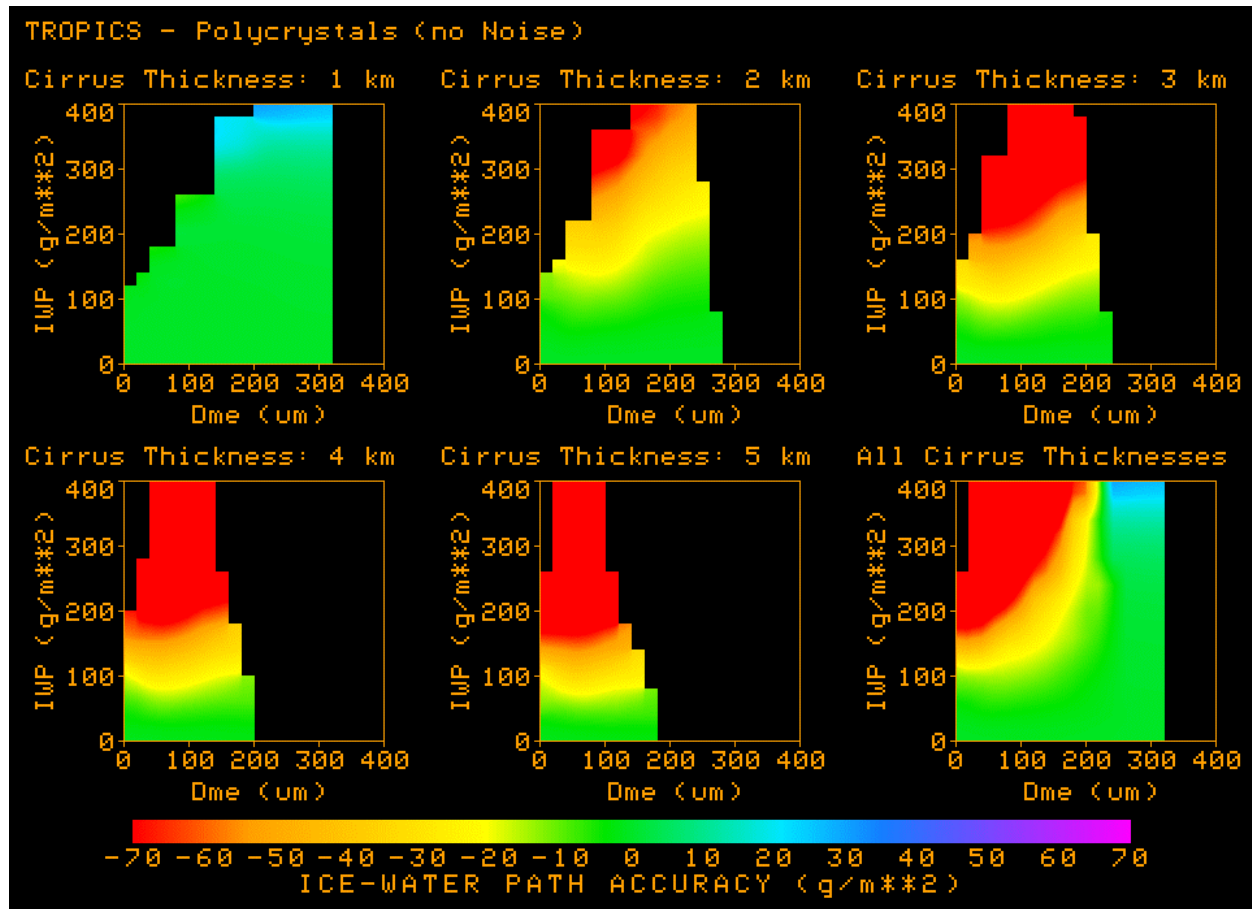


Figure 30: Noise-free IWP-retrieval accuracies for simulations of planar polycrystals in a tropical atmosphere, and for varying cirrus thicknesses.

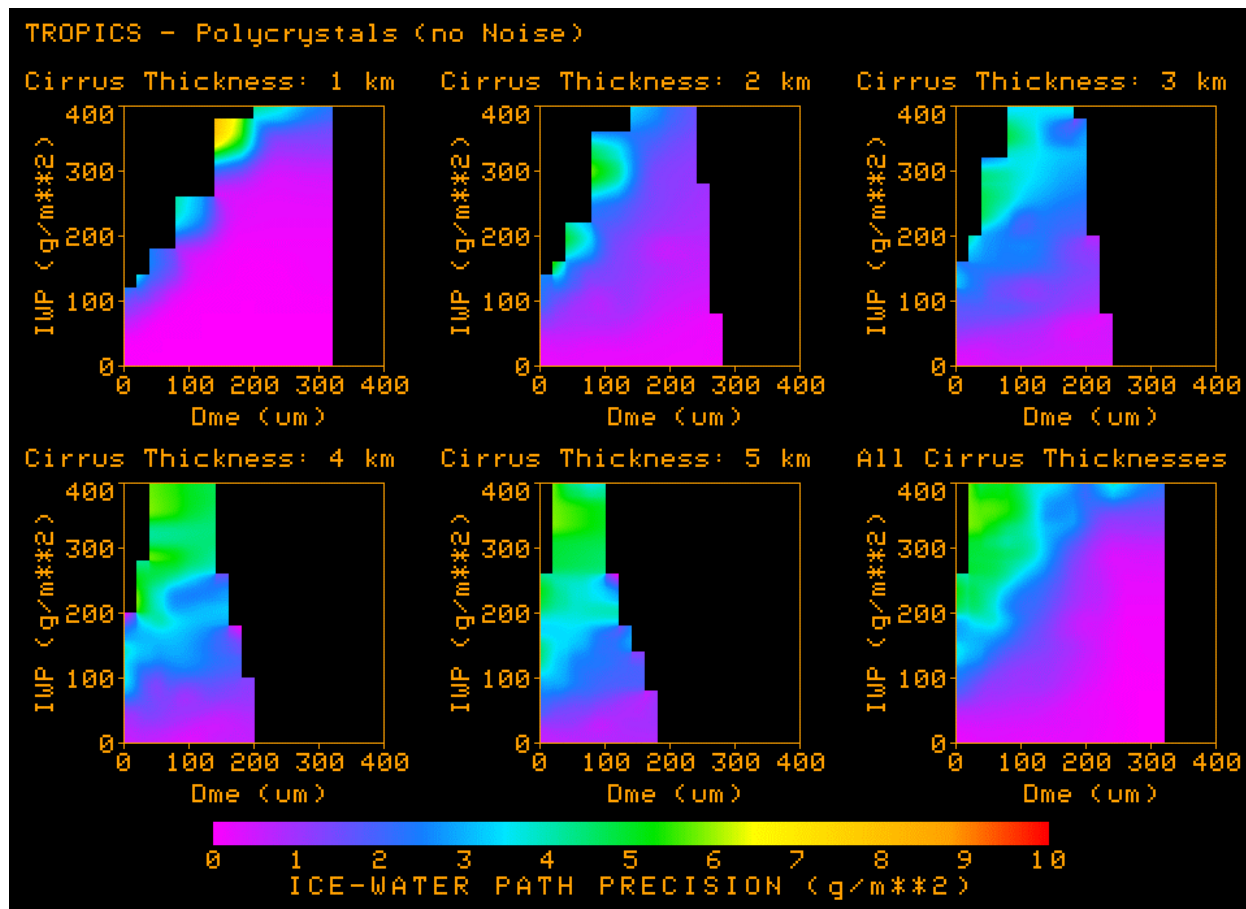


Figure 31: Noise-free IWP-retrieval precisions for simulations of planar polycrystals in a tropical atmosphere, and for varying cirrus thicknesses.

Figure 32 (Figure 33) summarizes the accuracy (precision) performance metrics for planar polycrystals in a tropical atmosphere. Color codes in Figure 32 (Figure 33) are as follows: blue denotes portions of IWP- D_{me} retrieval space where accuracy (precision) requirements are exceeded, green denotes where requirements are met, yellow denotes where accuracy (precision) is within a factor of two, and red denotes where accuracy (precision) fails to meet requirements by more than a factor of two.

Figure 32 shows that accuracy requirements are met or exceeded except when IWP is large and D_{me} is small. However, this is the region in IWP- D_{me} retrieval space where the CMIS microwave UR IWP retrievals have increasingly greater skill. Figure 33 shows that precision requirements are met everywhere in simulated retrieval space.

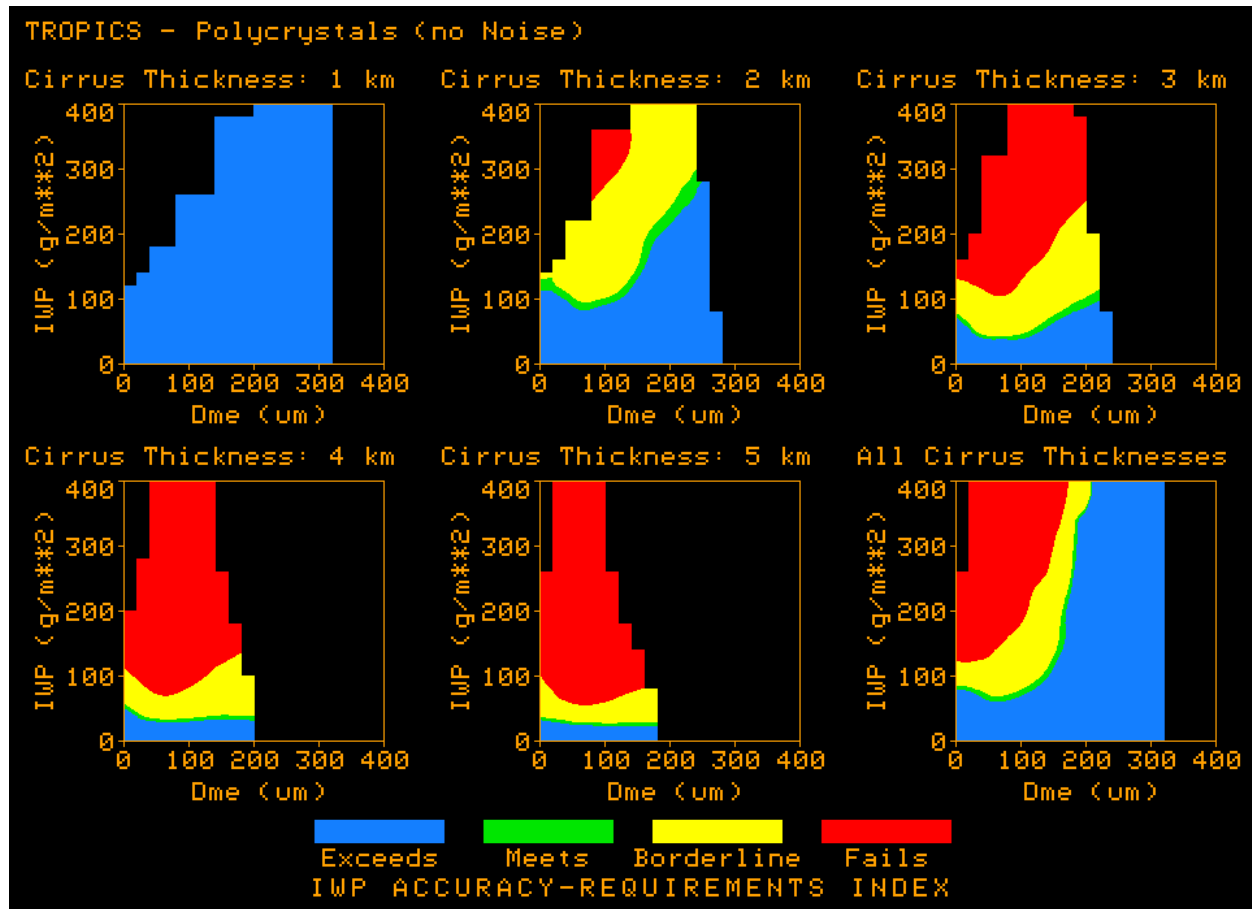


Figure 32: Summary of accuracy performance indices for planar polycrystals in a tropical atmosphere (noise free).

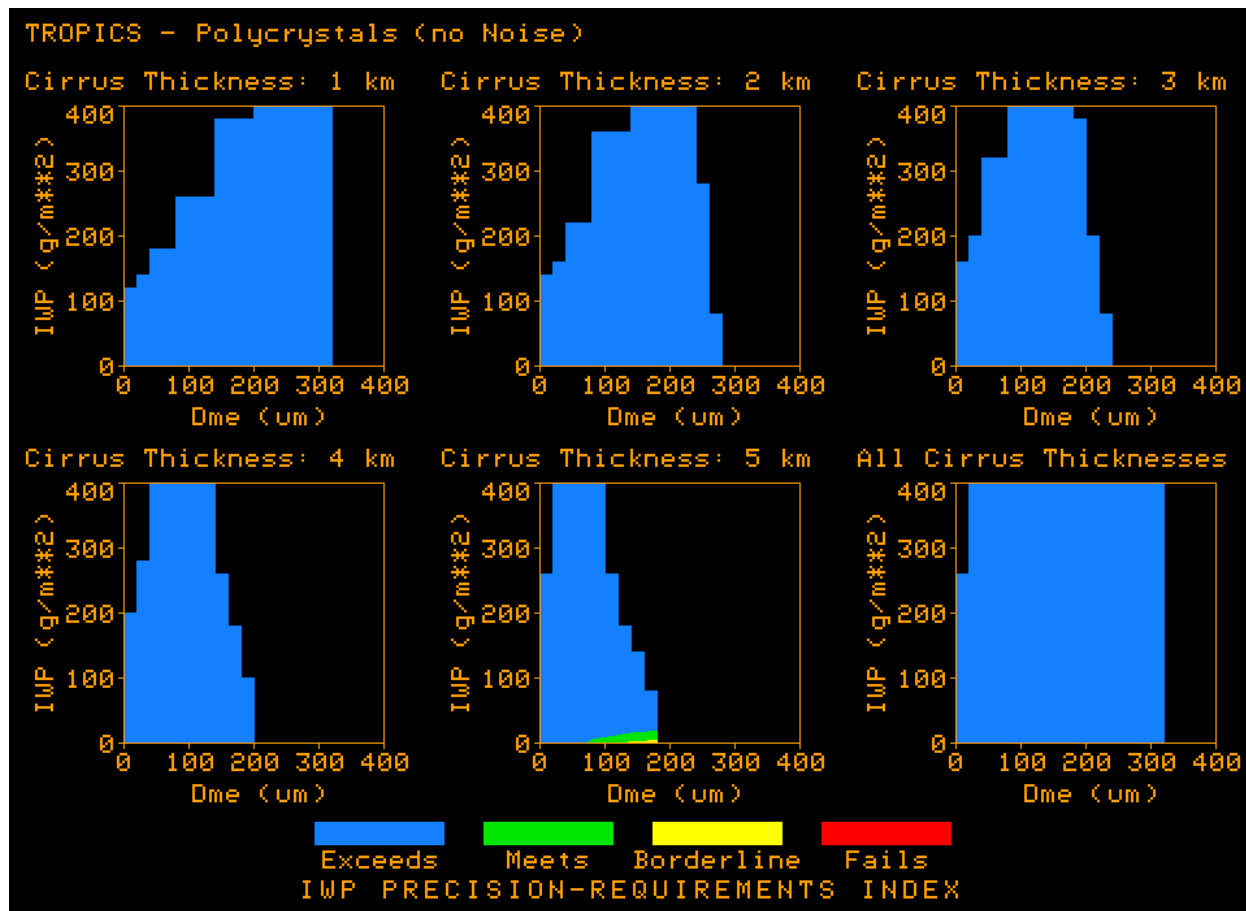


Figure 33: Summary of precision performance indices for planar polycrystals in a tropical atmosphere (noise free).

4.3.3. IWP Retrieval Sensitivities to Sensor and Clear-Scene Noise

Remember that the simulation results discussed in Section 4.3.2 do not include noise effects and errors in the estimation of clear-scene radiances. Those simulations were useful, however, in learning about the numerical attributes of the IWP infrared retrieval algorithm, and about the infrared radiative transfer physics of vertically inhomogeneous cirrus clouds.

Figure 34 and Figure 35 contain accuracy and precision performance indices for the same simulation conditions outlined in Section 4.3.2, except this time with sensor and clear-scene-radiance noise effects included. As previously mentioned, sensor noise was simulated as a normal distribution of random noise with an MWIR NE Δ T of 0.07 K and a TIR NE Δ T of 0.05 K, each at 300 K. The clear-column noise model was simulated using a normal distribution of random noise with a mean of 0 K, and standard deviation of 1 K. Thus it is assumed that 67% of the MWIR-TIR $I_{\lambda, \text{clr}}$ estimates in our IWP retrieval-sensitivity simulations are accurate within ± 1 K, 96% within ± 2 K, and 99% within ± 3 K.

From Figure 34 it is seen that, for all cirrus thicknesses combined, CMIS accuracy requirements are met for small crystals only when IWP is relatively low (~ 80 g/m² or less when D_{me} is less than ~ 180 μm), but is routinely met for all IWP when D_{me} is above ~ 180 μm . For small crystals and large IWPs retrieval accuracies are poor; however, in this region of IWP space the upwelling microwave radiances become increasingly sensitive to the large amounts of ice mass in the cloud. Thus the infrared and microwave retrievals complement each other well in IWP- D_{me} space.

Figure 35 contains the precision performance indices for the “noisy” retrievals. CMIS precision requirements are met except when IWP is low. This is because requirements prescribe that retrieval precision be within 5%. When there is neither sensor measurement nor clear-scene radiance error this precision requirement is universally met (recall Figure 33). The reason for the poorer performance in the “noisy” retrievals is as follows.

When the cirrus ice mass is low, only a small portion of the upwelling infrared radiance signal is contributed from the cloud itself. From our retrieval point of view the final IWP estimate is strongly dependent on the wavelength-respective cloudy contributions to the MWIR and TIR radiances, especially when cirrus IWP is very low. Under these conditions the dominant portion of the MWIR and TIR energy originates from the underlying surface. Thus small errors in the surface-contribution estimates yield large errors in the cirrus-contribution estimates, in turn resulting in large errors in cirrus IWP retrievals. Precision performance increases with increasing IWP because less and less of the upwelling infrared radiance signal is contributed by the underlying surface (i.e., more and more is contributed by the cirrus cloud). Subsequently any errors in clear-scene radiance estimates become increasingly less influential on the cirrus retrievals.

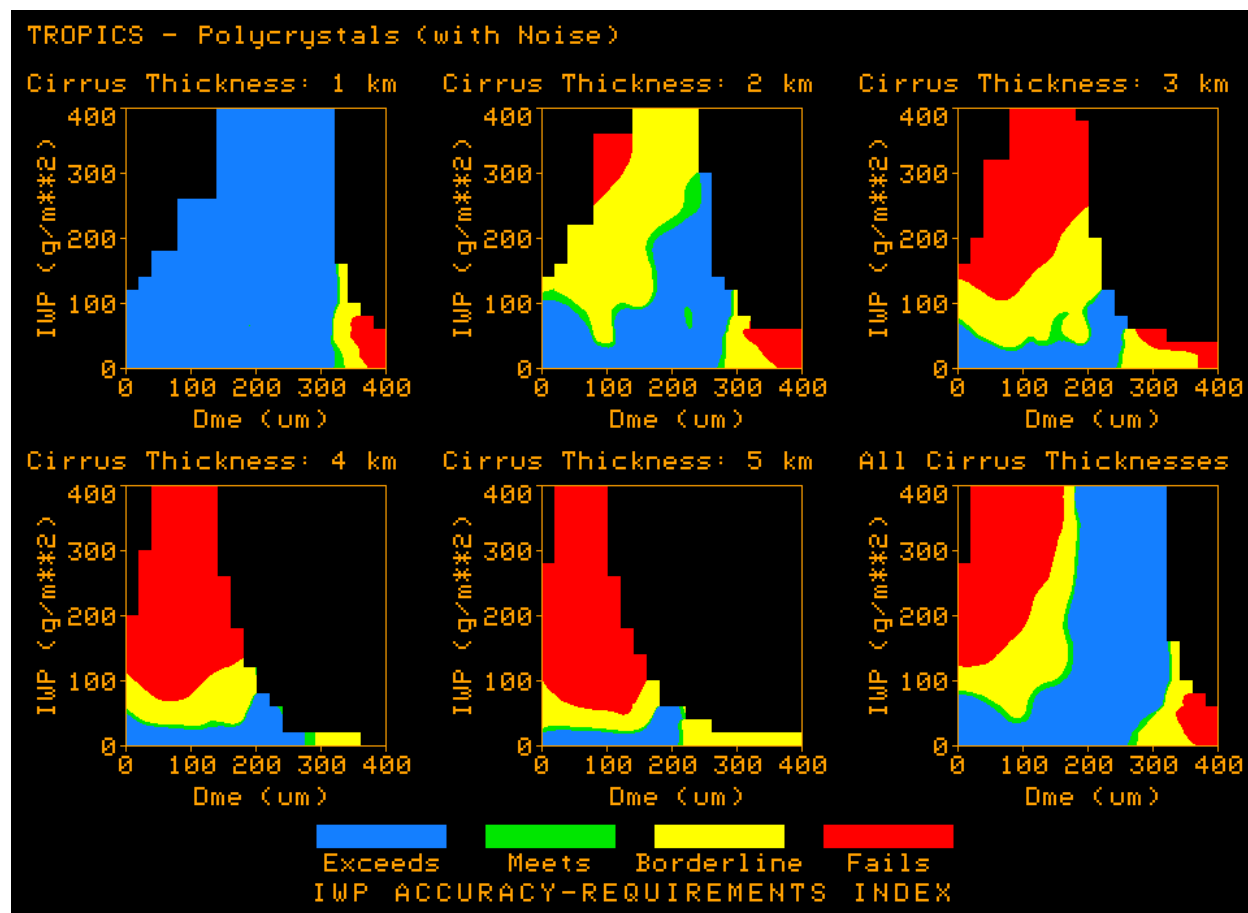


Figure 34: IWP-retrieval accuracy performance indices for simulations of planar polycrystals in a tropical atmosphere, and for varying cirrus thickness, with sensor and clear-scene noise models.

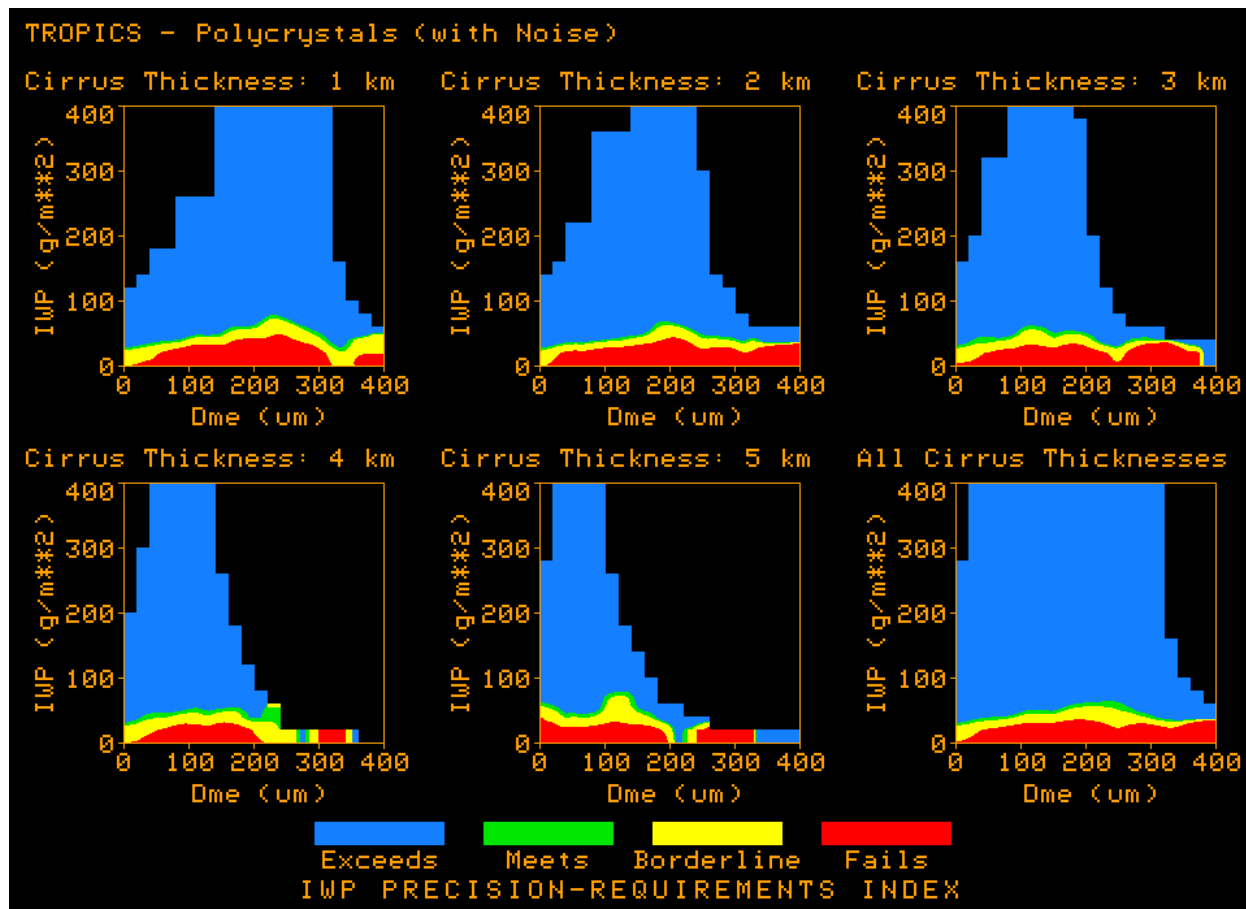


Figure 35: IWP-retrieval precision performance indices for simulations of planar polycrystals in a tropical atmosphere, and for varying cirrus thickness, with sensor and clear-scene noise models.

4.3.4. Accuracy and Precision Performance Indices for Rosettes

Simulations (with sensor and clear-scene noise models) were performed for bullet rosettes. In addition to the tropics, cirrus clouds in a U.S. Standard atmosphere were also simulated. A total of over 67,000 retrieval simulations were performed, spanning the range of conditions summarized in Section 4.3.1. This section contains summary plots of the performance indices for these retrievals.

Figure 36 and Figure 37 contain the accuracy and precision performance indices, respectively, for bullet rosettes in a tropical atmosphere. Note that the performance characteristics are similar to those for planar polycrystals. Perhaps the most notable difference between the rosette and polycrystal plots is that, in general for a fixed temperature, bullet rosettes have smaller maximum crystal dimensions than polycrystals.

Figure 38 – Figure 41 contain retrieval performance plots for polycrystals and rosettes in a mid-latitude atmosphere, the 1976 U.S. Standard. In general the IWP retrieval characteristics are similar for mid-latitudes as they are for the tropics, the most notable exception being the decreased range in observed sizes of the ice crystals from one atmosphere to the next. This has been observed in the CEPEX and ARM in-situ observations of ice crystals in non-precipitating cirrus that form the basis of the D_{eff} formulations of our IWP retrieval algorithm. Physically this is defensible in that decreased amounts of water vapor are available for crystal formation in a somewhat cooler mid-latitude atmosphere, as predicted by the Clausius-Clapeyron relation.

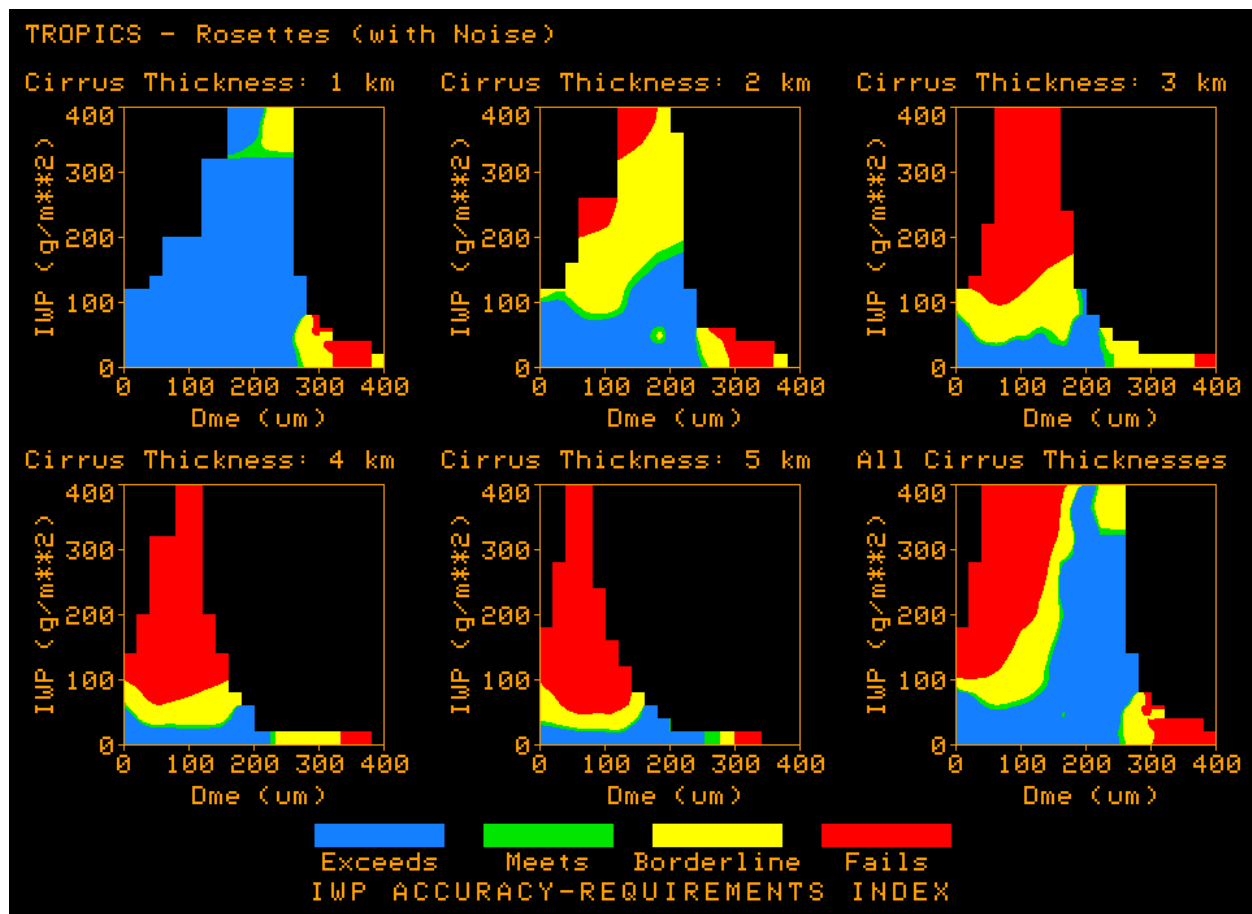


Figure 36: IWP-retrieval accuracy performance indices for simulations of rosettes in a tropical atmosphere, and for varying cirrus thickness, with sensor and clear-scene noise models.

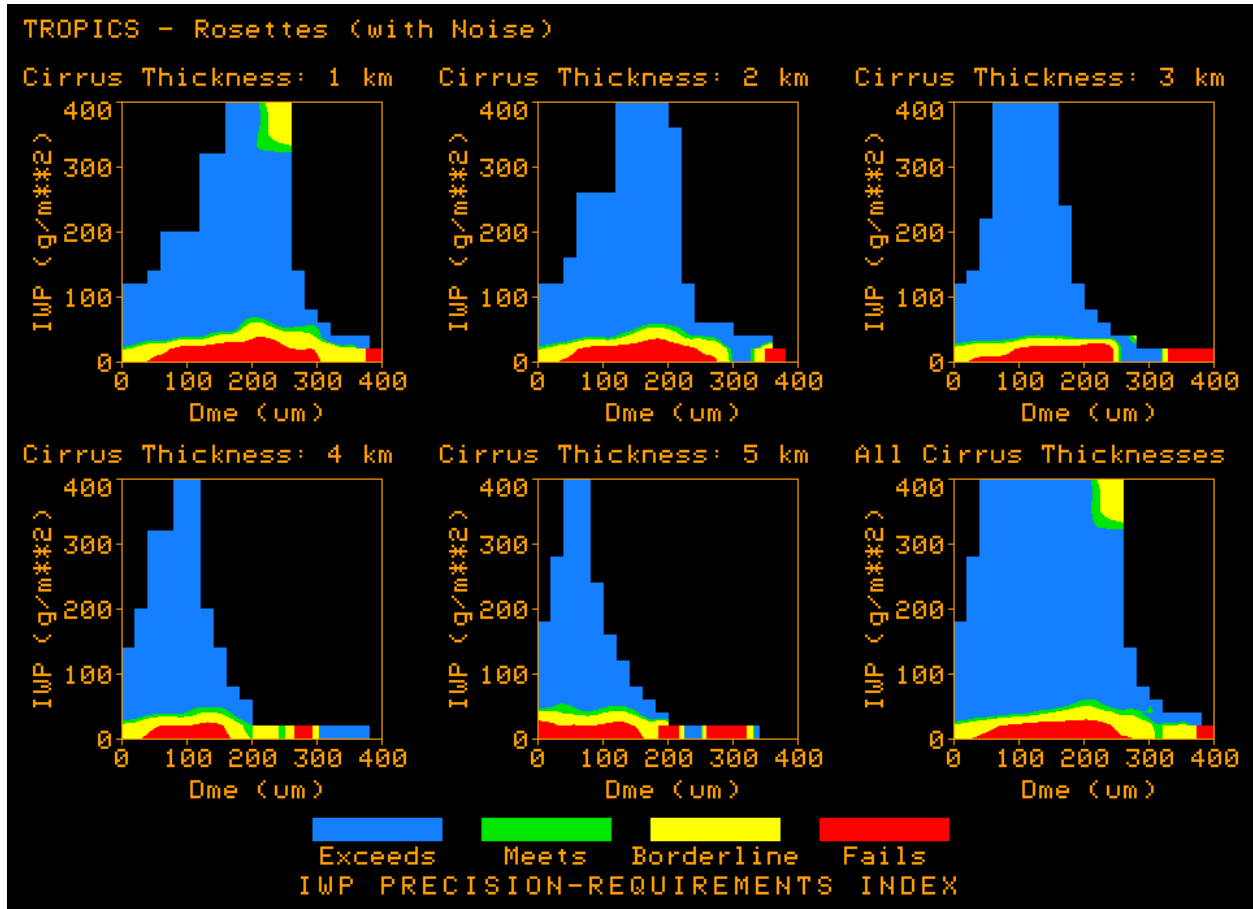


Figure 37: IWP-retrieval precision performance indices for simulations of rosettes in a tropical atmosphere, and for varying cirrus thickness, with sensor and clear-scene noise models.

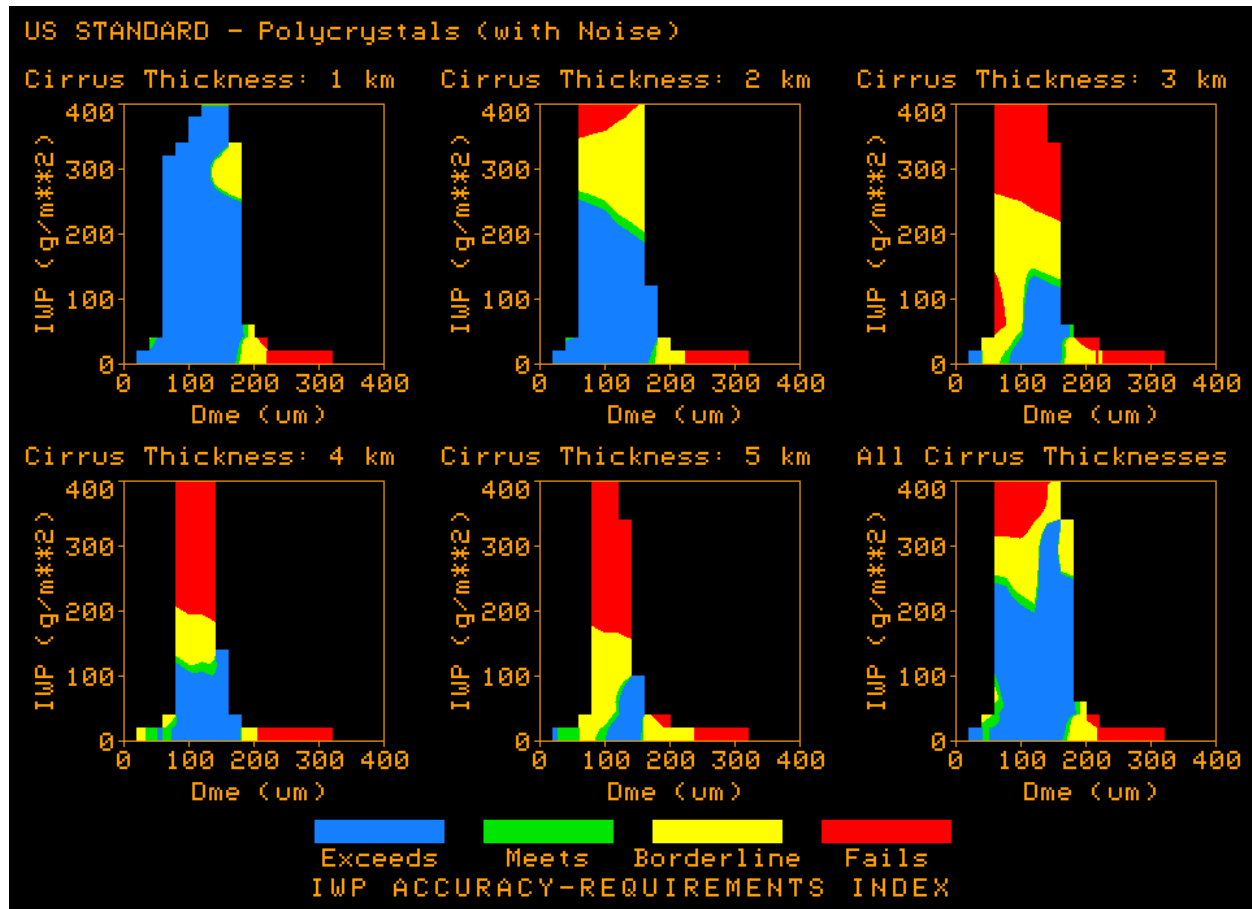


Figure 38: IWP-retrieval accuracy performance indices for simulations of planar polycrystals in a mid-latitude atmosphere, and for varying cirrus thickness, with sensor and clear-scene noise models

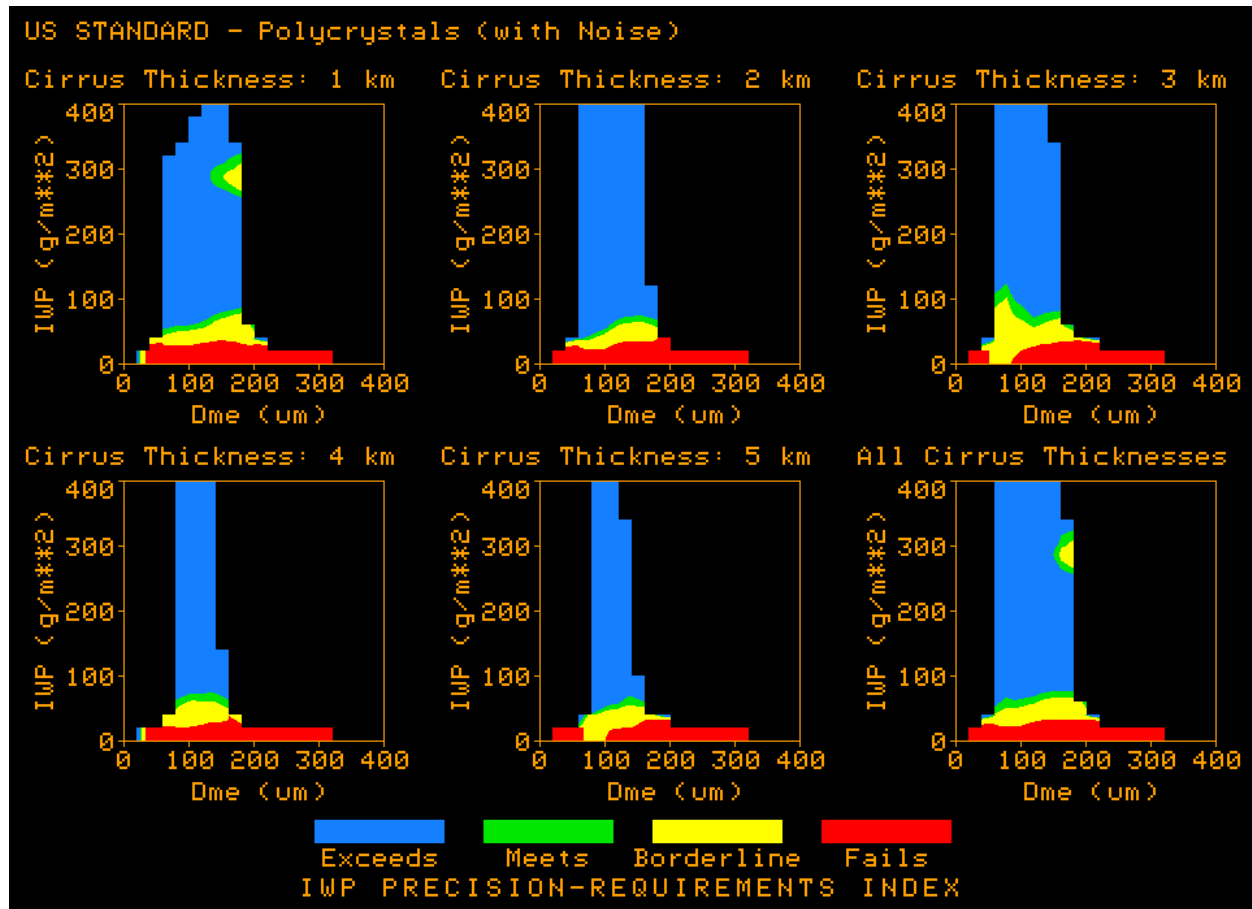


Figure 39: IWP-retrieval precision performance indices for simulations of planar polycrystals in a mid-latitude atmosphere, and for varying cirrus thickness, with sensor and clear-scene noise models.

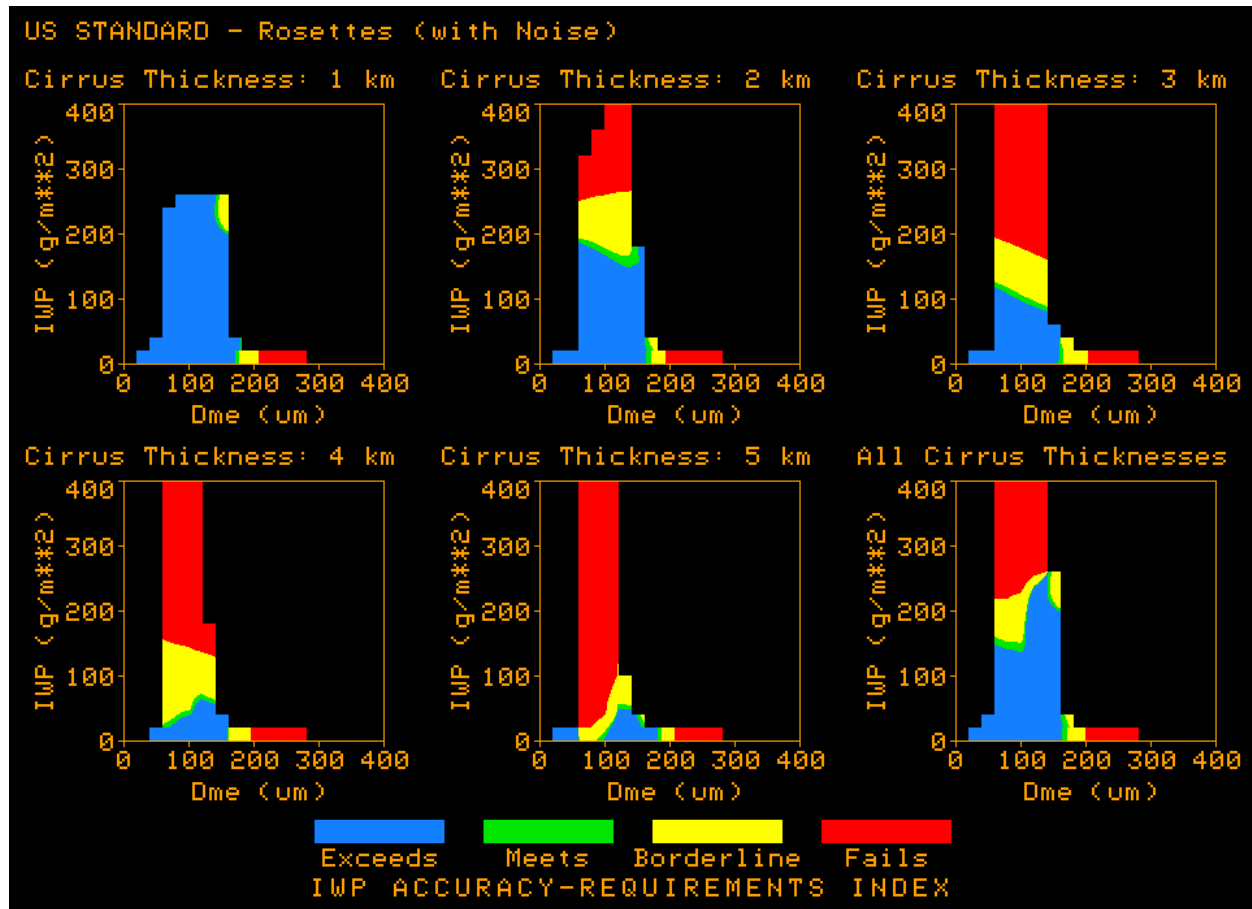


Figure 40: IWP-retrieval accuracy performance indices for simulations of rosettes in a mid-latitude atmosphere, and for varying cirrus thickness, with sensor and clear-scene noise models.

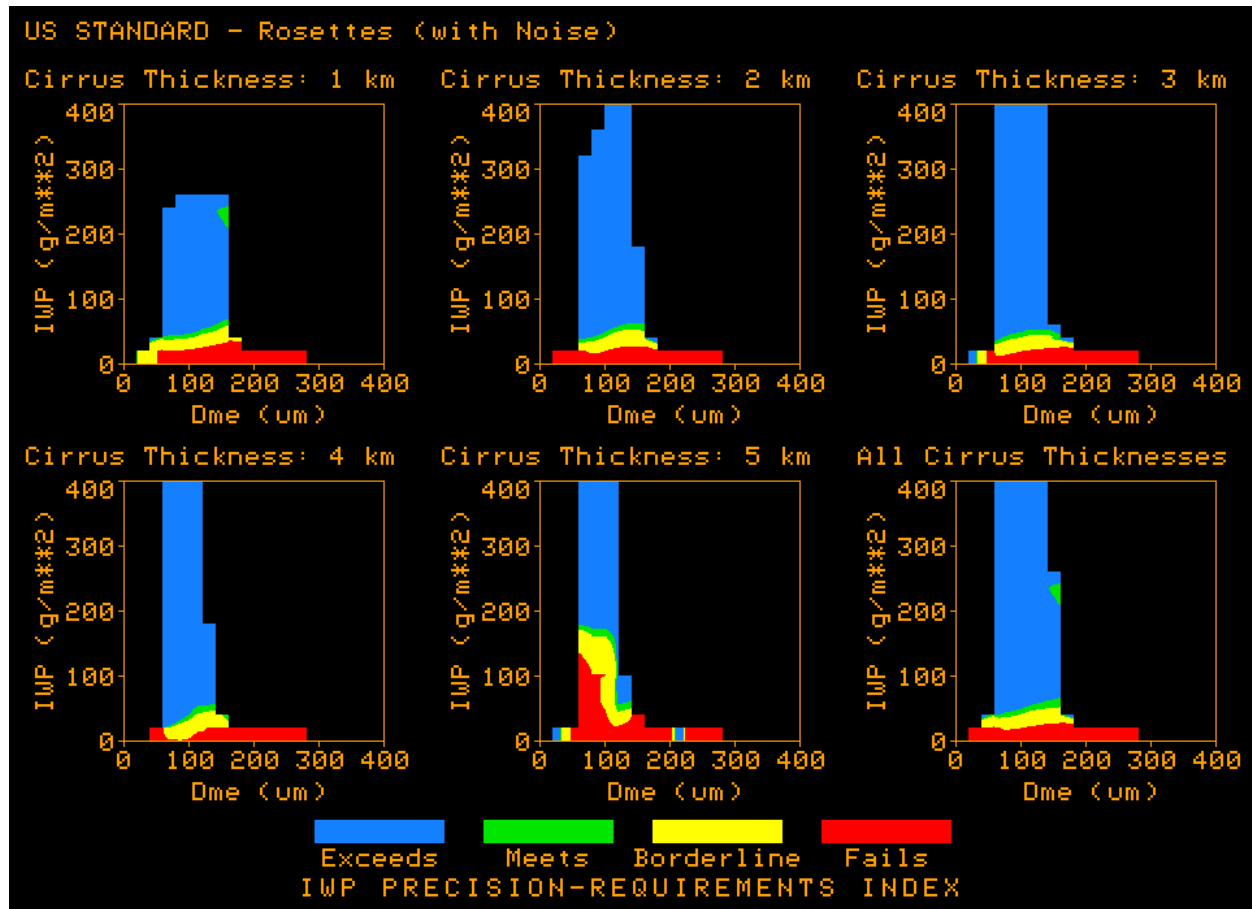


Figure 41: IWP-retrieval precision performance indices for simulations of rosettes in a mid-latitude atmosphere, and for varying cirrus thickness, with sensor and clear-scene noise models.

4.4. Summary of the Infrared Algorithm Description and Performance

Cirrus ice-water path (IWP) is estimated using a deterministic algorithm that simultaneously models the interdependent effects of IWP, ice-crystal particle size, emissivity, and cirrus temperature using radiances collected in nominal $3.9\mu\text{m}$ mid-wave infrared (MWIR) and $10.8\mu\text{m}$ thermal infrared (TIR) wavelengths. The cirrus IWP retrieval algorithm uses a simultaneous-solution approach to ensure physical consistency between multispectral satellite radiance measurements and theoretical radiative transfer calculations.

Retrieval sensitivity studies indicate that, in general, IWP is underestimated and that the magnitude of the underestimation increases with increasing cirrus thickness. As cirrus thickness and/or IWP increases, the smaller crystals near the top of the cirrus have a larger cross section absorbing area than the larger crystals below. Being more efficient absorbers of upwelling energy, small crystals above tend therefore to “hide” or “subdue” the influence of the larger crystals below. Subsequently the upwelling MWIR and TIR radiances are not maximally sensitive to the presence of the larger crystals, in turn causing IWP to be underestimated. However it has been shown that the consistent underestimate of IWP is not all bad because the error is systematic and repeatable, suggesting that thermal-IR retrievals of IWP can be adjusted according to our sensitivity results (e.g., see Figure 30).

Under conditions of very opaque cirrus when the infrared IWP retrieval accuracy is poor, microwave radiances become increasingly sensitive to the larger amounts of ice mass in the cloud. Consequently the microwave UR IWP retrievals have increasing skill, demonstrating that

the CMIS infrared and microwave IWP retrievals complement each other well in IWP- D_{me} space.

5. Final Error Budget

The requirements are not met with the added sub millimeter frequencies (325 GHz). Therefore, they are not carried out in the baseline CMIS channels. The following error budget refers to the configuration of the CMIS baseline without using the IR radiances. The use of the infrared algorithm is useful only if we keep the sub millimeter channels to fill in the gap between the D_{me} range sensed by the microwave frequencies and the range sensed by the IR radiances. Table 13 and Table 14 present the global error budget summary for the cases of knowing and not knowing the cloud top. Both the accuracy and the precision are computed as the square root of the sum of the squares of the different sources of errors.

Table 13: Error budget summary for known cloud top

	Accuracy (%)	Precision (%)
Sensor noise and environmental conditions	15	20
Unknown concentration of small particles	10	15
Particle shape/density	10	40
3D effects	5	10
Cell mismatch	7	10
Margin	10	10
Total	25%	50%

Table 14: Error budget summary for unknown cloud top

	Accuracy (%)	Precision (%)
Sensor noise and Environmental conditions	23	30
Unknown concentration of small particles	10	15
Particle shape/density	10	40
3D effects	5	10
Cell mismatch	7	10
Margin	10	10
Total	30%	55%

6. Algorithm Calibration and Validation Requirements

The use of a mean mixture of crystal habits or mean density (global or stratified by cloud type or climate regime) should significantly reduce measurement bias and precision. On-going and future *in situ* measurement campaigns should help improve retrieval assumptions. Such campaigns for precipitating clouds include the TRMM validation missions (e.g. Kwajalein atoll); CALJET/PACJET (sampling storms off the coast of California); Canadian research (George Isaac et al.); and NCAR's WISP program (Roy Rasmussen). For non-precipitating clouds there will be, in the next several years, a number of aircraft- and space-based sub-millimeter sensors that will be able to make measurements of the ice water path. This section summarizes the attributes of some of those sensors that will gather data suitable for the calibration and validation of the CMIS ice water path algorithms.

The FIRSC (Far-InfraRed Sensor for Cirrus) spectrometer has been modified to allow for a more accurate calibration of the measured radiances and to permit autonomous operation. This sensor is scheduled to fly on the Proteus UAV over the ARM Southern Great Plains site. In the future, cirrus cloud measurements can be made year-round as the Proteus aircraft is able to fly above the altitude of the clouds. FIRSC views the upwelling radiation from the Earth, or intervening cirrus clouds, using a far-infrared/sub-millimeter Fourier transform spectrometer with a cryogenic bolometer.

Another sensor being built by JPL is the Submillimeter-Wave Cloud Ice Radiometer (SWCIR). This is scheduled to fly on the NASA DC-8 aircraft in late 2001. The goal for this sensor is a measurement precision of 0.5K in brightness temperature, with an absolute accuracy of 1.0K.

A heterodyne sensor built by NASA Goddard (J. Wang and P. Racette) will have receivers at 183, 380, 487, and 640 GHz, with a total of 11 channels. This is scheduled for completion at the end of 2001.

A multichannel instrument with channels up to 500 GHz is being proposed to the NASA UnESS program. This sensor, the Cloud InfraRed Radiometer for UnESS (CIRRUS), would consist of a four channel HiTc bolometer and would fly on the Space Station starting in 2004. The CIRRUS bolometers would be cooled to about 80 K, which is much warmer than those of the FIRSC sensor. Consequently, more photons must be collected by using wide channels (3 to 1 cm⁻¹) and a large field of view. However, costs will be minimized by flying on the Space Station, and CIRRUS will be able to sample the diurnal cycle of ice clouds.

All the above efforts will serve to advance the technology and algorithms for sub-millimeter remote sensing of ice clouds. The migration of these technologies to CMIS is foreseeable. In addition to the sensors themselves, there are planned validation efforts for these aircraft and space missions which will be based on ground base remote sensing methods (e.g. the ARM cloud radar). The results from these validation campaigns, and the radiometric data itself, will be used to update and validate the CMIS algorithms.

6.1. Pre-launch

6.2. Post-launch

6.3. Special Considerations for Cal/Val

6.3.1. Measurement Hardware

6.3.2. Field Measurements or Sensors

6.3.3. Sources of Truth Data

7. Practical Considerations

7.1. Ice Water Path Algorithm Timing Constraints

Current computer techniques make it feasible to include multiple scattering in a physical-based retrieval algorithm. The limiting step is the need to compute the derivatives with respect to the retrievable parameters using finite differences. This requires several calculations of the forward model radiances for each iteration. Currently several approaches are being investigated to reduce the computation time: (1) Analytical computation of the derivatives, (2) Implementation of the adjoint of the forward model, (3) Parameterization of the cloud microphysics. Further, a hybrid approach could be implemented whereby in the presence of scattering the forward model is replaced by an approximate expression relating the atmospheric and cloud parameters directly to the brightness temperature of the scene. This could be developed in much the same way as the regression-based algorithms are used for the first guess and background in the physical retrieval. These relationships will be used only to calculate the derivatives, which do not require a very high accuracy. The fully-physical forward model will still be used at each iteration to produce the brightness temperatures. It is estimated that this approach will cut the computation time necessary to complete a single iteration by at least a factor of 20.

7.2. Numerical Computation Considerations

7.3. Programming/Procedure Considerations

7.4. Computer Hardware or Software Requirements

7.5. Quality Control and Diagnostics

7.6. Exception and Error Handling

7.7. Special Database Considerations

7.8. Special Operator Training Requirements

7.9. Archival Requirements

8. Appendix 1: Impact of Sub-Millimeter Channels on the IWP Retrieval

8.1. Introduction

The goal of this study is to estimate the added value of the sub-millimeter channels, up to 820 GHz. Based on simulations, we have computed the performances of the Ice Water Path (IWP) retrieval with different instrumental configurations. The configurations considered are: (1) CMIS baseline, (2) CMIS plus a set of three channels centered around the 325 GHz water vapor absorption line, (3) CMIS plus the 325 GHz channels as well as an additional channel at 642 GHz and (4) CMIS plus sub millimeter channels up to 820 GHz. Table 15 shows the central frequencies and the bandwidths of the added sub-millimeter channels.

Table 15: Description of the sub-millimeter channels tested along with the CMIS baseline configuration.

Central Frequency (GHz)	Side 1 (GHz)	Side2 (GHz)	Half-bandwidth (MHz)
325.15000	1.5000	0.0000	500
325.15000	3.1800	0.0000	500
325.15000	5.9400	0.0000	500
642.86000	6.5000	0.0000	500
680.00000	0.0000	0.0000	500
820.00000	0.0000	0.0000	500

Note that the simulations did not include the ozone as an active gas in the sub-millimeter region. While several O₃ lines do exist in this region, the frequencies were chosen so to minimize the impact of O₃ in our simulations.

8.2. Description of the Experiments

The dataset used to compute the performances was constructed around 50 atmospheric profiles over ocean. For each profile we generated randomly a wind speed between 0 and 20 m/s. We also simulated seven discrete values of IWP between 50 and 1000 g/m² and seven discrete values of size distribution median diameter (Dme) between 50 and 800 μm. The total number of profiles processed is thus 2450 per instrumental configuration.

We also simulated a random cloud thickness between 30 and 170 mb. The vertical distribution of the Dme and IWP was assumed inhomogeneous. The degree of inhomogeneity varied randomly. The performances were computed using a known cloud top of 300 millibars.

8.3. Impact of Adding Sub-Millimeter Channels

The interaction between the electromagnetic waves and ice particles depend strongly on the frequency. Higher frequencies (lower wavelengths) are sensitive to smaller size particles. The microwave channels in the CMIS baseline configuration are sensitive to sizes greater than ~400 μm. The sub-millimeter channels are sensitive to sizes smaller than 200 μm. The addition of sub-millimeter channels bridges the gap between the microwave algorithm retrieval (using CMIS baseline) and the infrared algorithm. IR radiances are sensitive to smaller size particles and smaller amounts of ice water path. Depending on the particle shape and on the cirrus cloud thickness, the IR algorithm typically senses Dme's less than ~250 μm and IWP less than 200 g/m² (see Figure 30 through Figure 41). A combined microwave and IR system would allow the retrieval of IWP range that extends to thin cirrus cloud situations.

8.4. Results/Conclusion

Figure 42 to Figure 45 present the different errors binned by ice water path range. Each curve represents a particular value of Dme, in the range 50 to 800 μm . The performances computed used the cumulative range, i.e. for each curve corresponding to a particular Dme value, we have included all the range starting from that value up to the maximum Dme in the dataset (800 μm). The EDR requirements are specified in terms of precision (10% or 5g/m² whichever is greater) and accuracy (5%). The addition of higher frequencies significantly reduces the errors for small Dme (< 400 μm) and extends the range of performance to encompass small Dme's.

The most restrictive Dme threshold is picked (worst case between precision and accuracy). Apparent good performance of baseline near 200 g/m² is due to the choice of the background (200 g/m²) and not to a skill in the retrieval algorithm. The retrieved IWP stays close to the background value because of lack of sensitivity of the radiances in this regime. The performance of the system is summarized in Table 16 and Table 17. Including the sub-millimeter channels can either increase the performance over the same IWP/Dme 2D space or it extend this IWP/Dme space but keeping the same performances. We have chosen to describe the impact of sub-millimeter channels in terms of the latter criterion. In Table 16, the ranges are determined so that we meet the requirements of 15% and 20% in the accuracy and precision errors respectively. These thresholds do not include effects of particle shape and density and neglect effects of small size particles. They also ignore errors due to cell mismatch and 3D effects. Margins to account for these additional sources of error are derived in Section 5. In Table 17, the ranges are determined using a unique metric, 25% of RMS error (square root of the sum of the squares of the previous thresholds on precision and accuracy).

Table 16: IWP and Dme ranges for the different instrumental configurations, based on an accuracy threshold of 15% and a precision threshold of 20%.

	<i>CMIS</i>	<i>CMIS+325</i>	<i>CMIS+325+642</i>	<i>CMIS+325+642+680+820</i>
IWP range (g/m ²)	[300-1000]	[300-1000]	[200-1000]	[200-1000]
Dme range (micro)	380 and up	220 and up	170 and up	170 and up
Freq of occur (%)	-	-	-	-

Table 17: IWP and Dme ranges for the different instrumental configurations, based on an RMS error threshold of 25%.

	<i>CMIS</i>	<i>CMIS+325</i>	<i>CMIS+325+642</i>	<i>CMIS+325+642+680+820</i>
IWP range (g/m ²)	[300-1000]	[250-1000]	[170-1000]	[170-1000]
Dme range (micro)	340 and up	210 and up	160 and up	150 and up
Freq of occur (%)	-	-	-	-

The addition of 325 GHz channels improves the accuracy and precision of the IWP retrieval by extending the range of Dme down to 220 μm (from 380 μm). Adding the 642 GHz further improves to 170 μm . The minimal impact of the 820 GHz in Table 16 is due to the way we determine the range of performance by considering both accuracy and precision. With this additional channel, accuracy is improved to extend the Dme range down to almost 100 μm but not precision.

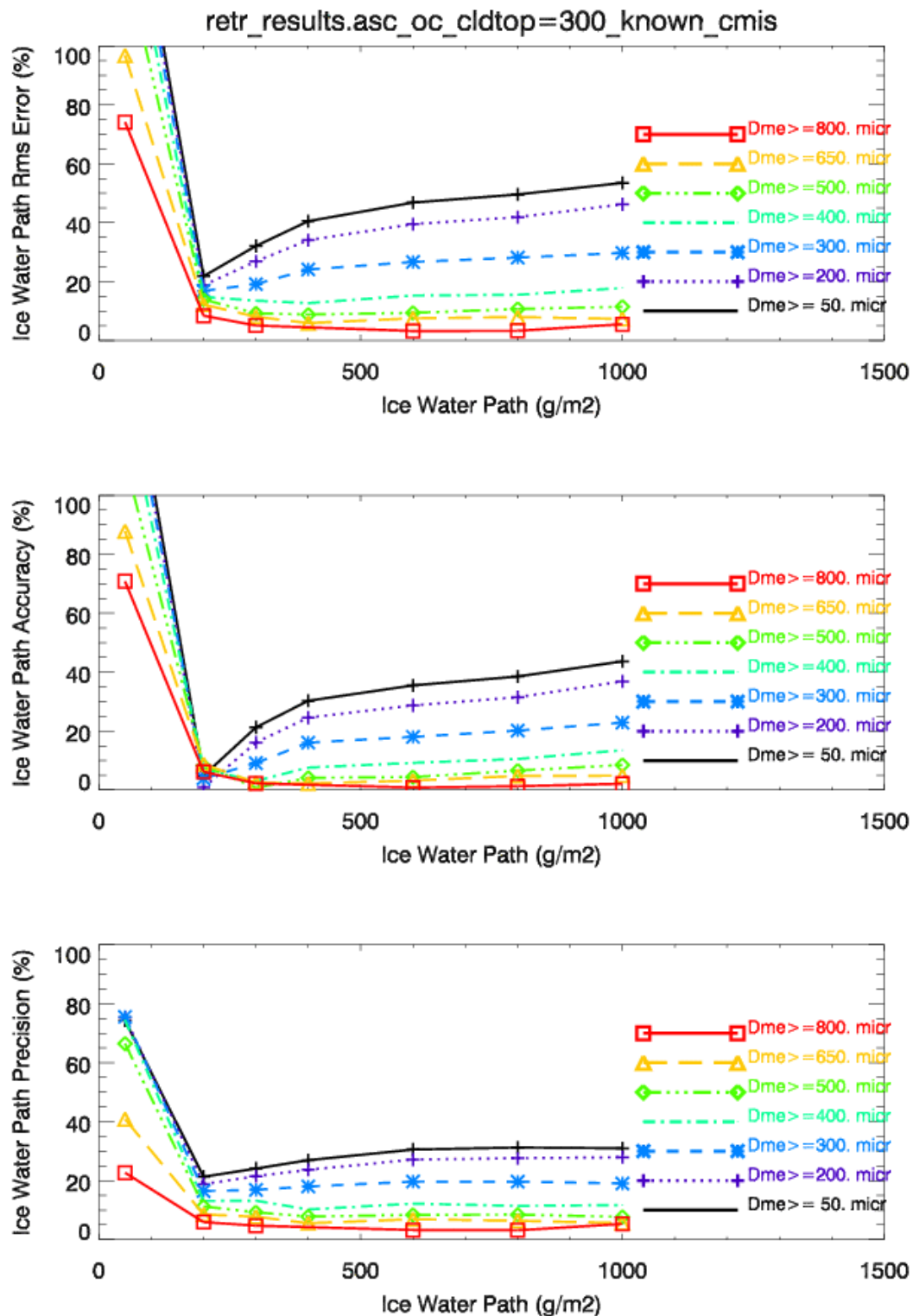


Figure 42: RMS error, accuracy and precision of the ice water path retrieval using the CMIS baseline configuration. The low errors at 200 g/m2 correspond to the background value taken for these retrievals (200 g/m2) and not to a real skill.

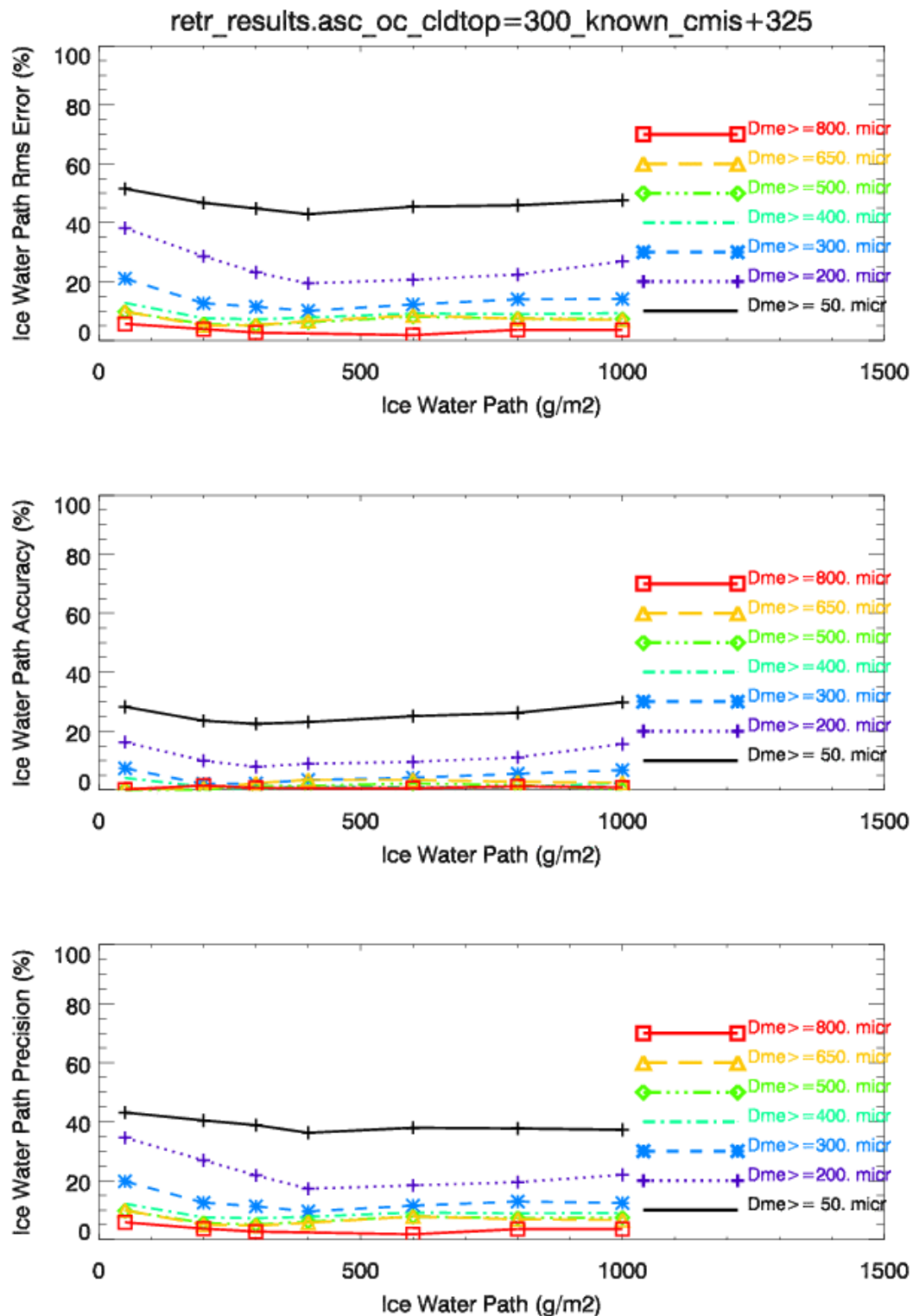


Figure 43: RMS error, accuracy and precision of the ice water path retrieval using the CMIS configuration plus three channels around the 325 GHz WV absorption line.

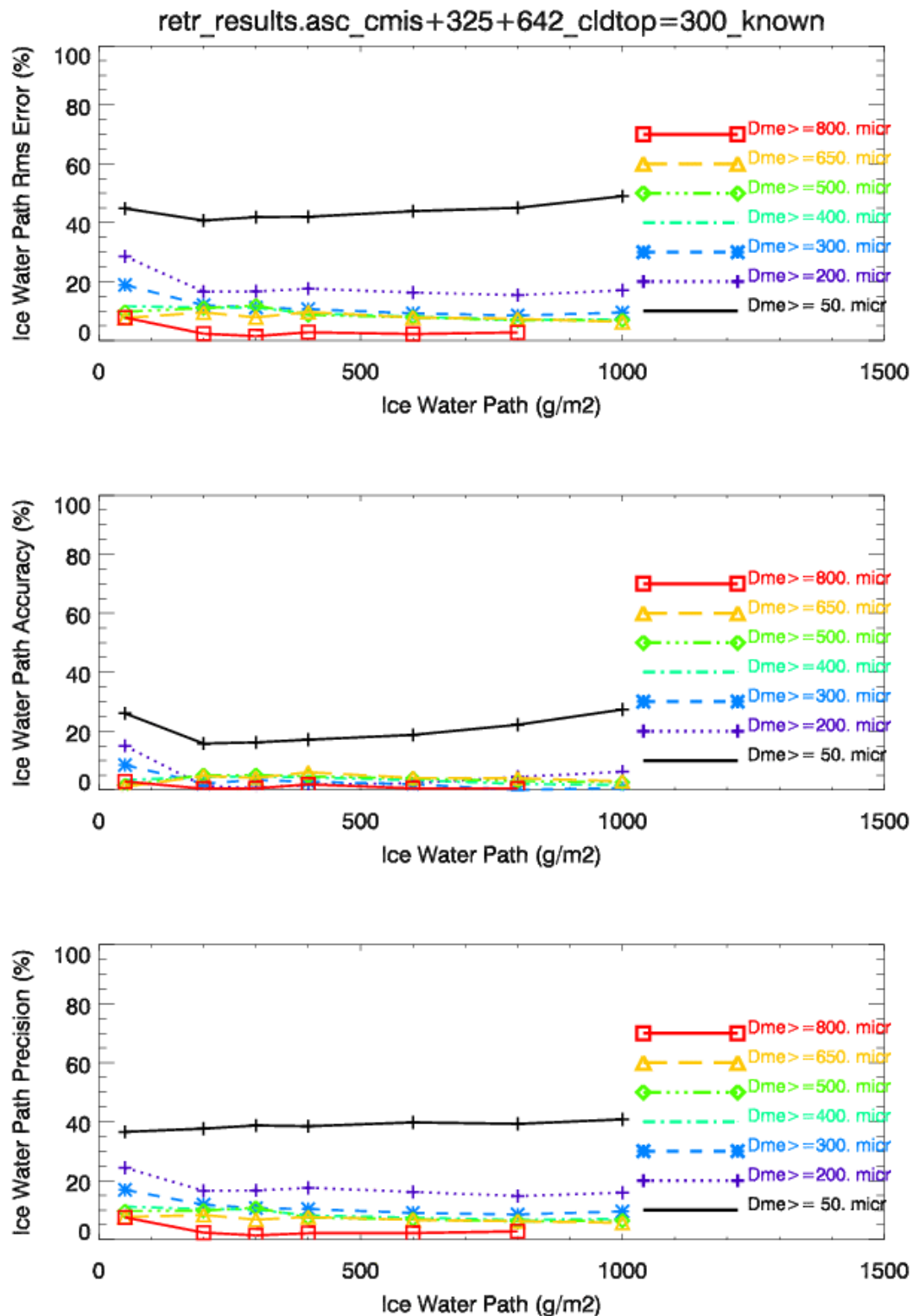


Figure 44: RMS error, accuracy and precision of the ice water path retrieval using the CMIS configuration plus three channels at 325 GHz and an additional one at 642 GHz.

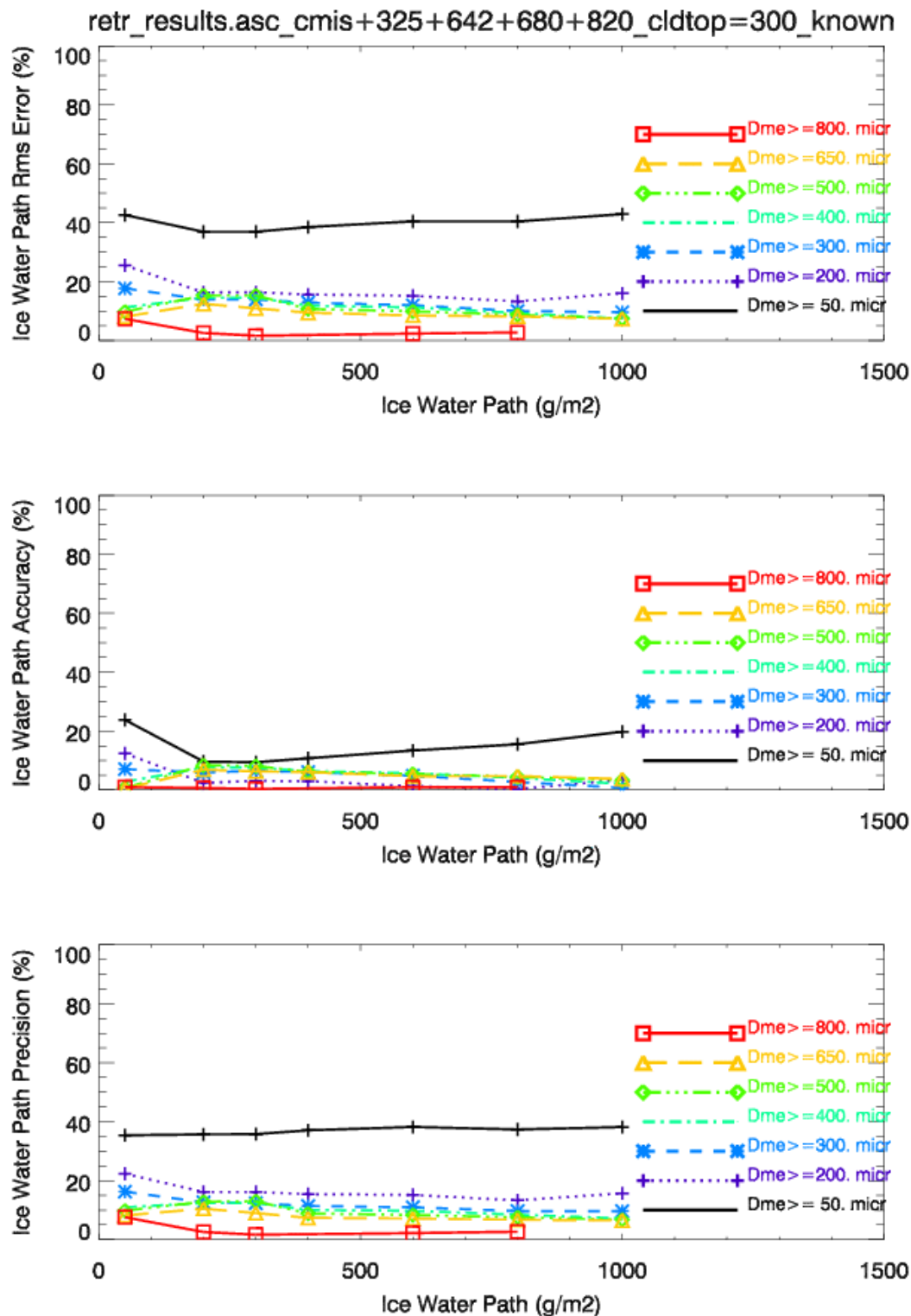


Figure 45: RMS error, accuracy and precision of the ice water path retrieval using the CMIS configuration plus three channels at 325 GHz and additional ones at 642, 680 and 820 GHz.

REFERENCES

- Baran, A. J., J. S. Foot, and D. L. Mitchell, The question of ice crystal absorption: a comparison between T-matrix, Mie and anomalous diffraction theory and implications for remote sensing. *Appl. Optics*, **37**, 2207-2215, 1998.
- Bauer et al., 2000.
- Deeter, M.N. and K.F. Evans.
- Deirmendjian, D., *Electromagnetic scattering on spherical polydispersions*, Elsevier, New York, 1969.
- Evans, K.F. and G.L. Stephens, Microwave Radiative Transfer through Clouds Composed of Realistically Shaped Ice Crystals. Part I: Single Scattering Properties, *J. Atmos. Science*, **52**, pp. 2041-2057, 1995.
- Evans, F., Talk given at the Atmospheric and Oceanic Sciences Department at the University of Wisconsin, Madison on January 31, 2000, <http://nit.colorado.edu/~evans/wisctalk/index.html>
- Evans, K.F., S.J. Walter, A.J. Heymsfield and G.M. McFarquhar, The Submillimeter-Wave Cloud Ice Radiometer (SWCIR): Simulations of Retrieval Algorithm Performance, to be submitted to *J. Appl. Met.*, 2001.
- Evans, K.F., S.J. Walter, A.J. Heymsfield and M.N. Deeter, Modeling of Submillimeter Passive Remote Sensing of Cirrus Clouds, *J. Appl. Met.*, **37**, 184-205 1998.
- Francis, P. N., J. S. Foot, and A. J. Baran, Aircraft measurements of the solar and infrared radiative properties of cirrus and their dependence on ice crystal shape. *Journ. Geophys. Res.*, **104**, 31685-31695, 1999.
- Hale, G. M., and M. R. Querry, Optical constants of water in the 200-nm to 200- μ m wavelength region. *Appl. Optics*, **12**, 555-563, 1973.
- Heymsfield, A. J., and J. Iaquinta, Cirrus crystal terminal velocities. *J. Atmos. Sci.*, **57**, 916-936, 2000.
- Heymsfield, A. J., A. Bansemer, S. Lewis, J. Iaquinta, M. Kajikawa, C. Twohy, and M. Poellot, A general approach for deriving the properties of cirrus and stratiform ice cloud particles. Submitted to *J. Atmos. Sci.*, 2000.
- Heymsfield, A. J., and C. M. R. Platt, A parameterization of the particle size spectrum of ice clouds in terms of the ambient temperature and the ice water content. *Journ. Atmos. Sci.*, **41**, 846-855, 1984.
- Ivanova, D., D. L. Mitchell, W. P. Arnott, and M. Poellot, A GCM parameterization of bimodal size spectra for mid-latitude cirrus clouds. Proceedings, 13th International Conference on Clouds and Precipitation, Reno, Nevada, 546-549, 14-18 August 2000.

REFERENCES

- Korolev, A., G. A. Isaac, and J. Hallett, Ice particle habits in Arctic clouds. *Geophys Res Lett* , **26**, 1299-1302, 1999.
- Korolev, A., G. A. Isaac, and J. Hallett, Ice particle habits in stratiform clouds. *QJ Royal Meteorol Soc*, **126**, 2873-2902, 2000.
- Liu, G. and J.A. Curry, Determination of ice water path and mass median particle size using multichannel microwave measurements, *J. Appl. Met.*, **39**, pp. 1318-1329, 2000.
- Lo, K. K., and R. E. Passarelli Jr., The growth of snow in winter storms: An airborne observational study. *Journ. Atmos. Sci.*, **39**, 697-706, 1982.
- Mace, G. G., T. P. Ackerman, P. Minnis, and D. F. Young, Cirrus layer microphysical properties derived from surface-based millimeter radar and infrared interferometer data. *Journ. Geophys. Res.*, **103**, 23207-23216, 2000.
- Matrosov, S. Y., Retrievals of vertical profiles of ice cloud microphysics from radar and IR measurements using tuned regressions between reflectivity and cloud parameters. *Journ. Geophys. Res.*, **104**, 16741-16753, 1999.
- McFarquhar, G. M., and A. J. Heymsfield, Parameterization of tropical ice-crystal size distributions and implications for radiative transfer: results from CEPEX. *Journ. Atmos. Sci.*, **54**, 2187-2200, 1997.
- McFarquhar, G. M., and A. J. Heymsfield, Microphysical characteristics of three anvils sampled during the central equatorial pacific experiment. *Journ. Atmos. Sci.*, **53**, 2401-2423, 1996.
- Mitchell, D. L., and W. P. Arnott, A model predicting the evolution of ice particle size spectra and radiative properties of cirrus clouds. Part II: Dependence of absorption and extinction on ice crystal morphology. *Journ. Atmos. Sci.*, **51**, 817-832, 1994.
- Mitchell, D. L., Use of mass- and area-dimensional power laws for determining precipitation particle terminal velocities. *Journ. Atmos. Sci.*, **53**, 1710-1723, 1996.
- Mitchell, D.L., Parameterization of the Mie Extinction and Absorption Coefficients for Water Clouds, *J. Atmos. Science*, **57**, pp. 1311-1326, 2000(a).
- Mitchell, D. L., Effective diameter in radiation transfer: General definition, applications and limitations. Submitted to *J Atmos Sci* July 2000(b).
- Mitchell, D. L., A. Macke, and Y. Liu, Modeling cirrus clouds. Part II: Treatment of radiative properties. *J Atmos Sci*, **53**, 2967-2988, 1996.
- Moncet, J.-L., and S.A. Clough, Accelerated monochromatic radiative transfer for scattering atmospheres: Application of a new model to spectral radiance observations, *J. Geophys. Research*, **102**, 21853-21866, 1997.
- Mugnai et al., 1990.

REFERENCES

- Platt, C. M. R., A parameterization of the visible extinction coefficient of ice clouds in terms of the ice water content. *Journ. Atmos. Sci.*, **54**, 2083-2098, 1997.
- Prigent, C., W.B. Rossow and E. Matthews, E., Microwave land emissivities estimated from SSM/I observations, *J. Geophys. Res.*, **102**, pp. 21867-21890, 1997.
- Prigent, C., W.B. Rossow and E. Matthews, Global maps of microwave land surface emissivities: Potential for land surface characterization, *Radio Science*, **33**, pp. 745-751, 1998.
- Racette, P., R.F. Adler, J.R. Wang, A.J. Gasiewski, D.M. Jackson and D.S. Zacharias, An airborne millimeter-wave imaging radiometer for cloud, precipitation, and atmospheric water vapor studies, *J. Atmos. Ocean. Tech.*, **13**, 610-619, 1996.
- Rossow and Shiffer, 1991.
- Ryan, B. F., On the global variation of precipitating layer clouds. *Bull. Amer. Meteor. Soc.*, **77**, 53-70, 1996.
- Twohy, C. H., A. J. Schanot, and W. A. Cooper, Measurement of condensed water content in liquid and ice clouds using an airborne counterflow virtual impactor. *J Atmos Ocean Tech*, **14**, 197-202, 1997.
- Virekanandan et al., 1991
- Weng and Grody, 1994.
- Weng and Grody, Retrieval of Ice Cloud Parameters Using a Microwave Imaging Radiometer, *J. Atmos. Sci.*, **57**, pp. 1069-1081, 2000.
- Wilheit, T.T., The effect of winds on the microwave emission from the ocean's surface at 37 GHz, *J. Geophys. Res.*, **84**, pp 4921-4926, 1979.

LIST OF ACRONYMS

ADD	Algorithm Description Document
AER	Atmospheric and Environment Research
AGL	Above Ground Level
ALFA	AER Local Area Forecast Model
AMS	American Meteorological Society
AMSR	Advanced Microwave Scanning Radiometer
AMSU	Advanced Microwave Sounding Unit
APOLLO	AVHRR Processing Scheme Over Cloud Land and Ocean
APS	Algorithm Performance Simulation
ARA	Atmospheric Radiation Analysis
ARD	Algorithm Requirements Document
ARM	Atmospheric Radiation Measurement
ASRR	Algorithm System Requirements Review
ASTER	Advanced Spaceborne Thermal Emission and Reflection Radiometer
ATBD	Algorithm Theoretical Basis Document
ATOVs	Advanced TOVS
AVHRR	Advanced Very High Resolution Radiometer
BT	Brightness Temperature
CC	Cloud Clearing
CEPEX	Central Equatorial Pacific Experiment
CF	Central frequency
CHARTS	Code for High resolution Accelerated Radiative Transfer with Scattering
CKD	Clough, Kneizys and Davies
CLW	Cloud Liquid Water
CMIS	Conical Microwave Imaging Sounder
COD	Cloud Optical Depth
CTH	Cloud Top Height
CTP	Cloud Top Pressure
DEM	Digital Elevation Model
DMSP	Defense Meteorological Satellite Program
DoD	Department of Defense
DOE	Department of Energy
ECMWF	European Centre for Medium-Range Weather Forecasting
EDR	Environmental Data Record
EIA	Earth Incidence Angle
EOF	Empirical Orthogonal Function
EOS	Earth Observing System
ESFT	Exponential Sum Fitting Technique
FFT	Fast Fourier Transform
FIRE	First ISCCP Regional Experiment
FOR	Field Of Regard
FOV	Field Of View
GPS	Global Positioning System
GSFC	Goddard Space Flight Center
HH	Hole Hunting
HIRS	High-resolution Infrared Sounder
HSR	Horizontal Spatial Resolution
IFOR	Instantaneous Field Of Regard

IFOV	Instantaneous Field Of View
ILS	Instrument Line Shape
IPO	Integrated Program Office
IPT	Integrated Product Team
ISCCP	International Satellite Cloud Climatology Project
IST	Ice Surface Temperature
IWVC	Integrated Water Vapor Content
JHU	Johns Hopkins University
JPL	Jet Propulsion Laboratory
LA	Lower Atmosphere
LAT	Latitude
LBL	Line By Line
LBLRTM	Line By Line Radiative Transfer Model
LMD	Laboratoire de Météorologie Dynamique
LON	Longitude
LOS	Line Of Sight
LST	Land Surface Temperature
L-V	Levenberg-Marquardt
LVM	Levenberg-Marquardt
MHS	Microwave Humidity Sounder
ML	Maximum Likelihood
MODIS	Moderate-Resolution Imaging Spectrometer
MODTRAN	Moderate Resolution Transmittance Code
MSU	Microwave Sounding Unit
MW	Microwave
NASA	National Aeronautics and Space Administration
NCAR	National Center for Atmospheric Research
NCEP	National Center for Environmental Prediction
NDSI	Normalized Difference Snow Index
NDVI	Normalized Difference Vegetation Index
NEDN	Noise Equivalent Difference
NESDIS	National Environmental Satellite, Data, and Information Service
NN	Neural Network
NOAA	National Oceanic and Atmospheric Administration
NPM	Numerical Prediction Model
NPOESS	National Polar-orbiting Operational Environmental satellite System
NRL	Naval Research Laboratory
NWP	Numerical Weather Prediction
OD	Optical Depth
OI	Optimal Interpolation
OLS	Operational Linescan System
OMIS	Operational Multi-Spectral Imaging Suite
OMPS	Ozone Mapping and Profiler Suite
OSS	Optimal Spectral Sampling
PCA	Principal Component Analysis
PDR	Preliminary Design Review
PSD	Power Spectral Density
POES	Polar Orbiting Environmental Satellite
Psfc	Surface Pressure

PSURF	Surface Pressure
QC	Quality Control
RDR	Raw Data Records
RH	Relative Humidity
RMS/ <i>rms</i>	Root Mean Square
RMSE	Root Mean Square Error
RRTM	Rapid Radiative Transfer Model
RT	Radiative Transfer
RTA	Radiative Transfer Algorithm
RTE	Radiative Transfer Equation
RTM	Radiative Transfer Model
S/N	Signal/Noise
SAR	Synthetic Aperture Radar
SCPR	Simultaneous Cloud Parameter Retrieval
SDR	Sensor Data Record
SEIT	System Engineering Integrated Product Team
SFR	System Functional Review
SGI	Silicon Graphics, Inc.
SPS	System Performance Simulation
SRD	Sensor Requirement Document
SRR	System Requirements Review
SSM/I	Special Sensor Microwave/Imager
SSM/T	Special Sensor Microwave/Temperature
SSMIS	Special Sensor Microwave Imager Sounder
SST	Sea Surface Temperature
SVD	Single Value Decomposition
SW	Shortwave
T	Temperature
TBD	To Be Determined (by contractor)
TBR	To Be Resolved (by contractor/government)
TBS	To Be Supplied (by government)
TIGR	TOVS Initial Guess Retrieval
TIM	Technical Interchange Meeting
TOA	Top Of Atmosphere
TOD	Time of Day
TOVS	TIROS-N Operational Vertical Sounder
TRD	Technical Requirements Document
TSKIN	Skin Temperature
UA	Upper Atmosphere
UR	Unified Retrieval
USGS	United States Geological Survey
VIIRS	Visible/Infrared Imager/Radiometer Suite
Vis	Visible
WPTB	Weather Product Test Bed
WV	Water Vapor
WVF	Water Vapor Fraction